First-Principles Calculations of the Local Electronic Structure in Undoped and Doped Cuprates

Dissertation

zur
Erlangung der naturwissenschaftlichen Doktorwürde
(Dr. sc. nat.)

vorgelegt der
Mathematisch-naturwissenschaftlichen Fakultät
der
Universität Zürich

von
Christophe Bersier
von
Cugy FR

Begutachtet von
Prof. Dr. Daniel Wyler
Prof. Dr. Peter Fritz Meier

Zürich 2005

Die vorliegende Arbeit wurde von der Mathematisch-naturwissenschaftlichen Fakultät der Universität Zürich auf Antrag von Prof. Dr. Daniel Wyler und Prof. Dr. Hugo Keller als Dissertation angenommen.

To my mother and the memory of my grandfather Albert Blanc

Conscient de l'inachèvement propre à toute entreprise vouée à la recherche, et une publication sur papier ne pouvant s'exprimer en temps réel, c'est sciemment que je publie cette thèse sans y mentionner tous les travaux qui on paru récemment. Tous les chercheurs le savent bien: le seul élément définitif en sciences, ce ne sont pas les réponses, mais la recherche. Du reste, comme l'a dit Maurice Blanchot: "La réponse c'est la mort de la question. Une réponse est un tiroir qu'on ferme, une question un tiroir qu'on ouvre."

Contents

Abstract

The local charge and spin density distributions in various cuprates are calculated within the spin polarized density functional theory. A cluster model is used which allows a detailed investigation into the electronic structure of a region of the crystal.

In the first part of this work, the electric field gradients at the Cu sites in electron doped Nd_2CuO_4 are determined. The experimental Cu NQR frequency is smaller in the undoped parent compound than in hole doped cuprates. This is explained by a different population of the $3d_{3z^2-r^2}$ atomic orbital. Furthermore the strong decrease of the Cu NQR frequency under doping is explained by a difference of population in the $3d_{3z^2-r^2}$ and $3d_{x^2-y^2}$ orbitals.

In the second part of this work, the effect of zinc and nickel substitution on the local electronic structure of several cuprates is investigated. Clusters comprising 5, 9, and 13 copper atoms in the cuprate plane of La_2CuO_4, $YBa_2Cu_3O_7$, and $YBa_2Cu_4O_8$ are used. The cluster method enables a detailed study of the changes in the charge and spin density distribution induced by Zn and Ni substitution. Furthermore, doping with charge carriers in the above materials is simulated and the resulting changes in the charge distribution are compared to the changes induced by Zn and Ni impurities. These differences are then discussed in terms of a phenomenological model related to properties expected from the generic phase diagram. The effects of zinc and nickel substitution are rather local and, as expected, the absolute values of the Mulliken charges at both nearest and next nearest neighbor oxygens to Zn are larger than in the unsubstituted clusters. The calculated electric field gradient at Cu sites that are nearest neighbor to Zn is found to be somewhat larger than in the unsubstituted cluster, whereas that of next nearest neighbors is about 5 % smaller. We conclude that the additional peak in the Cu NQR spectrum occurring upon Zn substitution in $YBa_2Cu_3O_7$ and $YBa_2Cu_4O_8$ has its origin at the Cu that are next nearest neighbors to Zn.

In the third part of this work, the electronic structure of La_2CuO_4, $Sr_2CuO_2Cl_2$, and $Sr_2CuO_2F_2$ which have respectively O, Cl and F at the apex position, are compared in order to investigate the changes induced by different apex environments. The copper $3d_{x^2-y^2}$ and the planar oxygen $2p_\sigma$ atomic orbitals exhibit a similar degree of covalency in all three compounds. The out-of-plane orbitals however, are quite different with the $3d_{3z^2-r^2}$ atomic orbital lowered significantly in energy for chlorine and fluorine replacing oxygen at apical positions.

Zusammenfassung

In dieser Arbeit wird die lokale Ladungs- und Spindichteverteilung in verschiedenen Kupraten im Rahmen der spinpolarisierten Dichtefunktionaltheorie berechnet. Dazu wird ein Clustermodell verwendet, welches detaillierte Untersuchungen der elektronischen Struktur eines Ausschnittes aus einem Kristall erlaubt.

Im ersten Teil werden die elektrischen Feldgradienten an planaren Kupferplätzen in mit Elektronen dotiertem Nd_2CuO_4 bestimmt. Die beobachtete ^{63}Cu NQR Frequenz im undotierten Material ist viel kleiner als die in den mit Löchern dotierten Kupraten. Dies wird mit einer unterschiedlichen Population der atomaren $3d_{3z^2-r^2}$ Orbitale erklärt. Ausserdem wird die starke Abnahme der ^{63}Cu NQR Frequenz bei Dotierung durch die Differenz der Populationen in den $3d_{3z^2-r^2}$ und $3d_{x^2-y^2}$ Orbitalen erklärt.

Im zweiten Teil wird untersucht, wie die lokale elektronische Struktur in verschiedenen Kupraten verändert wird, wenn einige Kupferatome durch Zink oder Nickel ersetzt werden. Cluster, die 5, 9 und 13 Kupferatome in der Kupferoxyd Ebene enthalten, werden für La_2CuO_4, $YBa_2Cu_2O_7$ und $YBa_2Cu_4O_8$ benützt. Die Cluster Methode erlaubt eine detaillierte Untersuchung der Veränderung der Ladungs- und Spinverteilung, die durch die Einführung von Zn und Ni induziert wird. Ausserdem wird die Dotierung mit Ladungsträgern in den oben erwähnten Materialien simuliert und die resultierenden Veränderungen in der Spin- und Ladungsverteilung werden mit den durch Zn und Ni induzierten Veränderungen verglichen. Diese Unterschiede werden dann im Rahmen eines phänomenologischen Modells diskutiert, das mit den aus dem Phasendiagramm erwarteten Eigenschaften verknüpft ist. Die Effekte der Substitution durch Zink und Nickel sind ziemlich lokal und die absoluten Werte der Mulliken Ladung an den Sauerstoff, die nächste und übernächste Nachbarn zum Zink sind, sind grösser als in den unsubstituierten Clustern. Der berechnete elektrische Feldgradient ist für ein Kupfer grösser als in den unsubstituierten Clustern, wenn es nächster Nachbar zu Zink ist, aber etwa 5 % kleiner, wenn es übernächster Nachbar ist. Dies erklärt das Auftreten einer zusätzlichen Resonanz im NQR Spektrum in Zn substituiertem $YBa_2Cu_3O_7$ und $YBa_2Cu_4O_8$ und ordnet dies den übernächsten Nachbarn zu Zn zu.

Der dritte Teil enthält einen Vergleich der elektronischen Struktur von La_2CuO_4, $Sr_2CuO_2Cl_2$und $Sr_2CuO_2F_2$, die unterschiedlich ein O, Cl, oder F an der Apexposition haben. Damit wird die induzierte Veränderung von verschiedenen Apex-Umgebungen untersucht. Die atomaren Orbitale $3d_{x^2-y^2}$ am Kupfer und $2p_\sigma$ am planaren Sauerstoff zeigen einen ähnlichen Kovalenzgrad. Die Orbitale senkrecht zu den Ebenen sind jedoch recht verschieden: das $3d_{3z^2-r^2}$ Orbital liegt energetisch tiefer für Cl und F an den Apex-Positionen als für O.

1 Introduction

1.1 General overview

Superconductivity is among the most fascinating phenomena in nature. The resistivity of the superconducting materials vanishes entirely upon cooling below the so-called critical temperature T_c. This phenomenon was a complete surprise when it was first observed by H. Kammerling Onnes [92] in 1911. He wanted to test the validity of the Drude theory by measuring the resistivity at the lowest temperatures possible. Investigating mercury he observed that all signs of resistance appeared to vanish suddenly below a temperature of 4 K. This was quite unexpected from the Drude model and was the discovery of a new state of matter: superconductivity.

The strange properties of superconductors are direct consequences of quantum mechanics. While most other quantum effects only appear in matter on the atomic and subatomic scale, superconductivity shows the effects of quantum mechanics acting on the bulk properties of matter on a large scale. In essence, superconductivity is a macroscopic quantum phenomenon.

It took more than 40 years of theoretical effort to find a theoretical background to explain the remarkable phenomenon observed by H. Kammerling Onmes. At this point, it is natural to wonder why it took so long to find a microscopic theory of superconductivity. There are several reasons for this. Firstly, for almost twenty years the physics community did not possess the basic building blocks needed to formulate a solution - the quantum theory of normal metals including Bloch theory and many electron theory. Secondly, it was not until 1934 that a key experiment was performed, the demonstration by Meissner that another basic property of a superconductor was its perfect diamagnetism. Thirdly, once the building blocks were in place, it quickly became clear that the characteristic energy associated with the formation of the superconducting state is tiny, roughly a millionth of the normal state characteristic electronic energies. Theorists therefore focused their attention on developing a phenomenological description of superconducting flow. The way was led by F. London, who pointed out in 1935 that "superconductivity is a quantum phenomenon on a macroscopic scale, ...with the lowest energy state separated by a finite interval from the excited states" and that "diamagnetism is the fundamental property"[1].

In 1957 Bardeen, Cooper, and Schrieffer (BCS) [19] published the first truly microscopic theory of superconductivity. The theory was soon recognized to be correct in all the essential aspects, and to explain a number of very important experimental phenomena. In particular the theory correctly explains the isotope effect i.e. the change of the transition temperature with the mass of the crystal lattice ions. The second main prediction of the

---

[1] For more details from an historical point of view we refer the reader to the very complete book of Matricon and Waysand [79]

BCS theory is the existence of the energy gap at the Fermi level separating the occupied and unoccupied quasiparticle states, a feature which had been foreseen by London.

BCS theory is built upon three major insights: (i) It turns out that from collective behaviour of the electrons the effective forces between them can sometimes be attractive in a solid rather than repulsive. This is due to coupling between the electrons and the phonons of the underlying crystal lattice. (ii) In the famous “Cooper problem”, Cooper [38] considered the simple system of just two electrons outside a filled Fermi sea. Surprisingly, he found that the electrons form a stable pair bound state called “Cooper pair”, and this no matter how weak the attractive force is. This leads to the so-called “Cooper instability” for which every electron at the Fermi surface will become bound into a Cooper pair. Furthermore these pairs are found in an *s-wave state.* (iii) Lastly Schrieffer constructed a many-particle wave function which all the electrons near the Fermi surface being paired up. The BCS wave function represents a coherent state of cooper pairs [8]. The BCS energy corresponds to the energy for breaking a pair into two free electrons, and is a direct result of Schrieffers analysis. We shall call superconductors which are appropriate for analysis by BCS theory *BCS superconductors.*

The BCS theory remains one of the greatest achievements in many-body theory and it had a significant impact on many other fields of physics. One example is the famous Higgs mechanism in the standard model [10]. After the development of the BCS theory it was thought that the phenomenon of superconductivity was restricted to very low temperatures. This pessimism about T_c came both from experimentalists and theorists. It was then an enormous surprise when in 1986 Bednorz and Müller discovered superconductivity at 35 K in the $La_{2-x}Ba_xCuO_4$ system. The discovery of this material was actually motivated by the considerations that higher superconducting transition temperatures could be achieved by combining Jahn-Teller active ions with structural complexity of perovskite oxides. Note that at the time of the discovery, the superconductor with the highest transition temperature known sofar was Nb_3Ge (23 K). This unexpected result gave rise to an intense activity in the field of ceramic oxides and led to the synthesis of compounds with increasingly higher T_c. By 1987 already, a T_c of approximatively 90 K (i.e. higher than the boiling point of liquid nitrogen at 77 K) was observed in $YBa_2Cu_3O_{7-\delta}$. Currently the highest T_c value is 133.5 K (at atmospheric pressure) obtained in the trilayer system $HgBa_2Ca_2Cu_3O_{8+x}$. It has to be emphasized that regardless of the values of T_c the observation of superconductivity in the ceramic copper oxides was itself an unexpected and surprising result[2]. In fact, ceramic materials are typically insulators, and

---

[2] One may wonder whether the discovery by Bednorz and Müller would have been somewhat overlooked if the recently discovered MgB_2 (39 K), had already been discovered earlier.

this is also the case for the undoped copper oxide. When doped, however, the latter become poor metals in the normal state and high-temperature superconductors upon reducing temperature.

Though they come in many different variants the high temperature superconductors (HTSC) (now commonly called *cuprate superconductors*) share some common features. All these compounds are characterized by a layered crystal structure with one or more copper-oxide (CuO_2) planes per unit cell separated by insulating spacer layers. The exception being the compounds of the yttrium family (i.e. $YBa_2Cu_3O_7$ and $YBa_2Cu_4O_8$) which have metallic CuO chain layers as spacer layers. The $La_{2-x}Sr_xCuO_4$ material has two apical oxygens (i.e. oxygens above and below a copper atom in the copper-oxide plane) and its structure is schematically represented in Fig. 1. In the substance of the yttrium family, one of these oxygens is absent, and in other structures, such as Nd_2CuO_4 which can be doped with electrons, the apical oxygens are totally missing. Despite all these complications, the essential structural features to worry about are the CuO_2 planes, which was understood early on, particularly by Anderson [13]. It is now commonly agreed that cuprates have a quasi-two-dimensional (2D)

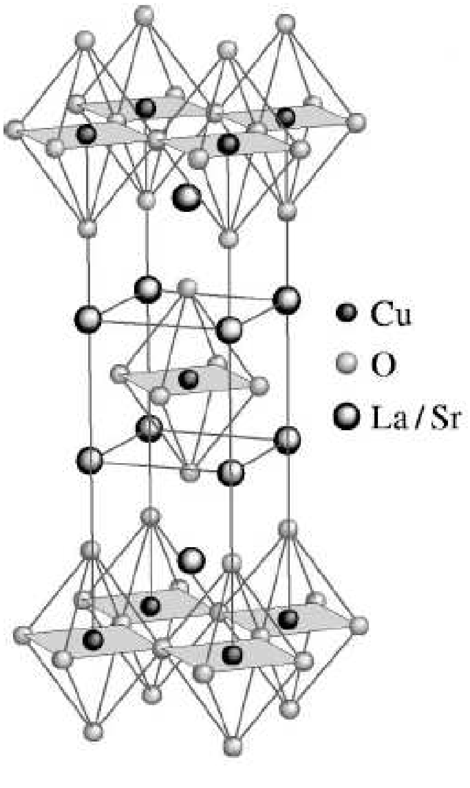

Figure 1: Crystal structure of La_2CuO_4.

electronic structure and that the relevant physics for high temperature superconductivity is localized in the CuO_2 planes. By substituting different elements in the spacer layers or by varying their oxygen content one can dope the charge carriers (electrons or holes) into the CuO_2 planes. Varying the doping level and the temperature reveals a very complex phenomenological phase diagram depicted in Fig. 2 for electron-doped ($Nd_{2-x}Ce_xCuO_4$) and hole-doped cuprates ($La_{2-x}Sr_xCuO_4$).

In cuprates, the *ground state* of the undoped parent compound is an antiferromagnetic (AF) Mott insulator, with an array of localized Cu^{2+} spins in the CuO_2 planes interacting with their nearest neighbors antiferromagnetically. In both hole doped and electron doped systems the Néel temperature (T_N) at which the antiferromagnetic-to-paramagnetic transition occurs decreases with increasing doping level. The antiferromagnetic phase described above is depicted in blue in Fig. 2. Mott insulators are characterized by a strong on-site Coulomb repulsion such that double occupancy of electrons per unit cell is energetically unfavorable and the electronic system behaves like an insulator rather than a good conductor at half filling (which would be predicted by band structure theory). An important signature of doped Mott insulators is the strong electronic correlation among carriers and the sensitivity of their ground state to the doping level. Naively the strong electron-electron correlations are not expected to favor superconductivity for which electrons must be bound together to form Cooper pairs.

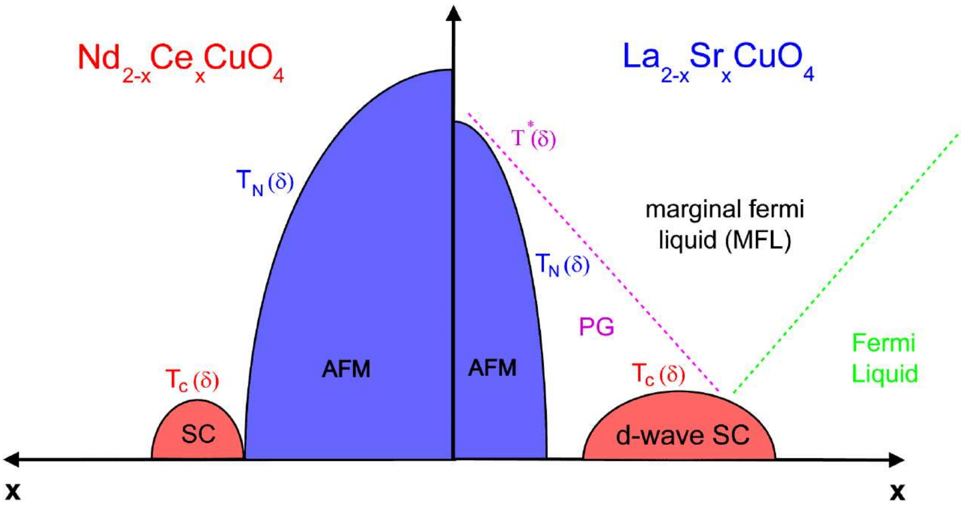

Figure 2: Generic phase diagram for electron doped ($Nd_{2-x}Ce_xCuO_4$) and hole doped ($La_{2-x}Sr_xCuO_4$) cuprates (temperature T versus doping level δ). The insulating antiferromagnetic phase is depicted in blue and the superconducting phase in red.

Upon further doping of carriers, the long range AF correlations vanish and superconductivity appears. The superconducting transition temperature T_c first increases with increasing doping level δ, reaching a maximum T_c at an *optimal doping level.* It then decreases and finally vanishes with further increase of doping. The superconducting phase forms a "dome" depicted in red in Fig.2. Essentially no property of the superconducting state is that of a "conventional" superconductor, in which BCS pairing occurs in a singlet s-wave state ($l = 0$). There is extremely strong experimental experimental evidence that the hole doped cuprates have Cooper pairs with an "unconventional" d-wave pairing state corresponding to an $l = 2$ spin singlet bound state. For pairing states with $l \geq 1$ the Cooper pair wave functions $\phi(\mathbf{r} - \mathbf{r}')$ vanish when $\mathbf{r} = \mathbf{r}'$. This is obviously advantageous in a strongly correlated electron system like cuprates. In electron doped cuprates the pairing symmetry is still a matter of debate. In overdoped samples a metallic regime is observed with an approximate T^2 dependence of the resistivity which was taken as an evidence for Fermi-liquid behavior. The Fermi liquid theory describes the behaviour of the normal state of metals and treats electronic excitations in terms of an interacting gas of renormalized quasiparticles. However the applicability of the Fermi-liquid theory to the "normal" metallic state of HTSC is highly questionable, because many properties do not follow canonical Fermi-liquid behavior and the quasiparticle spins display strong antiferromagnetic correlations (the term marginal Fermi-liquid is often used).

Furthermore for hole doped cuprates between the underdoped and optimally doped region of the phase diagram the normal state properties below a crossover temperature T* are significantly different from those of a Fermi-liquid, and the electronic density of states (DOS) appears to be slightly reduced and this at higher temperatures than for which superconductivity appears. This phenomenon has been called *pseudogap* by the HTSC community and its origin is one of the most debated subject. Most of the theories for cuprate superconductivity are based on the assumption that the pseudogap phenomenon is a precursor for cuprate superconductivity but very recently NMR experiments found this assumption highly questionable [155]. In electron doped cuprates no pseudogap behavior has been observed. Furthermore in electron doped cuprates the AF phase survives over a larger range of doping in contrast to hole doped cuprates, whereas the superconducting phase in electron doped cuprates exists over a much narrower doping range in comparison to the hole doped cuprates.

In hole doped cuprates the holes are believed to enter into the oxygens p-orbitals of the CuO_2 plane. On the other hand electron doping in electron doped cuprates is believed to take place in the d-orbitals of Cu, giving rise to spinless Cu^+-ions that dilute the background AF Cu^{2+}-Cu^{2+} coupling without inducing as strong spin frustrations as in the hole doped cuprates. This provides a simple physical picture why the Néel state survives over a larger

doping range. The fact is that there are many competing orders in cuprates like antiferromagnetism, pseudo gap, stripe phase (charge ordering), spin density wave, charge density wave, etc...
The experimental knowledge that has been accumulated in the field of HTSC is simply staggering. Since the discovery of Bednorz and Müller some 10.000 publications on HTSC per year appeared. Cuprates superconductors can currently claim to be the most well known materials in the history of condensed matter physics. Nevertheless there is still *no* global consensus on the theory of HTSC. First of all the underlying microscopic pairing mechanism remains a mystery. There is unfortunately no coherent global theory which is able to reconcile all the experimental data collected by the different experimental techniques used to probe superconducting cuprates (NMR, ARPES, STM, neutron scattering, μSR, etc...). There are still many questions to be answered but the following questions particularly interest me.

- Why does superconductivity occur despite all the instabilities present in cuprates?
- Why does superconductivity remain stable at so high temperatures?
- What makes the CuO_2 planes so special?
- What is the role of phonons in the cuprates?
- Why is T_c so high in cuprates?

1.2 Introduction to the present work

Among the wide diversity of experimental techniques used to probe the HTSC the nuclear magnetic resonance (NMR) and nuclear quadrupole resonance (NQR) spectroscopic studies have played a major role in investigating the microscopic properties of cuprates. The NMR approach is a *local* probe and is able to get information on the static (Knight shift) as well as the dynamical properties (spin-lattice relaxation rate $1/T_1$, nuclear spin-spin relaxation rate $1/T_{2G}$) of a particular nucleus. By an analysis of these measurements the magnetic hyperfine coupling constants at each nucleus can be extracted. The NQR method probes the interaction of the nuclear quadrupole moment with the electric field gradient (EFG). Both magnetic hyperfine coupling constants and EFGs give direct informations on the ground state charge distribution. In this context the *first principles cluster method* using *localized* basis functions, which is the basic tool used in this work, has been able to provide results for such NMR data such as magnetic hyperfine parameters and EFG which fit well with experimental data [53, 106]. The calculated value of the EFGs can actually be directly tested because it is proportional to the nuclear quadrupole frequency which can be measured experimentally. This successful comparison with experiments gives the cluster method a sound physical basis. The cluster method involves the explicit consideration of all electrons, employs the spin-polarized calculations and is based on density-functional formalism which attempts to account for correlation effects. It is generally accepted that density functional theory handles spin polarization better than unrestricted Hartree-Fock theory. In this thesis we will analyse three different problems.

1.2.1 Electron doped cuprate Nd_2CuO_4

In the electron doped cuprates like Nd_2CuO_4 a quite small ^{63}Cu nuclear quadrupole frequency has been observed in the undoped parent compound in comparison to the hole doped cuprates like La_2CuO_4 or $YBa_2Cu_3O_7$. The origin of this difference has not been clearly identified yet. Furthermore under electron doping the ^{63}Cu nuclear quadrupole frequency almost vanishes. This has been interpreted as a signature for a fully occupied 3d shell. However this argument is only valid in a pure ionic picture and a more detailed analysis is needed at this point. Cluster calculations have already permitted a detailed analysis of the different contributions to the electric field gradient in particular in La_2CuO_4. Another advantage of the cluster method is its ability to simulate doping. The first part of this thesis is dedicated to the investigation of the electron doped cuprate Nd_2CuO_4 by cluster calculations and a precise identification of the origin of the small ^{63}Cu nuclear quadrupole frequency in both undoped and doped materials will be presented.

1.2.2 Zn and Ni impurities in cuprates

In the search for a better understanding of HTSC numerous experimental and theoretical investigations have been made on cuprates where some of the planar Cu atoms have been substituted by magnetic (Ni) or non magnetic (Zn) impurities. In conventional BCS superconductors a small amount of magnetic impurities destroys superconductivity, the magnetic impurity acting as a pair breaker. On the other hand BCS superconductors are practically insensitive to a small concentration of non-magnetic impurities due to the fully gapped Fermi surface and therefore limited interaction with low-energy excitations at low temperatures. However the situation is much different in HTSC which are classed as unconventional superconductors. In this case non-magnetic impurities like Zn destroy superconductivity at a concentration of only a few percent. In hole doped cuprates Zn is even more effective than Ni in destroying superconductivity which typically disappears in La_2CuO_4 for 2.5% Zn substitution or 4% Ni substitution [145]. This strong sensitivity of cuprates to non-magnetic impurities is often claim to be one of the first indirect evidence for unconventional pairing in cuprates.

In spite of the great amount of experiments which have been performed so far in investigating Zn and Ni doped cuprates, the mechanism of the destruction of superconductivity by Zn and Ni impurities is still an unsolved problem. In particular the difference between the two impurities on the superconducting properties is poorly understood. Recently NMR and NQR experiments performed by Williams *et al.* and Itoh *et al.* in Zn substituted $YBa_2Cu_3O_7$ and $YBa_2Cu_4O_8$ revealed the appearance of an additional peak in the ^{63}Cu NQR spectra induced by Zn the origin of which was not yet clearly identified. Furthermore the NMR spin-lattice relaxation rate of the additional peak has been measured to be smaller than the one of the main peak.
In this context the cluster method is especially suited to investigate the electronic properties around an impurity since it is operating in direct space and does not need cyclic boundary conditions. Of course impurities break the translational symmetry and leads to prohibitive complications for calculations based on periodic boundary conditions like band structure methods. The cluster calculations applied to this problem seek to identify the origin of the Zn induced additional peak and provide a test of the recent proposition of Abrikosov which suggest that Zn impurities enhance antiferromagnetic correlation in their vicinity. In addition the cluster calculations will be able to comment on the perturbation to the electronic structure in the immediate vicinity of Zn and Ni.

1.2.3 Comparison of La_2CuO_4, $Sr_2CuO_2Cl_2$ and $Sr_2CuO_2F_2$

As mentioned above the apical anions are believed to be irrelevant for the mechanism of superconductivity. New interest in the apical anions arose when the oxyhalides $Sr_2CuO_2Cl_2$ and $Sr_2CuO_2F_2$ were investigated. The oxyhalides $Sr_2CuO_2Cl_2$ and $Sr_2CuO_2F_2$ have the same structure as La_2CuO_4 except that the apical oxygens are replaced by Cl and F atoms, respectively. One of the questions which have to be answered is what are the differences in the electronic structure with different apex environment. In the last part of this work this question will be addressed and the electronic structure of $Sr_2CuO_2Cl_2$ and $Sr_2CuO_2F_2$ will be calculated with the cluster method and compared to that of La_2CuO_4.

This thesis is organized as follows: In Sec. 2 basic NMR theory will be presented. This will be followed in Sec. 3 by a discussion of the arguments to define a cluster we use to represent a cuprate crystal. A detailed description of each used cluster will be presented. A detailed analysis of the EFG and the charge distribution in Nd_2CuO_4 will be dealt with in Sec. 4. Sec. 5 reviews the effect of magnetic and non-magnetic impurities from both an experimental and a theoretical point of view. The main part of this work (Sec. 6), present a detailed study of the modifications of the charge and spin distributions induced by Zn and Ni impurities in several hole doped cuprates.

The following Sec. 7 is devoted to a comparison of the electronic structure of three different cuprates possessing different apical anions ($Sr_2CuO_2Cl_2$, $Sr_2CuO_2F_2$, and La_2CuO_4). The thesis is concluded by summarizing the main results of this work in Sec. 8.

2 Nuclear magnetic resonance

The calculations that we are going to present in this work can be related to some experimental results performed with nuclear magnetic resonance (NMR). For this reason this chapter contains some of the basic features of this experimental technique. For more details we refer the reader to three more complete publications by Slichter [116], Brinkmann and Mali [36], and Berthier *et al.* [27]. NMR already played a crucial role in the test of the BCS theory and is also widely used in investigating the properties of HTSC. NMR is a local probe of the properties of a material. The theoretical background necessary to describe NMR is one of the most complicated among the experimental techniques used to investigate cuprates. These theoretical complications have made the interpretation of the NMR data of cuprates a very difficult task to achieve and still on-going (see for example [133]). As we will see the informations that can be gained with NMR are very rich. Let us start with the basic Hamiltonian of NMR. Nuclear spins in solids interact with their environment, formed by localized and delocalized electrons. Their total Hamiltonian reads:

$$H_{total} = H_{Zeeman} + H_Q + H_{Hyperfine} + H_{nuclei-nuclei} \tag{1}$$

where the various terms are the Zeeman term, the quadrupolar term, the magnetic hyperfine interaction and the nuclear spin-spin interaction, respectively. Let us discuss separately each contribution to this Hamiltonian.

2.1 The Zeeman Hamiltonian

NMR spectroscopy is actually based on the lifting of the degeneracy of the magnetic quantum number of the nuclear Zeeman levels in an external field, acting on the *nuclear moment* **I**:

$$H_{Zeeman} = -{}^{i}\gamma\hbar H_0 I_z \tag{2}$$

where ${}^{i}\gamma$ is the gyromagnetic ratio of the isotope i. This is the dominant term and the other terms are usually treated as a perturbation except for NQR measurements. The resonance experiment is carried out by inducing magnetic dipole transitions between the energy levels which are allowed by the selection rules ($\Delta m = \pm 1$). In absence of any perturbation the Zeeman Hamiltonian gives rise to a *single line spectrum*, at a Larmor frequency $\omega_n = 2\pi {}^{i}\gamma H_0$. In this section we will take as an example a ^{63}Cu nuclear spin with I=3/2. The effect of the Zeeman Hamiltonian on lifting the degeneracy of the magnetic quantum number can be seen schematically in Fig. 3.

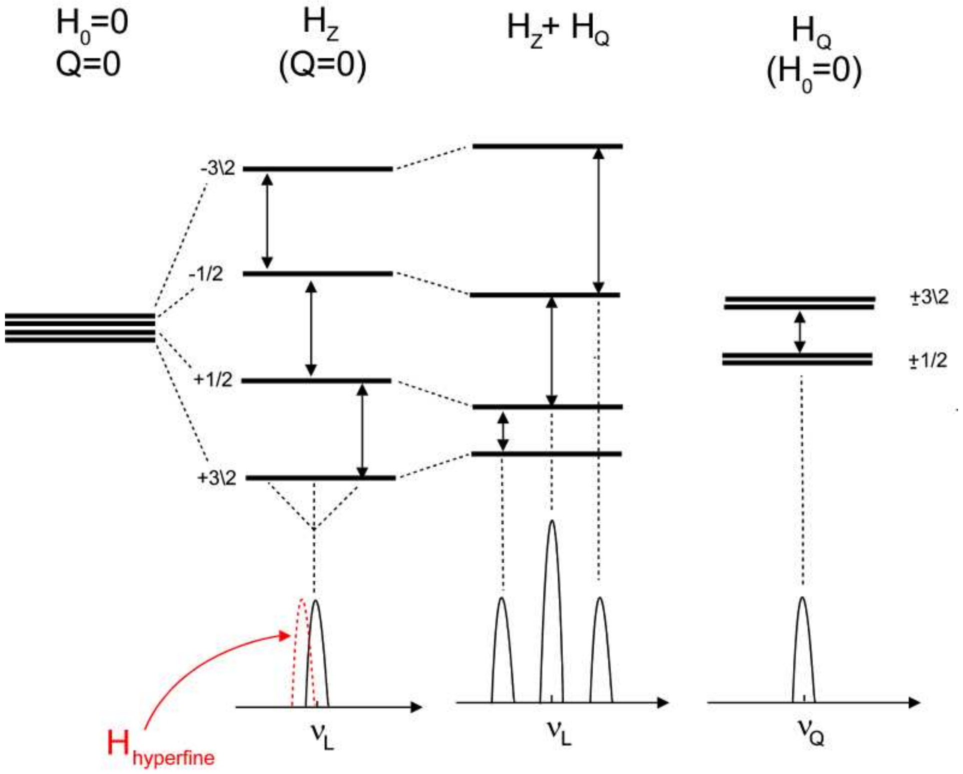

Figure 3: Schematic representation of the splitting due to the Zeeman Hamiltonian (left), the quadrupole Hamiltonian (right), or both together (middle) in NMR and NQR experiments for a nucleus with I=3/2. The possible magnetic dipole transitions are also represented. On the bottom of the figure the observed NMR signal for the different situations is depicted. The effect of the hyperfine interaction is a shift of the NMR line (red).

2.2 The quadrupolar Hamiltonian

Let us now discuss the second term. For nuclear spins greater than 1/2 in a non-cubic symmetry environment, the largest perturbation to the Zeeman Hamiltonian is usually the quadrupole Hamiltonian H_Q. It describes the interaction between the quadrupole moment Q of the nuclei and the electric field gradient (EFG) due to the surrounding electronic charge distribution. The EFG is of central importance in this work because it links our calculations to experiments and therefore gives them their physical value. Let us define the EFG first classically and then quantum mechanically. For this purpose two densities will be defined. The nuclear charge $Z \cdot e$ is distributed over the volume of the nucleus. This distribution is represented by the charge density $\rho_N(\mathbf{r})$ and it creates an electric potential $\phi_N(\mathbf{r})$. On the other hand the electronic charge distribution $\rho_e(\mathbf{r})$ gives rise to an electric potential $\phi_e(\mathbf{r})$. The electrostatic energy for a nucleus with an electrostatic potential $\phi_N(\mathbf{r})$ embedded in an electronic charge distribution $\rho_e(\mathbf{r})$ is:

$$E = \int \phi_N(\mathbf{r})\rho_e(\mathbf{r})d^3r. \tag{3}$$

The localized character of nuclear charge distribution $\rho_N(\mathbf{r})$ allows to perform a multipole expansion of $\phi_N(\mathbf{r})$ [60]

$$\Phi_N(\mathbf{r}) = \frac{q}{r} + \underbrace{\frac{\mathbf{p}\cdot\mathbf{r}}{r^3}}_{=0} + \underbrace{\frac{1}{2}\sum_{i,j=1}^{3}\frac{x_i Q_{ij} x_j}{r^5}}_{\phi_{NQ}(\mathbf{r})}. \tag{4}$$

The first term of this expression contains $q = \int \rho_N(\mathbf{r})d^3r$, which is the total charge of the nucleus. The second term contains $p_i = \int x_i\rho_N(\mathbf{r})d^3r$ the dipole moment of the nucleus which vanishes since the nuclei do not possess a dipole moment due to the definite parity of their wavefunction. The third term contains Q_{ij} the so called quadrupole tensor of the nucleus which is defined as

$$Q_{ij} = \int (3x_i x_j - \delta_{ij}\mathbf{r}^2)\rho_N(\mathbf{r})d^3r. \tag{5}$$

2.2.1 Definition of the electric field gradient

The electric field gradient at the nuclear site ($\mathbf{r} = 0$) is defined as the second derivative of the electronic potential $\phi_e(\mathbf{r})$ with respect to the coordinates x_i $(i = x, y, z)$

$$V_{ij} = \left(\frac{\partial^2\phi_e(\mathbf{r})}{\partial x_i\partial x_j}\right)_{r=0} = \left(\frac{\partial^2}{\partial x_i\partial x_j}\int\frac{\rho_e(\mathbf{r}')}{|\mathbf{r}-\mathbf{r}'|}d^3r'\right)_{r=0}. \tag{6}$$

A straightforward evaluation of the derivatives gives

$$V_{ij} = \int \frac{3x_i x_j - \delta_{ij}\mathbf{r}^2}{\mathbf{r}^5}\rho_e(\mathbf{r})d^3r. \tag{7}$$

With this expression for the EFG, the energy connected with the quadrupole moment ($\int \rho_e(\mathbf{r})\phi_{NQ}(\mathbf{r})d^3r$ where $\phi_{NQ}(\mathbf{r})$ is the third therm in the multipole expansion of Eq. 4) takes the following simple form

$$E = \frac{1}{6}\sum_{i,j} Q_{ij}V_{ij} = \frac{1}{6}\mathrm{Sp}(QV). \tag{8}$$

The electric field gradient is a symmetrical traceless tensor of rank two. It can be therefore diagonalized. By denoting the diagonal elements by V_{xx}, V_{yy} and V_{zz} and sorting them by their absolute values $|V_{zz}| \geq |V_{yy}| \geq |V_{xx}|$ the EFG components in the principle axis frame of reference and $\eta = \left|\frac{V_{xx}-V_{yy}}{V_{zz}}\right|$ the so called *asymmetry parameter* the EFG tensor can be written as:

$$\mathbf{V} = \begin{pmatrix} V_{xx} & 0 & 0 \\ 0 & V_{yy} & 0 \\ 0 & 0 & V_{zz} \end{pmatrix} = V_{zz} \begin{pmatrix} \frac{\eta-1}{2} & 0 & 0 \\ 0 & -\frac{\eta+1}{2} & 0 \\ 0 & 0 & 1 \end{pmatrix}. \tag{9}$$

Now quantum mechanically the EFG tensor is calculated with $\rho_e = |\Psi_0|^2$ as (we have now generalized the above formula for a nucleus at an arbitrary position $\mathbf{r}$),

$$V_{ij}(\mathbf{r}) = \langle\, \Psi_0 |\, \mathcal{V}^{\mathbf{r}}_{ij} \mid \Psi_0 \,\rangle = \int d^3r' \mathcal{V}^{\mathbf{r}}_{ij}(\mathbf{r}')\rho_e(\mathbf{r}'). \tag{10}$$

with

$$\mathcal{V}^{\mathbf{r}}_{ij}(\mathbf{r}') = \frac{3(r'_i - r_i)(r'_j - r_j) - \delta_{ij}|\mathbf{r}' - \mathbf{r}|^2}{|\mathbf{r}' - \mathbf{r}|^5}. \tag{11}$$

The EFG tensor reflects the symmetry of the electronic environment (the crystal field). For example nuclei at different sites in the crystal can have different EFG tensors if they are at different symmetry sites. Typically one has $V_{xx} = V_{yy} = V_{zz} = 0$ for cubic symmetry and $\eta = 0$ for the tetragonal symmetry[3]. It is important to realize that although it is defined at one specific nuclear site the EFG depends on the entire electronic charge distribution. Therefore the EFG at a specific site (the target atom) have contributions not only from the charge distribution of this target atom but also from all the other atoms.

In quantum chemical calculations the molecular orbitals (MO) of the system are linear combinations of the atomic orbitals (AO), i.e. the basis functions. In cuprates the different contributions to EFG can be decomposed into three parts [119]. (i) A first term with all the contributions from an on-site basis functions (regional partition I). (ii) A second term coming from both on-site and off-site basis functions (that is an overlap term). (iii) A third term which contains no on-site basis functions (everything else). This will be of importance in Sec. 4.

---

[3] For a Cu^{2+} in a tetragonal environment the field gradient comes from the empty $3d_{x^2-y^2}$ (the full shells do not contribute to the EFG) and can be easily calculated to be $V_{zz} = \frac{4}{7}\langle r^{-3}\rangle$ and $V_{xx} = V_{yy} = -\frac{2}{7}\langle r^{-3}\rangle$.

2.2.2 Definition of the quadrupolar Hamiltonian

The quadrupolar Hamiltonian appearing in Eq. (1) has the following form

$$H_Q = \frac{eQV_{zz}}{4I(2-1)}\left[3I_z - I^2 + \frac{1}{2}\eta((I_+)^2 + (I_-)^2)\right] \tag{12}$$

In absence of any external magnetic field and spontaneous spin polarization the degeneracy of the magnetic quantum number is partially removed by the EFG. The splitting of the energy level and the signal obtained for a nuclear moment $I = 3/2$ can be seen in the right section of Fig. 3. This situation is called nuclear magnetic quadrupole resonance (NQR). This technique is widely used in the study of cuprates, in particular for Cu and La nuclei. One of the great advantages of NQR is the possibility to measure the spin-lattice relaxation rate in zero field, avoiding complications related to vortices in the mixed phase.

2.2.3 Connection between EFG and NQR frequency

For both ^{63}Cu with $I = 3/2$ and ^{17}O with $I = 5/2$ the quadrupole frequency is defined to be the frequency at which (magnetic dipole) transitions from $m = \pm 3/2$ to $m = \pm 1/2$ are induced. This frequency can be evaluated to give

$$^{i}\nu_Q = \frac{\Delta E(\pm 3/2 \rightarrow \pm 1/2)}{h} = \frac{e\,^{63}QV_{zz}}{2h} \quad \text{for Cu and} \tag{13}$$

$$= \frac{3e\,^{17}QV_{zz}}{20h} \quad \text{for O.} \tag{14}$$

In the above formula the EFG must be inserted in SI units (with V_{zz}/e given in V/m^2). For the field gradient, 1 a.u.[4] corresponds to $9.7174 \cdot 10^{21} \cdot e\text{V/m}^2$.

2.2.4 Zeeman and quadrupolar Hamiltonians together

In the case of $H_0 \neq 0$, the quadrupolar Hamiltonian can be treated as a perturbation to the Zeeman Hamiltonian and one obtains in first order perturbation theory a displacement of the energy levels splitted by the Zeeman term. For $I = 3/2$ this leads to three inequivalent transitions which leads to a NMR signal made of three peaks (one central peak and two satellites) as can be seen in the center of Fig. 3. In this case the quadrupole frequency ν_Q can be extracted from the difference of the central peak frequency and one of the satellites.

---

[4] In quantum chemical calculations, usually atomic units (a.u.) are used (see for example [124]).

2.3 The hyperfine Hamiltonian

Let us now discuss the third term of the total Hamiltonian of Eq. (1): the hyperfine Hamiltonian. The hyperfine Hamiltonian describes the interaction of the nuclear spin $\mathbf{I}$ and N electrons with spins $\mathbf{S}^i$ and can be written as

$$H_{hyperfine} = \sum_{i=1}^{N} \mathbf{I} \cdot \mathbf{A} \cdot \mathbf{S}^i = \sum_{i=1}^{N} \sum_{\alpha\beta} I_\alpha A_{\alpha\beta} S^i_{\alpha\beta} \tag{15}$$

where $\mathbf{A}$ is the so called hyperfine interaction tensor. This tensor can be partly calculated with the cluster method. Note that the results of our quantum chemical calculations give the so called reduced hyperfine tensor a which is proportional to A. A is an energy whereas a is a spin density[5] and they transform to each other as following:

$$A_{\alpha\beta} = {}^i\gamma \gamma_e \hbar^2 a_{\alpha\beta} \tag{16}$$

where ${}^i\gamma$ and γ_e denote the nucleus and electron gyromagnetic ratio, respectively. a is the sum of three different contributions. The first contribution is the so-called *isotropic hyperfine density* a_{iso}[6]. A_{iso} represents the direct interaction of the electronic spin density at the nuclear position with the magnetic moment of the nucleus. a_{iso} is given by the spin density at the nucleus (defined as the difference of the density of spin up electrons and spin down electrons):

$$D(\mathbf{r}) = \frac{8\pi}{3}(\rho_e^{\uparrow}(\mathbf{r}) - \rho_e^{\downarrow}(\mathbf{r})). \tag{17}$$

The second contribution is so called *dipolar hyperfine tensor* a^{ij}_{dip}. This tensor describes the interaction of the nuclear spin with an electron spin residing in an on-site non spherically symmetric orbital (i.e. a non-s orbital) or in an orbital from a neighboring atom. The dipolar hyperfine tensor can be evaluated as:

$$\begin{aligned} a^{ij}_{dip}(\mathbf{r}) &= \langle\, \Psi_0^{\uparrow} |\, \mathcal{V}^{\mathbf{r}}_{ij} \,|\, \Psi_0^{\uparrow} \,\rangle - \langle\, \Psi_0^{\downarrow} |\, \mathcal{V}^{\mathbf{r}}_{ij} \,|\, \Psi_0^{\downarrow} \,\rangle & (18) \\ &= \int d^3r' (\rho_e^{\uparrow}(\mathbf{r}') - \rho_e^{\downarrow}(\mathbf{r}')) \mathcal{V}^{\mathbf{r}}_{ij}(\mathbf{r}') & (19) \end{aligned}$$

---

[5] i.e. it is also present if the nucleus has no magnetic moment e.g. ^{16}O.

[6] This term is often called *Fermi contact* if it originates from electrons in singly occupied s orbitals. If, however, it is due to doubly occupied s-states polarized by the spin of other electrons in the same atom or nearest neighbor atoms it is called *core polarization.* In our case both contributions are present explaining the terminology. The isotropic hyperfine density is simply a scalar.

where $\mathcal{V}_{ij}$ is defined in Eq. (11). Like the EFG a_{dip}^{ij} is a traceless tensor which in the principle axis frame of reference reads

$$\mathbf{a}_{dip} = \left(\begin{array}{ccc} a_{dip}^{\parallel} & 0 & 0 \\ 0 & a_{dip}^{\perp} & 0 \\ 0 & 0 & a_{dip}^{\perp} \end{array} \right) \tag{20}$$

with

$$\sum_j a_{dip}^{jj} = a_{dip}^{\parallel} + 2a_{dip}^{\perp} = 0. \tag{21}$$

Note that these equations only hold for the tetragonal symmetry where $a_{dip}^{xx} = a_{dip}^{yy}$. The third contribution comes from the spin-orbit coupling which is a purely relativistic effect representing the interaction of the spin with its own orbital momentum ($\mathrm{H}_{so} \propto \mathbf{L}_e \cdot \mathbf{S}_e$). In case of oxygen, we neglect the spin-orbit coupling, however in cuprates the spin-orbit coupling has a major contribution to the copper hyperfine tensor. Unfortunately this quantity cannot yet be directly calculated by our quantum chemical calculations and has to be estimated by the simplified formula given in [87] based on the simple picture of a singly occupied $3\mathrm{d}_{x^2-y^2}$ orbital

$$a_{so}^{\parallel} = -\frac{62}{7} k \langle\, r^{-3}\, \rangle \quad \text{and} \quad a_{so}^{\perp} = -\frac{11}{7} k \langle\, r^{-3}\, \rangle, \tag{22}$$

where k is estimated to be $k = -0.044$. The values of $\langle r^{-3} \rangle$ can be extracted from our cluster calculations.

2.3.1 The hyperfine Hamiltonian in cuprates: the Mila-Rice Hamiltonian

Early after the discovery of HTSC, the fact that most of the spin density is borne by the copper sites, led Mila and Rice to propose a phenomenological hyperfine Hamiltonian to explain the NMR data. They realized that in cuprates the effective hyperfine tensor at the nuclear site is the sum of an on-site (i.e a contribution from electron spins at the target atom) and a transferred term (i.e. a contribution from electron spins at nearest neighbors to the target atom). With these considerations Mila and Rice wrote the hyperfine (Eq. (15)) Hamiltonian as

$$^{63}H_{hyperfine} = {}^{63}\gamma\hbar^{63}\mathbf{I} \cdot \left(\mathbf{A}_0 \cdot \mathbf{S}_0 + \sum_{i=1}^{4} \mathbf{B}_i \cdot \mathbf{S}_i \right) \tag{23}$$

for a $^{63}\mathrm{Cu}(2)$ nucleus in the CuO_2 plane. The sum runs over the four spins nearest neighbors to the target spin $\mathbf{S}_0$. $\mathbf{A}_0$ is the on-site hyperfine field tensor and $\mathbf{B}$ is the transferred hyperfine field. The four Cu NN to the target atom are contributing to the transferred hyperfine interaction. $\mathbf{A}_0$ is of course the sum of an isotropic, dipolar and spin orbit contribution (i.e. $\mathbf{A}_0 = A_{iso} + \mathbf{A}_{dip} + A_{so}$). Mila and Rice considered B to be isotropic although there is a detectable influence of the dipolar contribution in our calculations [53]. For a planar oxygen the Hamiltonian is

$$^{17}H_{hyperfine} = {}^{17}\gamma\hbar{}^{17}\mathbf{I} \cdot \left(\sum_{i=1}^{2} \mathbf{C}_i \cdot \mathbf{S}_i \right) \tag{24}$$

where $\mathbf{C}$ denotes the transferred hyperfine field coming from each of the two NN to the target O atom. One of the great advantages of cluster calculations is that they permit to calculate each of these contributions separately.
We will not discuss the Y or La Hamiltonians since our cluster calculations have not yet permitted to calculate the properties of these atoms (as discussed in Sec. 6.1 in the cluster calculations presented in this work these atoms are simulated only by pseudopotentials).

2.4 Knight shift

The hyperfine tensor gives rise to a measurable shift of the NMR line proportional to the applied external field (this shift is schematically represented in Fig. 3). It is denoted as the magnetic hyperfine shift (MHS) tensor. Its components can be decomposed into a spin and an orbital part:

$$K_{\alpha\alpha} = K^{spin}_{\alpha\alpha} + K^{orb}_{\alpha\alpha}. \tag{25}$$

$\mathbf{K}^{orb}$ is temperature independent and it has been recently possible to calculate it with cluster calculations [107]. In cuprates below T_c, $\mathbf{K}^{spin}_{\perp}$ decreases with decreasing temperature like it does in BCS superconductors which is a signature of singlet spin pairing. The spin part of the MHS tensor is related to the static spin susceptibility through the relationship:

$$K_{\alpha\alpha} = A^{tot}_{\alpha\alpha}\chi_{\alpha\alpha} \tag{26}$$

A^{tot}_{jj} being the total hyperfine field ($\mathbf{A}^{tot} = \mathbf{A}_0 + 4\mathbf{B}$) .

2.5 Spin-lattice relaxation rate

The spin-lattice relaxation rate $1/\mathrm{T}_1$ is the rate at which the nuclear magnetization relaxes to its thermal equilibrium value along the external magnetic field. It is due to fluctuations of hyperfine fields in perpendicular directions to the applied field. It can be written as:

$$\frac{1}{{}^{i}T_{1\alpha}T} = \frac{{}^{i}\gamma^2 k_B}{\mu_B^2} \sum_{\mathbf{q},\alpha' \neq \alpha} \left| {}^{i}A_{\alpha'\alpha'}(\mathbf{q}) \right|^2 \frac{\chi''_{\alpha'\alpha'}(\mathbf{q},\omega_n)}{g^2_{\alpha'\alpha'}\omega_n} \tag{27}$$

where ${}^{i}A_{\alpha'\alpha'}(q)$ is the Fourier transform of the total hyperfine field defined above in Eq. (23) and $\chi''_{\alpha'\alpha'}(q,\omega)$ is the imaginary part of the spin susceptibility for the wavevector $\mathbf{q}$ and the nuclear Larmor frequency ω_n (α stands for the direction of H_0). That is the imaginary part of the dynamical susceptibility can be probed by NMR. Let us define ${}^{i}F(\mathbf{q}) = \left|{}^{i}A(\mathbf{q})\right|^2$ the so called form factor. For Cu atoms this form factor reads:

$$^{63}F_{\alpha\alpha} = \left[A_{0\alpha\alpha} + 2B(cosq_x a + cosq_y b)\right]^2 . \tag{28}$$

For the applied external field in the c direction (i.e. perpendicular to the CuO_2 plane) and in the case of fully antiferromagnetically correlated copper spins the imaginary part of the spin susceptibility is peaked at $\mathbf{q} = \mathbf{Q}_{AF} = (\pi/a, \pi/a)$. In this case the hyperfine fields are added coherently and one has:

$$^{63}T_{1c}^{-1} \propto (A_{0\perp} - 4B)^2. \tag{29}$$

In the case of fully uncorrelated copper spin the hyperfine fields are added incoherently and one obtains:

$$^{63}T_{1c}^{-1} \propto (A_{0\perp}^2 + 4B^2). \tag{30}$$

2.6 Nuclear spin-spin relaxation

We will not discuss the last term of the NMR Hamiltonian of Eq. (1) which gives rise the so called spin-spin relaxation rate T_{2G} as our calculations can not be related to measurements of this spin-spin relaxation rate. We just mention that T_{2G} is able to provide information about the static part of the staggered spin susceptibility $\chi'(\mathbf{q} \approx \mathbf{Q}_{AF}, \omega = 0)$.

3 Cluster model

In this section we present a brief introduction in the computational method used in this work will be presented. The method is well documented elsewhere (see for example S. Renold [108]) but some new concepts have to be introduced here due to the recent development of the computational tools.
A solution of the many body Schrödinger equation for a macroscopic number of particles is completely out of task. Nevertheless with some approximations and special computational methods it is possible to solve it for a relatively large number of particles. The idea of the cluster method is to solve the many body Schrödinger equation for a portion of the crystal (the cluster). Due to this local character the cluster method is only able to calculate local physical properties of the crystal. A property is called *local* if it can be determined by the electronic structure of a few neighboring atoms in the crystal. Electric field gradients (EFG) and hyperfine fields (see Sec. 2) are such local properties and can be determined by cluster calculations. They are directly comparable with local probes like NMR. Knowing that we are limited by the computational power we have to choose appropriately the atoms composing the cluster. In this work we will concentrate exclusively on the atoms that make up the Cu-O planes and their direct surroundings, as the relevant physics responsible for superconductivity in those material is now commonly agreed to come from the Cu-O planes[7]. As usually in condensed matter physics the irrelevant degrees of freedom are projected out. This is the case for the charge reservoir between the Cu-O planes which we will only simulate with pseudopotentials.
The time *independent* Schrödinger equation is solved within the framework of density functional theory[8]. Unfortunately this method only permits to calculate the *ground state* of the system which is obtained by solving the Kohn-Sham equations [70] self consistently. The excited states are not available[9]. This is a purely static simulation and the result of the calculation can be thought of as a “snapshot” of the electronic structure of the system at a given moment. This gives us the electronic structure “skeleton” of the system.

The calculation is performed in the direct space. This shows many advantages. First, the results in the direct space are more intuitive and easier to interpret than in the reciprocal space. Second, the absence of periodic

---

[7] This is one of the Anderson’s central dogmas [14].

[8] This provides a good trade-off between accuracy and computational cost. Hartree-Fock theory completely neglects correlation effects and yields poor results (see [53]). In contrast, configuration-interaction, which includes both exchange and correlation effects in its Hamiltonian, requires enormous computer resources and is currently prohibitive.

[9] Actually the ground state density contains information on the excited states but no practical way to extract this information is known so far.

boundary conditions permits to determine the electronic structure around defects and impurities. This is in contrast to the usual ab initio methods using periodic boundary conditions which run into severe numerical difficulties due to the large unit cells required for studying the electronic structure around defects or impurities.
However, the cluster method being an open boundary method presents some disadvantages. First, the surrounding conditions of the cluster especially at the border are difficult to simulate. The boundary conditions can be improved by using pseudo-potentials at the border of the cluster. Second, the relatively small size of the clusters implies a high surface to bulk ratio which can lead to finite size effects especially for small clusters (typically smaller than a Cu_5 cluster[10]). This has been dramatically improved recently by refinements of the computational tools which made it possible to almost triple the size of the clusters.
With the Heisenberg uncertainty principle in mind one can view the cluster method as *complementary* to methods which use periodic boundary conditions like band structure calculations. Each method has its advantages and disadvantages. For example band structure calculations failed to reproduce some local properties like for example the EFG at Cu sites in the cuprates (see [53]). On the other hand the cluster method is of course not capable to calculate any collective effects because it does not consider the band structure. Let us now define more precisely the cluster method.

3.1 Definition of the cluster model

A cluster consists of three regions. The target atom and at least its nearest neighboring atoms form the center of the cluster and the corresponding electrons are treated most accurately using first-principles all-electron methods. The atoms in this region are simulated with basis functions. The surrounding conditions acting on the core region are simulated in the following way. The core region is embedded in a large cloud of a few thousand point charges at the respective lattice sites providing a very good approximation of the Madelung potential experienced by the atoms in the crystal. The values chosen for the background point charges are based on the formal valence of the constituents of the crystal (for example La^{3+}). Point charges at the border of the core region are replaced by basis-free pseudopotentials to improve the boundary conditions for the electrons in the cluster core. The pseudopotentials are necessary to provide smooth boundary conditions between the core and the Madelung regions. The absence of pseudopotentials at the border of the cluster would lead to a too strong potential in this region. As a result the electrons would be pulled out from the center of the cluster, pro-

---

[10] This will be defined below.

voking an irregular charge density distribution which is unphysical. These pseudopotentials make up the so-called screening region.

Of course it would be desirable to have clusters that contain as many atoms as possible in the core region but there are two computational limitations to the cluster size: the available computer resources and the convergence of the self-consistent field procedure. However, these limits have been pushed further since our first use of the cluster technique (see Ref. [123]) which now allows to use larger clusters and hence to observe effects which could not be seen before especially by studying the effects of impurities (Sec. 6).

For the atoms in the core region we employed the standard 6-311G basis sets. The electronic structures of all the clusters which we will describe below were determined with the Gaussian 03 quantum chemistry package [43] in the framework of density functional theory incorporating the exchange functional proposed by Becke [20, 21] together with the correlation functional of Lee, Yang, and Parr [75] (specified by the BLYP keyword in the Gaussian 03 program). For more details on the density functional theory we refer the reader to the book of Dreizler and Gross [41] or the very pedagogical book of Koch and Holthausen [69]. The results of each calculation were examined with the Mulliken population analysis which gives a description of the charge and spin densities in terms of the individual atoms and also the constituent orbitals. Other properties such as EFGs and hyperfine fields were also recorded at each copper center.

3.2 Description of the clusters used in this work

In the present work clusters simulating six different cuprates are used for our investigations (Nd_2CuO_4, La_2CuO_4, $YBa_2Cu_3O_7$,$YBa_2Cu_4O_8$, $Sr_2CuO_2Cl_2$ and $Sr_2CuO_2F_2$). The core region of all clusters is made of atoms building the Cu-O planes and their corresponding apex atoms (O, Cl, or F) if present. We use three clusters of different sizes (with 5, 9, and 13 copper atoms in the core region). We will use the terminology Cu_5, Cu_9, and Cu_{13} when referring to these different sizes. All three clusters are centered on the Cu sites. The geometry of the CuO_2 plane (which is identical in all considered cuprates) for the three cluster sizes is displayed in Fig. 5. For clarity these clusters are labeled X/Y where X is the chemical formula of the core cluster and Y the formula of the ions represented by pseudopotential functions.

3.2.1 Spin multiplicities of the clusters

Within the spin-polarized formalism used in this work, the spin multiplicity of a cluster is a *free* parameter of the calculation. In a simple ionic picture, the planar copper atoms and the planar oxygen atoms have a valence of $+2$ and -2, respectively. This leads to a $3d^9$ configuration with a total spin of one half for the copper atom, whereas the oxygen valence gives zero

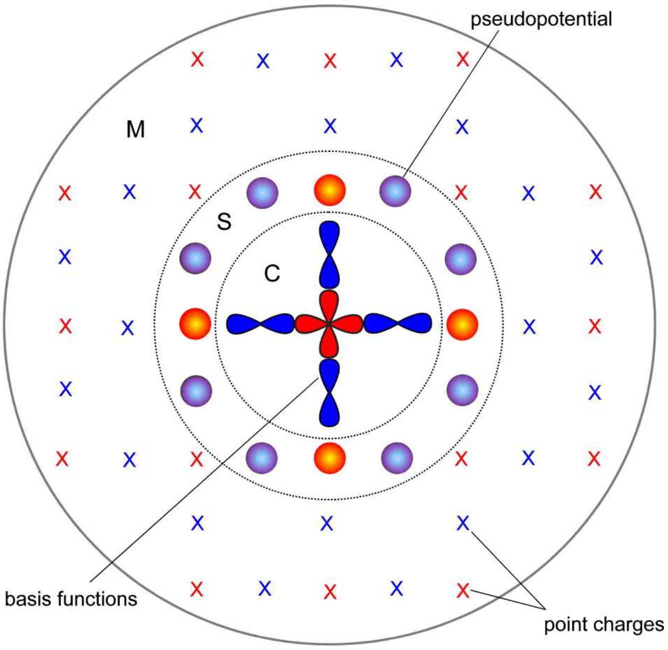

Figure 4: Schematic representation of the cluster model in the CuO_2 plane. The three regions of the cluster are represented: the core region (C), the screening region (S) and the Madelung region (M). The basis functions, the pseudopotentials and the point charges are schematically depicted in this cartoon view.

total spin. This suggests two choices of spin multiplicities with a *physical* significance, a "ferromagnetic" spin multiplicity with all spins parallel and an "antiferromagnetic" spin multiplicity with two neighboring spins being antiparallel. However, other spin multiplicities are also possible leading to a spin alignment which can be viewed as a superposition of an antiferromagnetic and a ferromagnetic spin state. In Table 3.2.1 the chosen spin multiplicities are tabulated for each cluster size. The antiferromagnetic and ferromagnetic spin multiplicities are in bold face. Let us now describe each cluster used in this work separately.

3.2.2 Clusters used for Nd_2CuO_4

Let us first discuss the clusters used in Sec. 4 for the determination of the electronic structure in the electron doped compound Nd_2CuO_4. The crystal structure of Nd_2CuO_4 is the so called T' structure (see Sec. 4). In this case the core region consists only of planar Cu and O. The lattice parameters ($a = b = 3.95$ Å and $c = 12.07$ Å) and the positions of the atoms within the unit cell have been adopted from Ref. [134, 146]. We follow the convention in the literature and label the planar Cu-O bond axes with a and b and

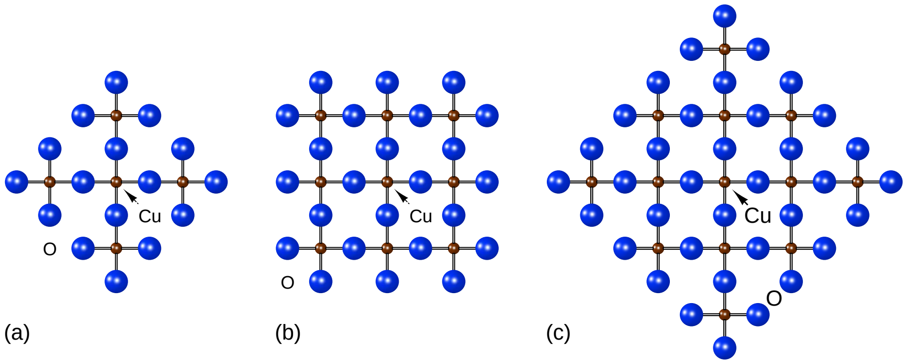

Figure 5: The layout of the CuO_2 planes in all three differently sized clusters, (a) with 5 planar copper atoms, (b) with 9 planar copper atoms, and (c) with 13 planar copper atoms. The apical oxygens are not shown.

cluster	multiplicities
Cu_5O_{26} / Cu_5O_{21}	2, **4**, **6**
Cu_9O_{42} / Cu_9O_{33}	**2**, 4, 6, 8, **10**
$Cu_{13}O_{62}$ / $Cu_{13}O_{49}$	2,4, **6**, 8, 10, 12, **14**

Table 1: Chosen spin multiplicities for the different clusters. The maximal spin multiplicity always corresponds to the “ferromagnetic” spin multiplicity and is printed in bold face. The “antiferromagnetic” spin multiplicity is also printed in bold face. Note that the possible spin multiplicities are determined solely by the number of planar copper atoms and are therefore independent on the specific material.

the axis perpendicular to the CuO_2 plane with c. The core region of the smallest cluster (Cu_5) for Nd_2CuO_4 which is also the simplest cluster used in this work incorporates five planar Cu atoms and their 16 nearest planar oxygen atoms. The screening shell includes bare pseudopotentials for eight Cu^{2+} and 24 Nd^{3+} ions. The Madelung shell contains more than 6000 point charges. According to the attributed valences of copper and oxygens of 2^+ and 2^-, respectively (see Sec. 3.3), this cluster is given at total charge of 22^- leading to a total number of 295 electrons. We will also use Cu_9 and Cu_{13} clusters which properties are given in Table 2. The smallest (Cu_5) and the largest (Cu_{13}) clusters used for the Nd_2CuO_4 substance are schematically depicted in Fig. 6.

3.2.3 Clusters used for La_2CuO_4, $YBa_2Cu_3O_7$, and $YBa_2Cu_4O_8$

Let us start with La_2CuO_4 which will be our reference substance for the hole doped cuprates throughout this work. It will be compared to Nd_2CuO_4 in

Cluster	N	E	B	C [e]
Cu_5O_{16}/Cu_8Nd_{24}	21	295	403	-22
$Cu_9O_{24}/Cu_{12}Nd_{32}$	33	483	663	-30
$Cu_{13}O_{36}/Cu_{12}Nd_{48}$	49	711	975	-46

Table 2: Compilation of the clusters used for Nd_2CuO_4 and some of their defining properties: number of atoms simulated by a full basis set (N), number of electrons (E), number of basis functions (B) and the total charge of the core region (C).

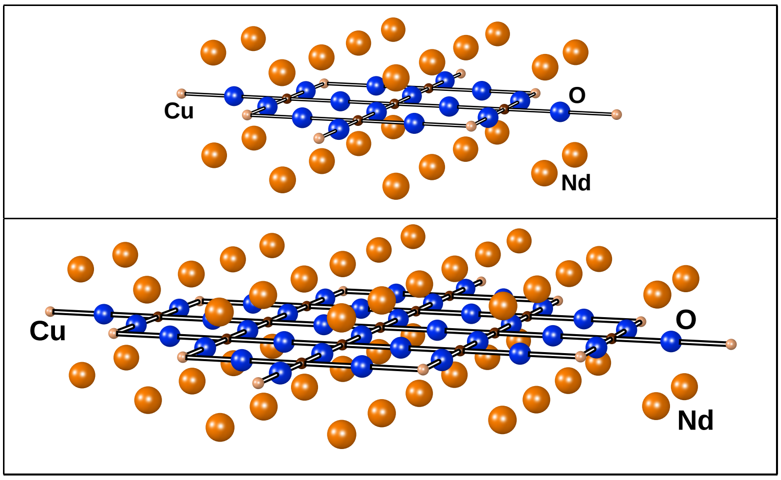

Figure 6: Schematic representation of the Cu_5O_{16}/Cu_8Nd_{24} cluster (top) and the $Cu_{13}O_{36}/Nd_{48}Cu_{12}$ (bottom) cluster.

Sec. 4 and to $Sr_2CuO_2Cl_2$ in Sec. 7. This substance has already been studied in detail by Hüsser *et al.* [53]. The symmetry of La_2CuO_4 is orthorhombic for low doping and temperature but changes to tetragonal with increasing doping and temperature. All calculations are performed assuming the high temperature tetragonal phase mainly for three technical reasons. First, the degree of symmetry of a given system determines the amount of integrals that are identical which in our case speeds up the SCF procedure. Second, we empirically found out that the convergence of the SCF procedure is more likely for clusters with higher degree of symmetry. Third, the CuO_2 plane being perfectly flat (no buckling) permits us to represent charge density distribution differences as in Sec. 6. This choice of structure for La_2CuO_4 was justified by test calculations in the orthorhombic phase [52] which revealed no significant dependence of the EFGs between the orthorhombic and the tetragonal structure. The lattice parameters and the positions of the atoms within the unit cell have been adopted from Ref. [105] ($a = 3.77$ Å and $c = 13.18$ Å). The Cu_5, Cu_9, and Cu_{13} for La_2CuO_4 are shown in Fig. 7.

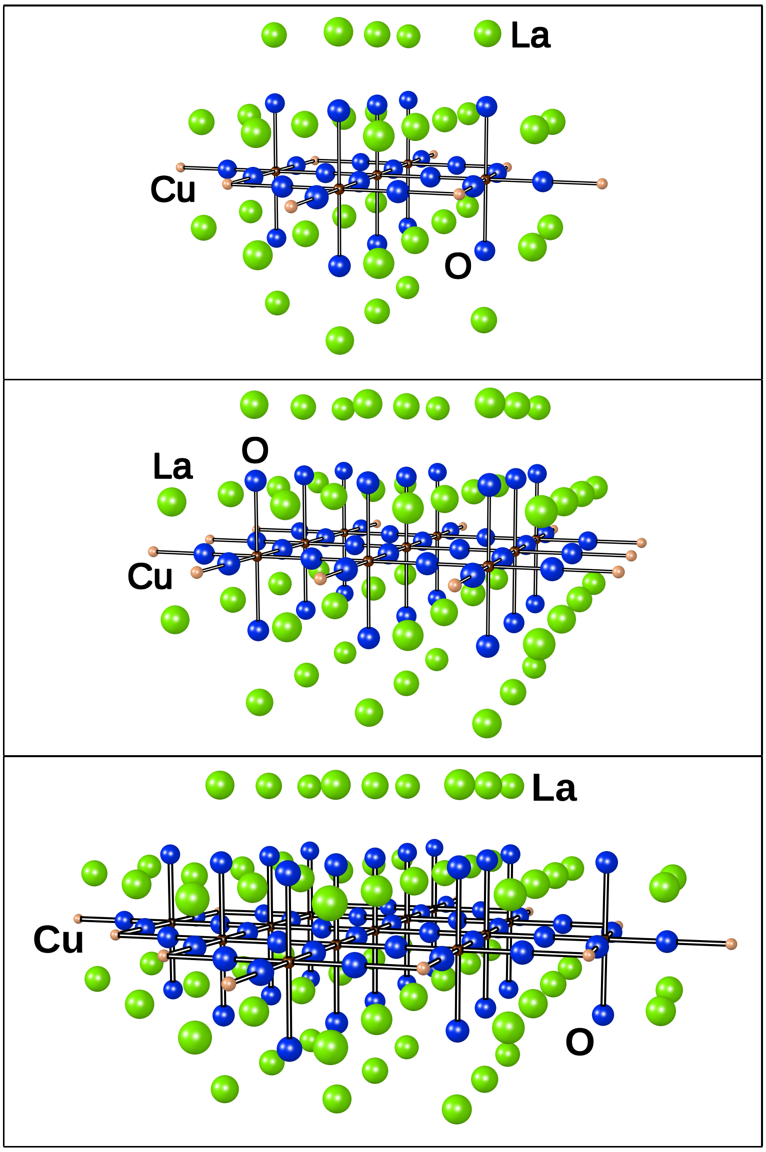

Figure 7: The Cu_5O_{26}/Cu_8La_{34} cluster (top), the $Cu_9O_{42}/Cu_{12}La_{50}$ cluster (middle), and the $Cu_{13}O_{62}/Cu_{12}La_{74}$ cluster (bottom). The atoms connected with bonds are represented by an all-electron basis set. The other atoms drawn show some of those atoms that were represented by bare pseudopotentials.

In Sec. 6 we will also use clusters representing $YBa_2Cu_3O_7$ and $YBa_2Cu_4O_8$. The $YBa_2Cu_3O_7$ and $YBa_2Cu_4O_8$ compounds have a more complex crystal structure than the La_2CuO_4 compound. The most significant difference is the occurrence of a double CuO_2 layer separated by one layer of yttrium ions. As a consequence, the planar copper atom in $YBa_2Cu_3O_7$ and $YBa_2Cu_4O_8$, Cu(2), have only *one* apical oxygen. Furthermore, the CuO_2 layers are slightly buckled in contrast to the flat planes of La_2CuO_4. Another difference between the "Yttrium family" and La_2CuO_4 is the presence of Cu-O chains between the CuO_2 planes. The difference between $YBa_2Cu_3O_7$ and $YBa_2Cu_4O_8$ is that the former has one Cu-O chain whereas the latter has two[11]. It is now commonly agreed that these chains have no direct influence on superconductivity and therefore we will again concentrate on the CuO_2 planes. We constructed the $YBa_2Cu_3O_7$ and $YBa_2Cu_4O_8$ clusters assuming the low-temperature orthorhombic structure with lattice constants $a = 3.827$ Å, $b = 3.882$ Å, and $c = 11.682$ Å for $YBa_2Cu_3O_7$ as given in Ref. [34] and $a = 3.8411$ Å, $b = 3.8718$ Å, and $c = 27.240$ Å for $YBa_2Cu_4O_8$ as given in Ref. [42]. The constitutive properties of the clusters used for La_2CuO_4 $YBa_2Cu_3O_7$ and $YBa_2Cu_4O_8$ are given in Table 3. More informations on the cluster methods applied to $YBa_2Cu_3O_7$ can be found in [108].

Compound	Cluster	N	E	B	C [e]
La_2CuO_4	Cu_5O_{26}/Cu_8La_{34}	31	395	533	-42
La_2CuO_4	$Cu_9O_{42}/Cu_{12}La_{50}$	51	663	897	-66
La_2CuO_4	$Cu_{13}O_{62}/Cu_{12}La_{74}$	75	971	1313	-98
$YBa_2Cu_3O_7$	$Cu_9O_{33}/Cu_{30}Y_{16}Ba_{16}$	42	573	780	-48
$YBa_2Cu_3O_7$	$Cu_{13}O_{49}/Cu_{38}Y_{24}Ba_{24}$	62	841	1144	-72
$YBa_2Cu_4O_8$	$Cu_9O_{33}/Cu_{21}Y_{16}Ba_{16}$	42	573	780	-48
$YBa_2Cu_4O_8$	$Cu_{13}O_{49}/Cu_{25}Y_{24}Ba_{24}$	62	841	1144	-72

Table 3: Compilation of the used clusters for La_2CuO_4, $YBa_2Cu_3O_7$, and $YBa_2Cu_4O_8$ with some of their defining properties: number of atoms (N), number of electrons (E), number of basis functions (B) and the total charge of the core region (C).

3.2.4 Clusters used for $Sr_2CuO_2Cl_2$

In Sec. 7 we will compare the $Sr_2CuO_2Cl_2$ and $Sr_2CuO_2F_2$ compounds with La_2CuO_4. In Sec. 7 two differently sized clusters will be used: a small[12] octahedral-like cluster, CuO_4A_2/Cu_4M_{10} where A = O, Cl, or F and M = La or Sr, respectively (see for example Fig. 1a where A=Cl and M=Sr) and the cluster $Cu_5O_{16}A_{10}/Cu_8M_{34}$ made up of effectively five Cu octahedra (Fig. 8). The sizes of these cluster are sufficient to account for the orbital populations.

---

[11] $YBa_2Cu_4O_8$ is also a stoichiometric compound whereas $YBa_2Cu_3O_7$ is not. This gives rise to much narrower NMR lines in $YBa_2Cu_4O_8$ than for the rest of the cuprates.

[12] Note that we did not introduce such a small cluster before because it will only be used in Sec. 7 to represent diagrammatically the energies of the highest occupied molecular orbitals. Such a diagram is much clearer for a small cluster made of only one Cu atom.

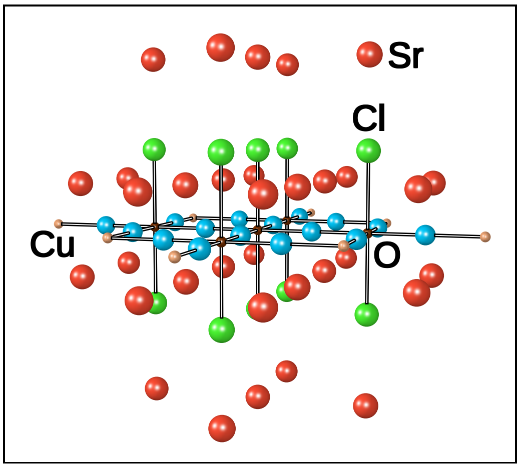

Figure 8: The $Cu_5O_{16}Cl_{10}/Cu_8Sr_{34}$ cluster with 31 atoms in the core and 42 atoms represented with pseudopotentials.

All atomic positions are located according to the tetragonal phase with lattice constants adopted from [85] with lattice parameters $a = b = 3.9625$ Å and $c = 15.5303$ Å. Although $Sr_2CuO_2F_{2+\delta}$ was found in the orthorhombic phase we neglected its orthorhombicity (since the precise structure has not been established [11]) and also use the idealized K_2NiF_4 structure here. For simplicity we only modified the position of the F atoms.

3.3 Charge assignment

The values chosen for the background point charges constituting the Madelung region are based on the formal valence of the constituents. In clusters representative of $YBa_2Cu_4O_8$ the formal valences have to be slightly modified in order to reach charge neutrality. These values for all clusters used in this work are listed in Table 4. This charge assignment made for the point charges is of course not unique and other groups like Kaplan *et al.* [64] following works from Gupta and Gupta [45] made different charge assignments and as a consequence the number of electrons in their clusters is also different.

3.4 Simulation of doping

Finally we would like to describe the simulation of doping with the cluster method. For more details about this method we refer to Stoll *et al.* [120, 121]. There are several aspects to be considered when studying the change of the electronic structure upon doping copper oxides. If the doping is produced by impurity atoms (as for example replacing La^{3+} by Sr^{2+} in La_2CuO_4 or Nd^{3+} by Ce^{4+} in Nd_2CuO_4) one can investigate the local changes in the

	Nd		Cu	O(p)	O(o)		
Nd_2CuO_4	+3		+2	−2	−2		
	La		Cu	O(p)	O(a)		
La_2CuO_4	+3		+2	−2	−2		
	Y	Ba	Cu(2)	O(p)	O(a)	Cu(1)	O(ch)
$YBa_2Cu_3O_7$	+3	+2	+2	−2	−2	+2	−1
$YBa_2Cu_4O_8$	+3	+2	+2	−2	−1.5	+2	−2
	Sr		Cu	O(p)	Cl(a)		
$Sr_2CuO_2Cl_2$	+3		+2	−2	−1		

Table 4: Charge assignment made for the different clusters used in this work. The out-of-plane oxygens in Nd are denoted by O(o). The chain oxygens in the yttrium familly are denoted by O(ch).

immediate neighborhood of the impurity atoms. There have been several studies reporting changes in the local structure around dopants (for example Sr in La_2CuO_4) due to holes in cuprates (the holes being “pinned” around the dopant) but these studies pertain to localized holes in the *insulating* phase. In contrast we would like to investigate mobile holes in the *metallic* state. In band-structure calculations the effect of doping is often considered in the rigid-band model in which just the Fermi level is adjusted. It is controversial whether this is justified in cuprates [97].

In this work both electron doped (Nd_2CuO_4) and hole doped (La_2CuO_4) materials are be studied. We are using two different methods to simulate doping. With the first method *hole* doping is achieved by simply *removing* an electron from the cluster and redoing the calculation. Equivalently *electron* doping is achieved by *adding* an electron to the cluster. It is important to realize that there is a change of the spin state for this doping method. Note that the nature of the dopant is not specified. The corresponding doping level is of 20% for a Cu_5 cluster, 10% for a Cu_9 cluster, and 7.7% for a Cu_{13} cluster. That is with this method we are not able to reach every doping level.

The second method simulate doping by introducing additional point charges at the periphery of the cluster to set up an electric field across the cluster in order to move the charge towards or away form the target atoms in the cluster center. We call this method the *peripheral charge method*. The electric field is easily applied with the required symmetry by adding an array of point charges around the periphery of the cluster. This added system of charges has no physical interpretation except that it can be continuously altered so that the charge can be progressively directed to or extracted from the target atoms in the center of the cluster. This implies that the cluster must be sufficiently large so that ions of interest are not near the cluster edge. In contrast to the first method the cluster and the system of charges keep the same number of electrons and the same spin state, but using a Mulliken population analysis approach, the charge of the cluster can be progressively changed in a manner expected by doping. This model has only a limited range of applicability and it has to break down for high doping levels since no electron is actually removed or added. This approach is only concerned with movements of charges and not electrons spins, which are more appropriate in the discussion of holes. The peripheral charge method serves to continuously interpolate the results already obtained for the first method. As we will see in Sec. 4 the peripheral charge method fits surprisingly well with the results obtained by the first method.

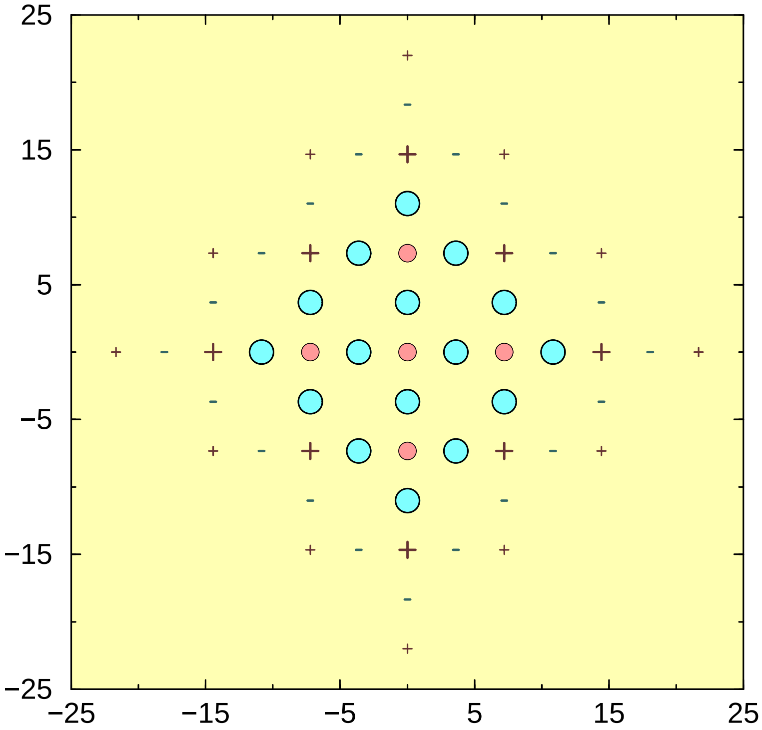

Figure 9: Schematic illustration of the peripheral charge method used for the Cu_5 cluster for the La_2CuO_4 compound. The illustration represents the 5 cooper atoms (red), the 16 planar oxygen atoms (blue), and additional point charges (+ and - signs). The additional plus signs are at the locations of Cu atoms and the minus signs at the locations of oxygen atoms. We have tried to indicate the relative magnitude of each charge by the size of the + and - signs.

The peripheral charge method is illustrated in Fig. 9 for the Cu_5 cluster for La_2CuO_4. In this case we have added three shells of *additional* point charges q_j (j=1,...,n) in the CuO_2 plane. The first shell with charges q_1 was placed at the Cu sites with a distance of $2a$ form the central copper and at the seven other equivalent sites. In the next shell charges q_2 with signs opposite to q_1 are put on the 20 oxygens sites and finally charges q_3 on the 12 coppers forming the next shell. The ratios q_2/q_1 and q_3/q_1 are chosen such that the induced changes in the potential in the central region are nearly identical for all five copper and the four oxygens atoms and that, of course, charge neutrality is observed. It is easy to generalize this method on the one hand for electron doping by just inverting the signs of the peripheral charges and on the other hand for bigger clusters.

4 Calculation of the electronic structure of the electron doped cuprate $\mathrm{Nd_2CuO_4}$

The results of the present section have been published in Ref. [26]. As mentioned in the introduction it is possible to dope cuprates with electrons. For these so called *electron doped* (or n-type) cuprate superconductors the charge carriers are electrons. The first electron doped material was discovered by Tokura *et al.* [130]. This is the $\mathrm{Nd_2CuO_4}$ compound which becomes a superconductor by replacing a certain amount of Nd (3^+) atoms by Ce (4^+) to obtain $\mathrm{Nd_{2-x}Ce_xCuO_4}$. It has a maximal T_c of 22 K for x=0.15. Note that Nd can be also replaced by other rare-earth ions like Pr (3^+) or Sm (3^+) to obtain $\mathrm{M_{2-x}Ce_xCuO_4}$ with M=Pr,Sm. It crystallizes in the so called T' phase structure which can be seen in Fig. 10 where it is compared with the crystal structure of $\mathrm{La_2CuO_4}$. The main structural difference between $\mathrm{Nd_2CuO_4}$ and $\mathrm{La_2CuO_4}$ is the absence of apex oxygens in the former[13]. Later, another type of electron doped material was discovered [117]. It is the so called "infinite layer" compound. The parent compound is $\mathrm{SrCuO_2}$ and superconductivity can be achieved by doping with La to obtain $\mathrm{Sr_{1-x}La_xCuO_2}$. The crystal structure of $\mathrm{SrCuO_2}$ is the simplest among the cuprates and can also be seen in Fig. 10. It has a maximum T_c of 42 K for x=0.1.

4.1 Some experimental facts: the differences between electron doped and hole doped cuprates

The electron doped materials were much less studied by the HTSC community than the hole doped materials. One reason for this may be the relative low T_c showed by these materials compared to the hole doped cuprates. Another reason is certainly the technical difficulty in growing the electron doped materials compared to the hole doped substances (see below). It is now a well established fact that some properties of the electron doped cuprates are different from those of hole doped cuprates. There seems to be a large electron-hole asymmetry in the cuprate materials.

Let us start with Fig. 2 where the generic phase diagram of both hole doped and electron doped cuprates are compared. Although at first sight the phase diagrams appear similar they are in fact not truly symmetric. As described in Sec. 1 for hole doped cuprates in the under- and optimally doped region, the normal state properties below a crossover temperature T^* (the so called pseudo-gap phase) are significantly different from those of the Fermi liquid, and the electronic density of states (DOS) appears to be slightly suppressed. The doped holes are believed to enter into the oxygen p-orbitals in

---

[13] Theoretically it should be possible to dope $\mathrm{La_2CuO_4}$ with electrons but it is practically impossible to grow such crystals. The absence of apical oxygens in the crystal structure seems to favor electron doping.

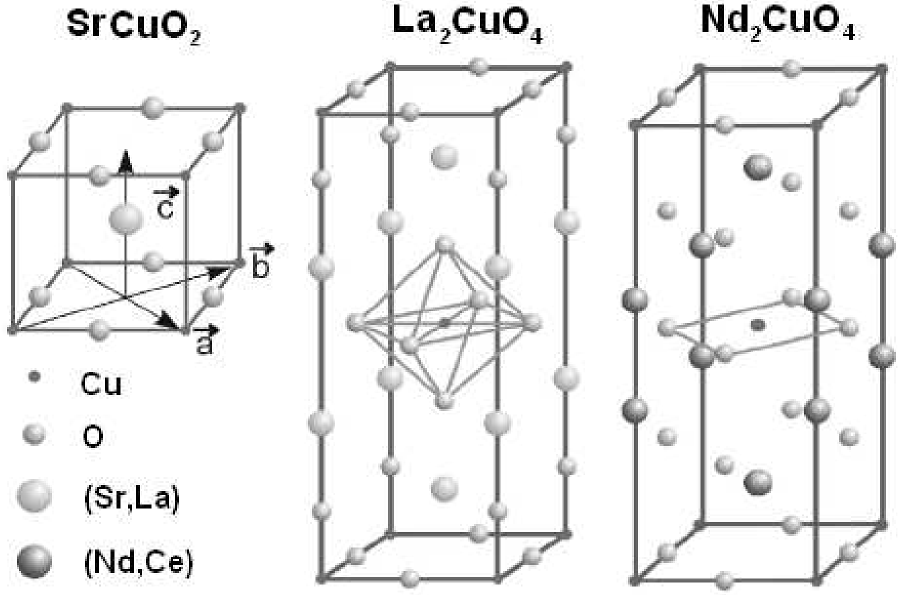

Figure 10: Comparison of the crystal structure of the infinite-layer $Sr_{1-x}La_xCuO_2$ (left), the one-layer hole doped La_2CuO_4 with T structure (middle) and the one-layer electron doped Nd_2CuO_4 with T' structure (right).

the CuO_2 planes. In electron doped cuprates however, the extra electrons induced by doping are believed to enter into the d-orbital of Cu, giving rise to spinless Cu^+-ions that dilute the background antiferromagnetic Cu^{2+}-Cu^{2+} coupling without inducing as strong spin frustrations as those in the hole doped cuprates. The fact is that for electron doped materials the Néel state is much more robust and survives over a larger range of (electron) doping (the antiferromagnetic ordering drops precipitously when approaching x=0.13), in contrast to the hole doped cuprates, whereas the superconducting phase in the electron doped cuprates exists over a much narrower doping range (i.e. $15-18\%$) relative to the hole doped cuprates (i.e. $5-28\%$). Other important differences between electron doped and hole doped cuprates include the absence of a pseudogap in the former and different doping dependence of the Fermi surface as seen by ARPES experiments [15]. To be more precise recent STM experiments performed in high magnetic fields on $Pr_{2-x}Ce_xCuO_{4-y}$ by Alff *et al.* [9] have demonstrated that there is actually a pseudogap in electron doped cuprates when the superconductivity is suppressed. In absence of a magnetic field which suppresses superconductivity the pseudogap phase seems to coexist with the superconducting phase and is somehow "hidden" behind it. That is why the pseudogap does not appear on the left side of Fig. 2. Furthermore in $Sr_{1-x}La_xCuO_2$ the coherence length in the c direction has been measured to be $\xi_c = 5.2$ Å [68] which is larger than $c = 3.5$ Å, the lattice constant in the c direction, which implies three dimensional superconductivity. A simple argument for this fact is that the copper oxide planes are much closer to each other than in the other cuprates (i.e. there is only one layer of Sr between two planes). This of course implies a stronger coupling between the planes and a departure from a quasi-two-dimensional behaviour. This may lead to additional complications for the theoretical description of the infinite layer compound.

What the symmetry of the order parameter in the electron doped cuprates should be is not clear yet in contrast to the hole doped cuprates. As pointed out by Yeh [149] and Shengelaya [111] there are contradictions between the different experiments and this even for optimally doped compounds. Penetration depth [71], ARPES [15, 110], tricrystal [131], Raman scattering [28] and specific heat [18] experiments are in favour of d-wave symmetry. This is in contradiction with tunneling spectroscopy [66, 6, 37], pair breaking and other penetration depth experiments [7, 68, 115] which have evidences for an s-wave symmetry.

Furthermore, as pointed out by Shengelaya [111], the electron doped HTSC have a much higher superfluid density compared to hole doped HTSC. They do not follow the famous Uemura plot where T_c is plotted as a function of ρ_s for different compounds (the superfluid density). This plot shows a linear behaviour for the hole doped cuprates but the electron doped cuprates cannot be put on this line. As pointed out by Yeh [149] the lack of electron-hole symmetry suggests that the cuprates cannot be fully described by a one-band Hubbard or t-J model since this model is electron-hole symmetric. Nevertheless a global theory of HTSC cuprates should also contain the electron doped materials.

Although these materials could be very important for a complete understanding of the HTSC phenomenon they have led to a lot of experimental difficulties which perhaps made the research less active for this type of material. With recent experimental progress it has been possible to "cure" some of these problems. The first problem which experimentalists have to face is the presence of large magnetic moments from rare-earth ions $(\mathrm{Nd,Pr,Sm})_{2-x}\mathrm{Ce}_x\mathrm{CuO}_{4-\delta}$ which have made it difficult to investigate the local magnetic properties of these materials, in particular NMR properties. This problem has been partially resolved by the synthesis of three different electron doped materials: (1) $\mathrm{Pr}_{1-x}\mathrm{LaCe}_x\mathrm{CuO}_{4-\delta}$ ($T_c = 24K$) which helps to eliminate the magnetic moments due to the rare earth ions and where single crystals are available, (2) $\mathrm{La}_{2-x}\mathrm{Ce}_x\mathrm{CuO}_{4-\delta}$, (which has the T' structure) and (3) the infinite layer compound. A further problem is that oxygen reduction is absolutely necessary[14] to induce superconductivity in $(\mathrm{Nd,Pr,Sm})_{2-x}\mathrm{Ce}_x\mathrm{CuO}_{4-\delta}$, δ being approximatively $0.03 - 0.04$ and the

---

[14] Note that the reason for this necessity is poorly discussed in the literature.

physical properties of these materials are extremely sensitive to the oxygen content as can be seen in the results of Kambe *et al.* [63]. In the case of the infinite layer compounds this oxygen reduction is not necessary. The one disadvantage of $Sr_{1-x}La_xCuO_2$ is that it has to be made by using a high-pressure synthesis technique and incorrect synthesis can lead to site disorder, the partial formation of the one dimentional antiferromagnetic insulator $SrCuO_2$, as well as the antiferromagnetic insulator La_2CuO_4 [142]. A further problem is the difficulty to make large crystals. Recently much progress in this direction has been made.

4.1.1 NMR

Several NMR experiments were performed in the electron doped Nd_2CuO_4 compound [72, 1, 151, 150, 63, 73], the $Pr_{1-x}LaCe_xCuO_{4-\delta}$ compound [154], the infinite layer compound $Sr_{1-x}La_xCuO_2$ [55, 142, 136], and its parent compound $SrCuO_2$ [83]. The first surprising feature of these results is a relatively low ^{63}Cu NQR frequency (ν_Q) measured in the undoped parent compound compared to the hole doped compounds. In the undoped parent compounds the quadrupolar frequency has been measured to be 14 MHz for the Nd_2CuO_4 compound and 7.4 MHz in the infinite layer. This is less by more than a factor of two than La_2CuO_4 (33.0 MHz [54]) and $YBa_2Cu_3O_7$ (31.5 MHz [96]) compounds. The second striking feature of all these experiments is the extreme sensitivity of ν_Q on the doping level. Thus ν_Q is ≤ 2 MHz for $Nd_{1.85}Ce_{0.15}CuO_4$ [63], ≤ 0.5 MHz in $Pr_{0.91}LaCe_{0.09}CuO_{4-\delta}$ [154] and finally ≤ 3 MHz in $Sr_{0.9}La_{0.1}CuO_2$ [142].

This strong doping dependence of the field gradient in the electron-doped compounds cannot be quantitatively explained [119] by simplistic ionic models [118] [15].

In the present section we report on cluster calculations of the local electronic structure in Nd_2CuO_4 and its changes upon electron doping. The results are compared to those for hole-doped La_2CuO_4. The contributions to the EFG are studied in detail and it is explained why the EFG values in Nd_2CuO_4 are much smaller than in the hole-doped substances.

4.2 Electronic structure of Nd_2CuO_4 studied by cluster calculations

We propose here a detailed calculation of the electronic structure of Nd_2CuO_4 with the cluster method. The clusters that we have used for this chapter are described in detail in Sec. 3.2.2. We also simulated doping with two methods which are described in Sec. 3.4.

---

[15] In Ref. [153] it has been proposed that the $3d_{x^2-y^2}$ orbitals are fully occupied and therefore do not give any contribution to the field gradient if all other 3d orbitals are occupied.

4.2.1 Charge distribution

The total electron density distribution is an observable and its accuracy can in principle be tested experimentally. However, its usefulness for qualitative models is limited. A well established procedure is to partition the density in terms of atomic orbitals so that the behaviour can be associated with the properties of a small number of atoms. In cluster calculations, the charge distribution is determined by the occupied molecular orbitals (MOs). The m^{th} MO is represented as a linear combination

$$\phi_m(\vec{r}) = \sum_{K=1}^{n} \phi_m^K(\vec{r} - \vec{R}_K) = \sum_{K=1}^{n} \sum_{k=1}^{n_K} c_m^{K,k} B_{K,k}(\vec{r} - \vec{R}_K) \tag{31}$$

of n_K atomic basis functions $B_{K,k}$ centered at the nuclear sites $K = 1, \ldots, n$, and the $c_m^{K,k}$ are the MO coefficients[16]. The charge density is then given by $\sum_m \phi_m(\vec{r})^2$ and contains both on-site and overlap terms. Although atomic orbitals do not strictly exist in molecules it is possible to identify functions centered on nuclei which possess all the characteristics (number of nodal surfaces and angular properties) which correspond to hydrogen-like atomic orbitals. For example in our calculations we can identify a function in the molecular orbitals which is spherically symmetric about the central copper nucleus with three spherical nodal surfaces corresponding to a 4s hydrogen-like orbital. The most commonly used method of achieving this partition is the *Mulliken population analysis* [89, 124]. This procedure is clearly defined and accounts for the whole electron population although there is some concern how the overlap densities are apportioned to the individual basis orbitals.

To discuss the charge distribution we have analyzed the partial occupancies p_c according to the Mulliken population analysis of the various atomic orbitals. These are represented in the left part of Fig. 11 for the relevant orbitals: $3d_{x^2-y^2}$, $3d_{3z^2-r^2}$, and 4s for Cu and $2p_\sigma$ for O(p). All other orbitals have occupancies that differ only marginally ($< 0.2\%$) from 2. Results have been obtained from calculations with clusters of three different sizes: Cu_5O_{16}/Cu_8Nd_{24} with spin multiplicity M=4, $Cu_9O_{24}/Cu_{12}Nd_{32}$ with M=2, and with $Cu_{13}O_{36}/Cu_{12}Nd_{48}$ with M=6 for the undoped case. These calculations have been repeated with one additional electron and with M=3, 1, and 5 for Cu_5, Cu_9, and Cu_{13}, respectively. This doping simulation changes the total charge in the unit cell. We therefore define a quantity $\rho(3)$ as the sum of the Mulliken charge on the central copper atom and that on the adjacent oxygen atoms,

$$\rho(3) = \rho_{Mull}(Cu) + 2\rho_{Mull}(O_p) + 2, \tag{32}$$

---

[16] For the present discussion we do not need to distinguish the spin orbitals.

which approximately represents the fractional excess charge in the unit cell. Ideally, in the undoped plane $\rho(3)$ should vanish. Due to open boundaries in the cluster method this is not quite exactly the case but since all calculated values are sufficiently close to zero we have used renormalized values for $\rho(3)$ in Fig. 11. The full red symbols are the partial occupancies calculated with the cluster with 5 Cu atoms in the undoped case ($\rho(3) \approx 0$) and with one additional electron at $\rho(3) \approx -0.16$. The blue symbols denote p_c values obtained from a cluster with 13 Cu again in the undoped case and with an additional electron at $\rho(3) \approx -0.05$. The results of the calculation for the cluster with 9 atoms in the undoped case are almost identical to those of Cu_{13} and are not shown for convenience. When adding an electron, however, the results exhibit a peculiar superstructure for which presently we do not have a unique explanation. We just note that although we have assumed a multiplicity M=1 we have use an unrestricted approach. The open symbols, finally, represent partial occupancies that have been deter-

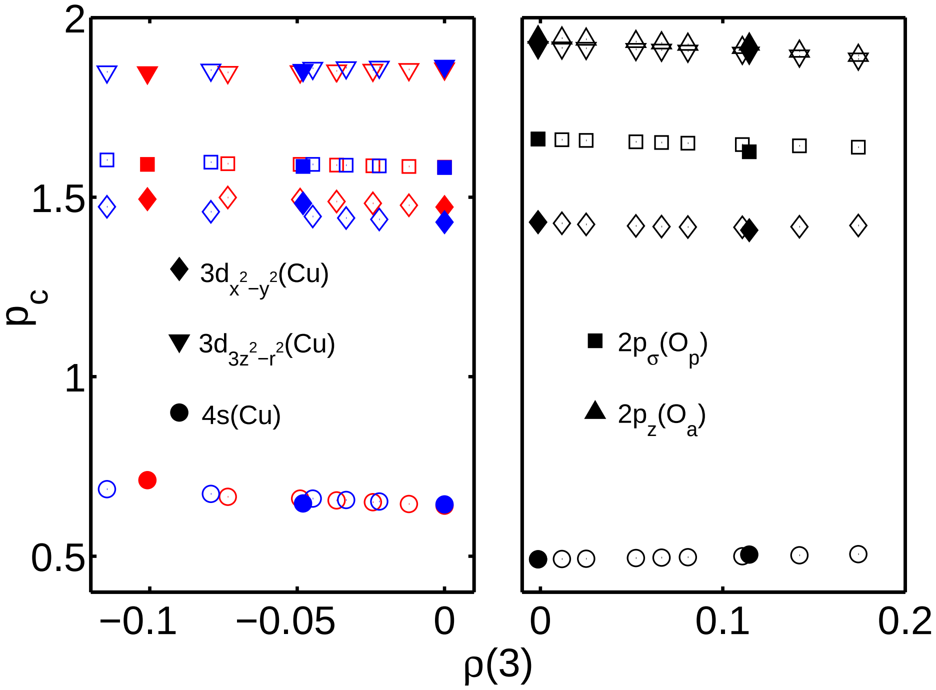

Figure 11: Partial Mulliken populations of the atomic orbitals versus doping level $\rho(3)$ for $La_{2-x}Sr_xCuO_4$ (black) and $Nd_{2-x}Ce_xCuO_4$. The following orbitals are represented: $3d_{3z^2-r^2}$ (triangles down), 4s (circles), apical oxygen $2p_z$ (triangles up), $3d_{x^2-y^2}$ (diamonds) and the planar oxygen $2p_\sigma$ (squares). Empty symbols refer to peripheral charge calculations and filled symbols refer to normal doped calculations where electrons are added or removed as appropriate.

mined with the peripheral charge method described in Sec. 3.4 that allows to simulate the doping with fractional charges. These values have been obtained with the 5 (13) Cu cluster and result from calculations that all used the same spin multiplicity M= 4 (M=6) as in the undoped case. It is seen that in the undoped case the partial occupancies only marginally depend on the cluster size. As a function of doping the p_c values calculated for the three differently sized clusters (filled symbols) change monotonically and are reasonably well interpolated by those obtained with the peripheral charge method (open symbols). For a general discussion it is instructive to compare these results with those obtained previously by Stoll *et al.* [120] for hole doped $La_{2-x}Sr_xCuO_4$ which are shown in the right part of Fig. 11. Note that in this case $\rho(3)$ is defined by

$$\rho(3) = \rho(\mathrm{Cu}) + 2\rho(\mathrm{O}_p) + 2\rho(\mathrm{O}_a) + 2\rho(\mathrm{La}). \tag{33}$$

Again, the full symbols denote partial occupancies of the relevant AO calculated for the undoped material ($\rho(3) \approx 0$) for the cluster with 5 Cu atoms with M=4 and with one electron less and M=3 ($\rho(3) \approx 0.12$). The open symbols are obtained from calculations with the peripheral charge method. Comparing the left and right sides of Fig. 11 shows first that there are no drastic differences between the electron and hole doped materials although the latter have apical oxygens whose $2p_z$ orbitals are not completely filled. The occupancies of the Cu $3d_{x^2-y^2}$ (diamonds) orbital and the O $2p_\sigma$ orbital (squares) which carry most of the spin density slightly decrease from left to right. There is of course a jump at $\rho(3) = 0$ which is due to the different structures. It is remarkable that the Cu $3d_{3z^2-r^2}$ AO (triangles down) in the electron doped material is less occupied than in La_2CuO_4. This is compensated by a significantly larger occupancy of the Cu 4s AO (circles). In Fig. 12 the density difference in the 4s and $3d_{3z^2-r^2}$ AOs between the $Cu_{13}O_{36}/Cu_{12}Nd_{48}$ and $Cu_{13}O_{62}/Cu_{12}La_{74}$ is shown which demonstrates the increased population of the 4s at the expense of the $3d_{3z^2-r^2}$ AO.

The quality of the results of these calculations can be assessed by comparing the electric field gradients (EFG) with experiments. EFGs are very sensitive to the charge distribution: An increase in $p_c(3d_{x^2-y^2})$ by 0.1 implies a decrease in V_{zz} by $0.1< r^{-3} > \times 4/7 \approx 0.46$ since $< r^{-3} > \approx 8\ a_B^{-3}$. Precisely the same decrease in V_{zz} can be achieved by a decrease in $p_c(3d_{3z^2-r^2})$ by 0.1. From Fig. 11 it is thus evident that the calculated main component V_{zz} for the Cu EFG is considerably smaller in the e-doped materials than in $La_{2-x}Sr_xCuO_4$. This has indeed been observed in various experiments but has been attributed to an increase in $p_c(3d_{x^2-y^2})$ only. It should be emphasized that in general theoretical results for EFG values V_{ij} become less reliable the smaller the values of $|V_{ij}|$ are. This is related to the natural

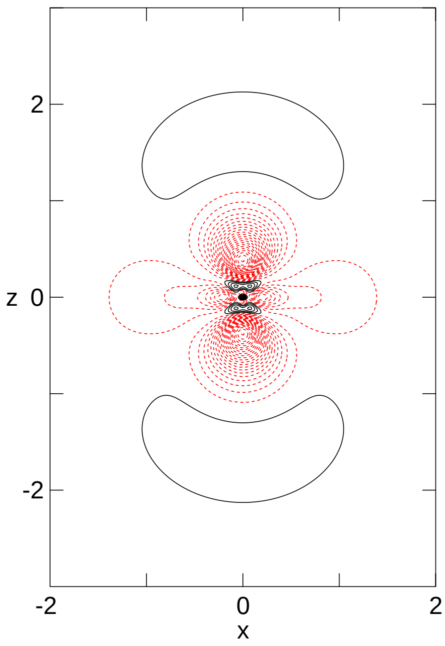

Figure 12: Electron density difference contour plots in the x-z plane (perpendicular to the CuO_2 plane) between the $Cu_{13}O_{36}/Cu_{12}Nd_{48}$ and the $Cu_{13}O_{62}/Cu_{12}La_{74}$ clusters on a area of 4 a_B × 6 a_B. The wave functions of the cluster electrons have been projected onto the 4s and the $3d_{3z^2-r^2}$ states. The solid density lines (black) occur when the local electron density of the cluster containing Nd is larger than the electron density of the cluster containing La. Dashed lines (red), on the other hand, denote that the local electron density is larger in the La containing cluster. Two neighboring lines (solid and dashed) are separated by an electron density difference of 0.01 e/a_B^3.

choice of atomic orbitals. In spherically symmetric environment, $^{63}V_{ij} = 0$ for a Cu $3d^{10}$ state. This vanishing is mathematically a cancellation of the contributions of the five individual d-shell contributions α where each provides a value $^{63}V_{zz} = m\frac{1}{7}\langle r^{-3}\rangle p_\alpha$ with m=4, -4, 2, 2, and -4 for $3d_{x^2-y^2}$, $3d_{3z^2-r^2}$, $3d_{yz}$, $3d_{xz}$, and $3d_{xy}$, respectively. Small departures of the occupancies p_α from 2 distort this balance, due to a shift from the spherical symmetry.

4.2.2 Sensitivity of EFG values on charge distribution

A detailed description of the evaluation of EFGs in the framework of cluster calculations is found in Ref. [119]. Here we just point out the relevant aspects that are connected to the rearrangement of charge distributions due

		undoped ($M=6$)	e doped ($M=5$)
I	reminder	0.755	0.797
	p	-1.431	-1.433
	$d_{x^2-y^2}$	-6.378	-6.613
	d_{xy}	-9.128	-9.088
	$d_{3z^2-r^2}$	8.309	8.222
	d_{xz}	4.528	4.512
	d_{yz}	4.528	4.512
II	s	-0.003	-0.002
	p	0.013	0.013
	$d_{x^2-y^2}$	-0.021	-0.020
	d_{xy}	0.001	0.001
	$d_{3z^2-r^2}$	-0.585	-0.616
	d_{xz}	0.000	0.000
	d_{yz}	0.000	0.000
III + Nuclei		-0.015	-0.017
Point charges		-0.033	-0.033
Total		0.538	0.234

Table 5: Contributions I, II, III to the EFG component V_{zz} in atomic units, calculated with DF/GGA for the $NdCu_{13}$ compound cluster, (undoped with spin multiplicity 6 and electron doped with M=5).

to electron doping.

We assume in the following that the target nucleus K_T is at $\vec{R}_{K_T} = 0$. The contribution of the MO ϕ_m to the EFG at K_T is given by the matrix element

$$V_m^{ij} = \langle\, \phi_m(\vec{r})|\, \frac{3x^i x^j - r^2\delta^{ij}}{r^5}\, |\, \phi_m(\vec{r})\,\rangle$$

$$= \sum_{K=1}^{n}\sum_{L=1}^{n}\sum_{k=1}^{n_K}\sum_{l=1}^{n_L} c_m^{K,k} c_m^{L,l} \times$$

$$\times \langle\, B_{K,k}(\vec{r} - \vec{R}_K)|\, \frac{3x^i x^j - r^2\delta^{ij}}{r^5}\, |\, B_{L,l}(\vec{r} - \vec{R}_L)\,\rangle. \tag{34}$$

This matrix element contains contributions from basis functions centered at two nuclear sites K and L. Thus we can identify three types of contributions: (*i*) on-site terms from basis functions centered at the target nucleus ($K = L = K_T$, contribution I), (*ii*) mixed on-site and off-site contributions (II), and (*iii*) purely off-site terms with $K \neq K_T$ and $L \neq K_T$ (III).

In addition, there is a contribution coming from all nuclear point charges Z_K which we denote by W_{ij}. The charges of the bare nuclei at sites $K \neq K_T$

are screened by the matrix elements with $K = L$. Therefore the combined contributions from III and the nuclei (W_{ij}) are small. The partitioning of the contributions to the EFG tensor V_{ij} thus reads

$$V_{ij} = {}^{I}V_{ij} + {}^{II}V_{ij} + {}^{III}V_{ij} + W_{ij}. \tag{35}$$

More details about these regional partitions can be found in Ref. [119].

We collect in Table 5 the various contributions to V_{zz} at the copper obtained for the $Cu_{13}O_{36}/Cu_{12}Nd_{48}$ cluster for both the undoped and the electron-doped calculations. EFGs are given in atomic units (1 a.u. corresponds to 9.717×10^{21} eV/m^2). In the undoped case, the total value $V_{zz} = 0.538$ is obtained from contributions I (0.428), II (0.160), III + nuclei (-0.015) and a small correction due to the surrounding point charges (-0.033). In the electron-doped case the total EFG of $V_{zz} = 0.235$ is substantially smaller which is mainly due to a diminished contribution from region I.

Focusing on region I we note that the added contributions from the three AO $3d_{xy}$, $3d_{zx}$, and $3d_{yz}$ are -0.072 (undoped) and -0.064 (doped).

A careful analysis of Table 5 shows that the most significant difference is due to the $d_{x^2-y^2}$ and the $d_{3z^2-r^2}$ parts of contribution I. Only very small corrections are obtained by the other contributions. The influence of part III of the electrons on the other atoms is nearly fully compensated by the nuclear charges of these atoms and contributes only by a very small amount. To understand the changes of the EFG on the copper sites upon doping, it is therefore sufficient to concentrate on the MOs which contain partially occupied $3d_{x^2-y^2}$ and $3d_{3z^2-r^2}$ AOs at the target nucleus. The EFG is then given by

$$V_{zz} = R + \frac{4}{7}(N_{3z^2-r^2}\langle\, r^{-3}\,\rangle_{3z^2-r^2} - N_{x^2-y^2}\langle\, r^{-3}\,\rangle_{x^2-y^2}), \tag{36}$$

where R is the contribution from all other orbitals and N are the partial occupation numbers of the corresponding orbitals which are gathered in Table 6.

The fact that the partial occupation numbers N of the AOs are very similar to the partial Mulliken populations p_c which are also included in Table 6 gives evidence that despite their simplistic concept the Mulliken charges can be significant quantities in the analysis of charge distributions in cuprates. In particular, the differences $N_{3z^2-r^2} - N_{x^2-y^2}$ and $p_c(3d_{3z^2-r^2}) - p_c(3d_{x^2-y^2})$ are very similar. In Sec. 6.4.1 we will therefore use a simplified version of Eq. (36) for a more general analysis of the Cu EFGs in cuprates.

4.2.3 Comparison with experiments

The connection between a calculated EFG and a measured NQR frequency is given in Sec. 2.2.3. If we adopt the value of the quadrupole moment

$^{63}Q = -0.211$ b derived by Sternheimer [118] we obtain from our calculations a quadrupolar frequency of $^{63}\nu_Q = 13.3$ MHz in the undoped Nd_2CuO_4 which is in very good agreement with the experimental value of $\nu_Q = 14$ MHz reported by Abe *et al.*[1]. In the electron-doped materials we get $^{63}\nu_Q = 5.8$ MHz in the Cu_{13} cluster (corresponding to a doping level of about 8 %) and $^{63}\nu_Q = 3.6$ MHz in the Cu_5 cluster (corresponding to 20 % doping). Experimental values for quadrupole frequencies in doped materials are generally much smaller than in the undoped case and close to zero ($\nu_Q < 2$ MHz in Ref. [63] for a doping level of 15 %). This reduction compared to the undoped substance is at least qualitatively reproduced by our calculations.

	undoped		electron-doped	
	$3d_{x^2-y^2}$	$3d_{3z^2-r^2}$	$3d_{x^2-y^2}$	$3d_{3z^2-r^2}$
N	1.379	1.820	1.435	1.806
p_c	1.430	1.865	1.483	1.856
$\langle r^{-3} \rangle$	8.094	7.991	8.064	7.968

Table 6: Partial occupation numbers N, partial Mulliken populations p_c, and expectation values $\langle r^{-3} \rangle$ for the relevant copper AOs in undoped ($M = 6$) and doped ($M = 5$) Cu_{13} clusters representative of Nd_2CuO_4.

4.2.4 General aspects of Cu EFG

It is often assumed (by making use of the simple ionic model) that the EFG can be used to give an estimate of the partial Mulliken population, $p_c(3d_{x^2-y^2})$, of the Cu $3d_{x^2-y^2}$ orbital. This is of course only true if one assumes that all the other d orbitals are fully occupied. If the population, $p_c(3d_{3z^2-r^2})$, of the Cu $3d_{3z^2-r^2}$ orbital is also less than 2, Eq.(36) must be used for the description of the EFG. If we replace the occupation numbers in Eq.(36) by the partial Mulliken populations and if we assume that $\langle r^{-3} \rangle$ is similar for all 3d orbitals we arrive at the following simplified formula:

$$V_{zz} \approx \frac{4}{7}\langle r^{-3}\rangle \Delta_d + R. \tag{37}$$

Here $\Delta_d = p_c(3d_{3z^2-r^2}) - p_c(3d_{x^2-y^2})$. In Table 7 we have collected the relevant partial Mulliken populations $p_c(3d_{x^2-y^2})$ and $p_c(3d_{3z^2-r^2})$ together with Δ_d and V_{zz} for several cuprates (including $YBa_2Cu_3O_6$ (Ref.[109]), $YBa_2Cu_3O_7$ (Ref. [106]), $YBa_2Cu_4O_8$ (Ref. [109]), and $Sr_2CuO_2Cl_2$ (see Sec. 7)). For further reference Table 7 also contains the 4s populations. In Fig. 13 we have plotted V_{zz} versus Δ_d for various cuprates. The linear correlation is evident and we thus conclude that the changes in V_{zz} depend almost entirely on the populq ation of the $3d_{x^2-y^2}$ and the $3d_{3z^2-r^2}$ orbitals. This modification of the ionic model tells us that a small value of V_{zz} can also be obtained by an appropriate population difference of the $3d_{3z^2-r^2}$ and $3d_{x^2-y^2}$ AOs.

Substance	Mulliken populations					
	$3d_{x^2-y^2}$	$3d_{3z^2-r^2}$	4s	Δ_d	V_{zz}	c_s
La_2CuO_4	1.4061	1.9223	0.5015	0.5162	1.1862	0.2220
Nd_2CuO_4	1.4303	1.865	0.6470	0.4347	0.5737	0.3012
$Nd_{1.92}Ce_{0.08}Cu_4$	1.4829	1.8535	0.6442	0.3706	0.2699	0.3123
$YBa_2Cu_3O_7$	1.4227	1.9142	0.5899	0.4915	1.047	0.2395
$YBa_2Cu_4O_8$	1.4268	1.9087	0.5920	0.4819	0.9863	0.2468
$YBa_2Cu_3O_6$	1.4278	1.9015	0.6178	0.4737	0.8072	0.2579
$Sr_2CuO_2Cl_2$	1.4495	1.8993	0.5250	0.4498	0.7180	0.2528

Table 7: Partial Mulliken populations of the $3d_{x^2-y^2}$ and $3d_{3z^2-r^2}$ orbitals, their difference Δ_d, and the calculated EFG for La_2CuO_4, undoped and electron-doped Nd_2CuO_4, three substances of the YBaCuO family, and $Sr_2CuO_2Cl_2$ for Cu_{13} clusters.

4.2.5 Discussion of the role of the $3d_{3z^2-r^2}$ and 4s orbitals:

In the discussion above we did not discuss the 4s orbital. As can be seen on Table 7 the *increase* in occupancy of the Cu 4s orbital seems to accompany a *decrease* in the Cu $3d_{3z^2-r^2}$. From Eq. (37) the indirect effect of the increased occupancy of the 4s orbital will be reflected in the EFG. We propose now a modification of the MO diagram 14 which change our perception of the bonding.

The $3d_{3z^2-r^2}$ and 4s orbitals belong to the same symmetry species in D_{4h} symmetry, and therefore can hybridise (mix) freely. The resulting orbital pair can be written as: $\phi_h = c_s\phi_{4s} + c_d\phi_{3d_{3z^2-r^2}}$ where $c_s^2 + c_d^2 = 1$, noting that ϕ_{4s} and $\phi_{3d_{3z^2-r^2}}$ are orthogonal. ϕ_h is effectively the $3d_{3z^2-r^2}$ orbital because c_s is small and $\phi_h^\star$ is effectively the 4s orbital. We define c_s so that the ϕ_h orbital is fully occupied, so it is entirely non-bonding, sometimes referred to as a lone pair. The value of c_s can be calculated from the formula

$$c_s^2 = \frac{2 - \rho_{3d_{3z^2-r^2}}}{4 - \rho_{3d_{3z^2-r^2}} - \rho_{4s}} \tag{38}$$

where,

$$c_d^2 = 1 - c_s^2. \tag{39}$$

This ensures that ϕ_h is doubly occupied. The argument for this equation is as follows: Instead of using orbitals ϕ_{4s} and $\phi_{3d_{3z^2-r^2}}$ we define hybrid orbitals

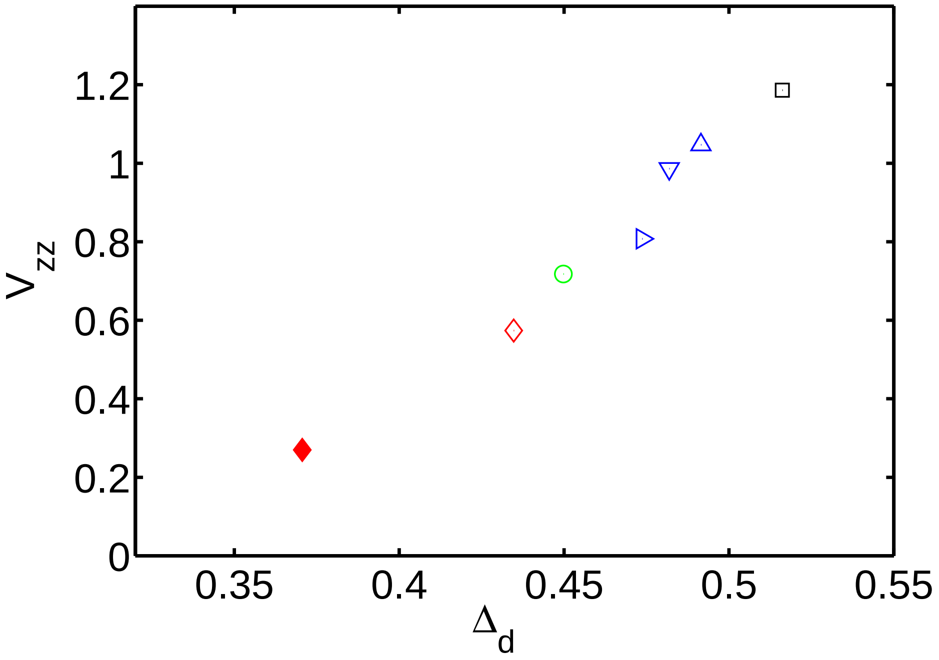

Figure 13: Main component V_{zz} of the copper EFG in atomic units versus Δ_d=$p_c(3d_{3z^2-r^2})-p_c(3d_{x^2-y^2})$ for La_2CuO_4 (black square), $YBa_2Cu_3O_7$ (blue triangle up), $YBa_2Cu_4O_8$ (blue triangle down), $YBa_2Cu_3O_6$ (blue triangle right), $Sr_2CuO_2Cl_2$ (green circle), Nd_2CuO_4 (red diamond), $Nd_{1.92}Ce_{0.08}CuO_4$ (full red diamond).

ϕ_h and $\phi_h^\star$ as above. The Mulliken charge in ϕ_h is assumed to be 2 and $(\rho_{4s}+\rho_{3d_{3z^2-r^2}}-2)$ in ϕ_h^*. This ensures that the Mulliken charge distribution is the same as the unhybridized orbitals. The Mulliken population of the 4s orbital in ϕ_h is $2c_s^2$ and in the ϕ_h^* is $(\rho_{3d_{3z^2-r^2}}+\rho_{4s}-2)(1-c_s^2)$. Hence

$$\rho_{4s} = 2c_s^2 + (\rho_{3d_{3z^2-r^2}} + \rho_{4s} - 2)(1 - c_s^2). \tag{40}$$

We can do the same for the $3d_{3z^2-r^2}$ orbital as follows

$$\rho_{3d_{3z^2-r^2}} = 2(1 - c_s^2) + (\rho_{3d_{3z^2-r^2}} + \rho_{4s} - 2)c_s^2. \tag{41}$$

Either of these equations leads directly to the above expression for c_s. The occupancy of $\phi_h^\star$ is $\rho_c(\phi_h^\star) = \rho_{3d_{3z^2-r^2}} + \rho_{4s} - 2$ and is generally about $p_c(\phi_h^\star) = 0.5$. This means that the effect on the EFG is dominated by the value of $c_d = \sqrt{1-c_s^2}$, that is, the larger c_s is the smaller is the EFG, as shown in Table 7. Only for small c_s is $\phi_h^\star \approx \phi_{3d_{3z^2-r^2}}$, that is, the lone pair density is the density of the $3d_{3z^2-r^2}$ atomic orbital. Increasing c_s simply spreads out the lobes along the z axis (where the apical oxygen are

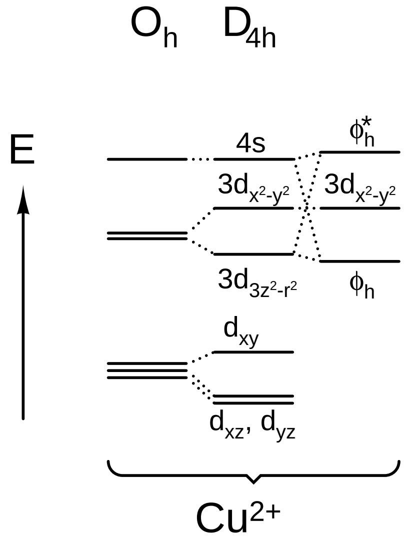

Figure 14: MO diagramm of the Cu^{2+} ion in a O_h and D_{4h} symmetry environment. ϕ_h and $\phi_h^\star$ are the sd-hybrids defined in the text.

normally formed). In Nd_2CuO_4 the missing apical oxygens (see Fig. 10) release space which is dominated by 4 Nd^{3+} ions on each site of the cuprate plane which still benefit from the electron density being oriented along the z axis. This is achieved by mixing the spherical electron distribution of the 4s orbitals. Since ϕ_{4s} makes no contribution to the EFG it is clear that a large c_s will reduce the EFG. Of course $\phi_h^\star$ now has an increased $3d_{3z^2-r^2}$ contribution but the occupancy is only ≈1/4 that of ϕ_h so the effect of this increased contribution is significantly decreased. So contrary to the experimental assertion that it is a function of the occupancy of the $3d_{3z^2-r^2}$ orbital we believe that it is related to the occupancy of the $3d_{3z^2-r^2}$ orbitals which is altered by mixing with the 4s orbital which in turn is governed by the structure of Nd_2CuO_4. Note that this model is unsuitable for the $YBa_2Cu_3O_6$, $YBa_2Cu_3O_7$, and $YBa_2Cu_4O_8$ because they are asymmetrical with respect of the CuO_2 plane.

4.3 Spin density distribution and hyperfine couplings

The spin-polarized cluster calculations allow us to investigate the spin density distribution in detail. In Fig. 23a we depict the spin density distribution along the five Cu and six O obtained for the $Cu_{13}O_{36}/Cu_{12}Nd_{48}$ cluster with spin multiplicity $M = 14$, which corresponds to a ferromagnetic alignment of the copper moments represented in Fig. 23b. Most of the spin density is provided by the singly occupied molecular orbital which is also highest in energy. It is a linear combination of $3d_{x^2-y^2}$ atomic orbitals (AOs) on the coppers ($\approx$ 80%) and $2p_\sigma$ AOs on the oxygens ($\approx$ 20%). The square of the $3d_{x^2-y^2}$ AO has maxima at distances of 0.35 Å from the nucleus but vanishes at the nucleus. In general, the spin density at a nuclear site is due to s-type AOs giving rise to the Fermi contact term. In particular, the spin densities at the Cu nuclei (cusps in Fig. 23a) can be correlated with the Mulliken spin densities (whose signs are given in Fig. 23b) at the same and the nearest neighbor Cu nuclei. This observation can be used to split the Fermi contact term into on-site and transferred terms as has been discussed in detail in Refs. [53, 106]. We just note here that the on-site term is negative if the Mulliken spin density at the Cu atom under consideration is positive and vice versa and that the transferred term is positive (negative) if the Mulliken spin densities at the neighboring Cu atoms is positive (negative). Near the oxygens, the spin density is provided by the $2p_\sigma$ AO and the small cusp at the position of the four innermost oxygen nuclei is due to the transferred hyperfine fields from the electronic moments of the two adjacent copper atoms.

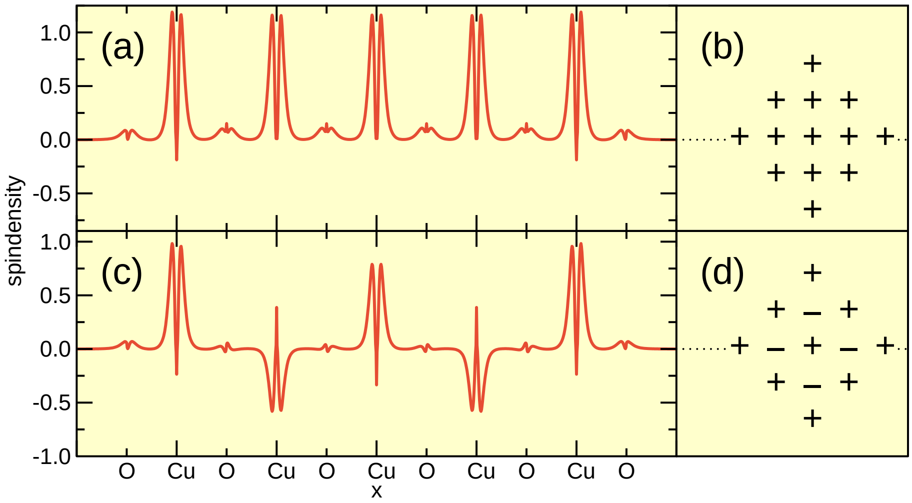

Figure 15: (a) Spin density along the 5 Cu and 6 O in the $Cu_{13}O_{36}/Cu_{12}Nd_{48}$ cluster of spin multiplicity $M = 14$; (c) spin density with multiplicity $M = 6$. (b) and (d) signs of the Mulliken spin densities.

In Fig. 23c we show the spin density distribution obtained with spin multiplicity $M = 6$. For this multiplicity, the total energy is lower than for all other multiplicities and corresponds to an antiferromagnetic alignment of the copper moments represented in Fig. 23d.

From the differences in the total energy of the various spin configurations it is possible to estimate the antiferromagnetic exchange interaction J (see for example Ref. [108]). Preliminary results indicate $J \approx 160$ meV for Nd_2CuO_4 which is about the same as in La_2CuO_4 and slightly larger than in $YBa_2Cu_3O_7$ ($J \approx 130$ meV).

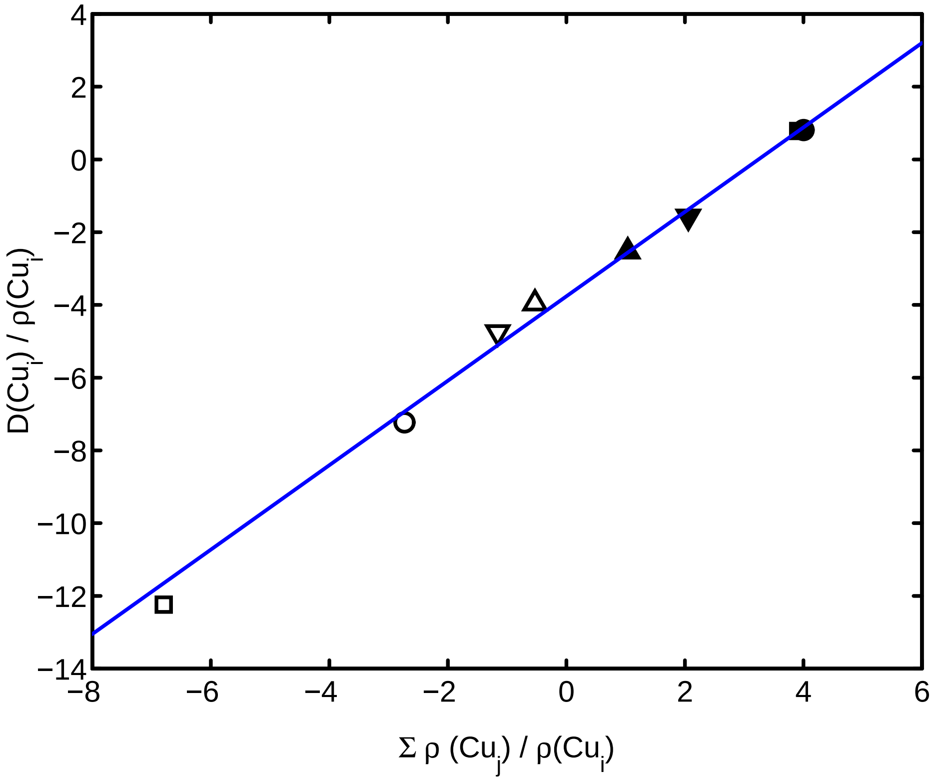

Figure 16: $D(\mathrm{Cu}_i)/\rho(\mathrm{Cu}_i)$ plotted against $\sum_{j\in NN}\rho(\mathrm{Cu}_j)\ /\ \rho(\mathrm{Cu}_i)$. Values for the cluster with multiplicity $M = 14$ ($M = 6$) are plotted with filled (open) symbols. The different markers correspond to symmetrically inequivalent copper sites in the cluster which differ e.g. by their number of nearest neighbors.

The hyperfine coupling tensor at the copper is determined by an on-site term a^{ii}_{tot} and a transferred term b^{ii}_{tot} from the nearest neighbors. The value of a^{ii}_{tot} is made up of three contributions, an isotropic on-site interaction, a_{iso}, a dipolar interaction, a^{ii}_{dip}, and a contribution from spin-orbit coupling, a^{ii}_{so}. The transferred term, b^{ii}_{tot}, is dominated by the isotropic interaction, b_{iso}, since the dipolar term, b^{ii}_{dip}, is small and the influence of spin-orbit coupling is entirely neglected. In Fig. 16 we show the dependence of the isotropic hyperfine density, D_{iso}, at the Cu nucleus on the on-site atomic spin density, ρ_i, and those of the nearest neighbors, ρ_j. The straight line is a fit to the equation

$$D_{iso} = a_{iso} \cdot \rho_i + \sum_j b_{iso} \cdot \rho_j \tag{42}$$

which allows the determination of a_{iso} and b_{iso}. Analogously, the dipolar contributions can be determined. The resulting hyperfine couplings are collected in Table 4.3 and are compared to the values obtained for La_2CuO_4. The total values $a_{tot}^{\|}$ and $a_{tot}^{\perp}$ include spin-orbit terms $a_{so}^{\|} = 2.222$ a_B^{-3} and $a_{so}^{\perp} = 0.394$ a_B^{-3} which have been estimated according to the procedure given in Ref. [53]. We note that the values for the two materials are very similar. The only significant change is in $a_{tot}^{\perp}$, which shows a different sign in the two substances.

	La_2CuO_4	Nd_2CuO_4
a_{iso}	-1.94	-2.42
$a_{dip}^{\|}$	-3.55	-3.38
b_{iso}	0.77	0.75
$b_{dip}^{\|}$	0.08	0.03
$a_{tot}^{\|}$	-3.30	-3.58
$a_{tot}^{\perp}$	0.22	-0.34

Table 8: Comparative table of the hyperfine constants for La_2CuO_4 and Nd_2CuO_4 (in units of a_B^{-3}).

From experiments there is much less information available for the hyperfine couplings in Nd_2CuO_4 than in the hole-doped materials. Zheng *et al.* [154] reported spin shift measurements in $Pr_{2-x}Ce_xCuO_4$ and found, with the field parallel to the c axis, the same temperature independent behavior as has been observed in doped La_2CuO_4 and in the YBaCuO family. The spin shifts measured with field in the plane, however, change with decreasing temperature. This behavior is commonly explained by a coincidental cancellation of the hyperfine coupling contributions in c direction. The theoretical values for $a_{tot}^{\|} + 4b_{tot}^{\|}$ are indeed close to zero. It is intriguing, however, that the same precise cancellation is required in most hole doped materials and in $Pr_{2-x}Ce_xCuO_4$ to explain the temperature independent spin shifts. More information on hyperfine couplings is available for the electron-doped infinite layer compound $SrCuO_2$. There, $a_{tot}^{\perp} + 4b_{tot}^{\perp}$ should vanish to explain the data. Our calculated values give no support for these observations.

5 Impurities in superconductors: an overview

The study of the effect of impurities in solids is one of the most important in solid state physics because it represents the departure from an ideal impurity free case towards a more realistic situation where impurities are present in a given material. A theory which describes how impurities affect certain properties of solids (for example the conductivity), is one of the most difficult tasks and there are still a lot of unsolved problems in this area. Here we will distinguish between two sorts of impurities. It is appropriate to call the first class of impurities *dopants* because by replacing certain atoms of a material by different atoms with different oxidation states (dopants), one can improve certain properties of this material. For example the doping is crucial in achieving the functionality of semiconductors: undoped semiconductors are just band insulators and are absolutely not useful for any kind of application in electronics (it is not possible to build any kind of diode or transistor without doping semiconductors). In the case of HTSC one has to dope the parent compounds[17] in order to obtain a superconducting material[18]. Consequently, sensitivity of a physical system to disorder can be a blessing in disguise. It can lead not only to achieving new applications but also to uncovering the nature of exotic ground states, elucidating the properties of electronic correlations, and producing electronic states that are impossible in the bulk of "ideal" clean systems.

The second type of impurities are the ones which are detrimental for certain properties of the material, in particular conductivity. We will simply call them *impurities*. The Kondo effect is a good example in this respect. In metals containing magnetic impurities it leads to an upturn of the conductivity at low temperatures which arises from the antiferromagnetic interaction between a local magnetic moment of a magnetic impurity and the surrounding electron gas. In this chapter we would like to discuss impurities that are detrimental for superconductivity. We will study two types of impurities: a) the Zn which is a non-magnetic impurity (ideally it has full $3d^{10}$ shell) and b) the Ni which is believed to be a magnetic impurity in a cuprate environment. There are strong evidences that the Ni impurity is in a high spin state (see for example Haskel *et al.* [48]). A schematic representation of the high and low spin state of the Ni^{2+} ion together with the spin states of Cu^{2+} and Zn^{2+} is given in Fig. 17 with the simple ionic model. Of course the ionic model is an oversimplified textbook picture. In the next section

---

[17] The necessity of doping for HTSC is not clear. Recently the discovery of a new class of superconducting cuprates with T' structure [132], has questioned the necessity of doping to obtain superconductivity in the cuprates.

[18] It is quite surprising that doping can improve certain properties of a material like conductivity. The dopant actually destroys the translational symmetry of the crystal and the naive Bloch picture is not valid anymore. In general impurities are detrimental for conductivity. It is quite fascinating and still not understood how highly unhomogeneous materials like cuprates can show superconductivity.

we will analyse in more details the spin states of Ni, Zn, and Cu calculated by cluster calculations.

There has been a lot of experimental investigations on impurities substituted cuprates[19]. Why are impurities so important for the study of HTSC? We know that in the pure state a HTSC is already very complicated - so why make it more so and what is the purpose of destroying superconductivity? The idea is that impurities interfere with the mechanism creating the superconductivity, destroying it in the vicinity of the impurity. As we will see below the cluster method permits a detailed calculation of this local behavior. By knowing how the superconductivity is destroyed, the condensed matter physicists hope to better understand the mechanism behind it. This approach is similar to a child taking a toy apart to see how it works.

Now we would like to give some basic theoretical concepts to see how impurities destroy superconductivity in both conventional and unconventional superconductivity and why the study of impurities in superconductors is so important.

5.1 Some elements of theory

5.1.1 Non-magnetic impurities in BCS type superconductors: The Anderson theorem

The starting point for the study of impurities in superconductors are the classical results such as the so called *Anderson theorem* (1959) [12] , and the Abrikosov-Gor'kov theory of pair breaking by magnetic impurities (1960) [2]. The Anderson theorem explains why non-magnetic impurities do not destroy conventional superconductivity. It is a well known experimental fact that the conventional BCS superconductors are almost insensitive to rather large amounts of physical[20] or chemical[21] impurities.

It is important to realize that non-magnetic impurities like Zn let the system invariant under time reversal operations. In a "clean" or pure metal the electronic states are characterized by their wave vector $\vec{k}$ and their Bloch eigenstates $\mid \phi_{\vec{k},s} \rangle$. In a "dirty" metal the (stationary) scattering potential U will lead to a new set of wave functions $\mid \psi_n \rangle$[22]:

$$\hat{H} \mid \phi_{\vec{k},s} \rangle = \xi_{\vec{k}} \mid \phi_{\vec{k},s} \rangle \rightarrow \left(\hat{H} + \hat{U} \right) \mid \psi_n \rangle = \xi_n \mid \psi_n \rangle. \tag{43}$$

---

[19] Note that we will use the word *substitution* to speak about impurities to avoid confusion.

[20] Substances in amorphous states can become superconducting.

[21] Disordered alloy systems with 20-50 percent of chemical scattering centers have a transition temperature comparable with those of pure elements. [80]!

[22] Of course the presence of randomly distributed impurities in the crystal destroys the translational invariance and $\vec{k}$ is no longer a good quantum number. Here n is an appropriate quantum number. We simply assume that we have solved the extremely difficult problem of finding the wave functions of the electrons in the presence of scatterers.

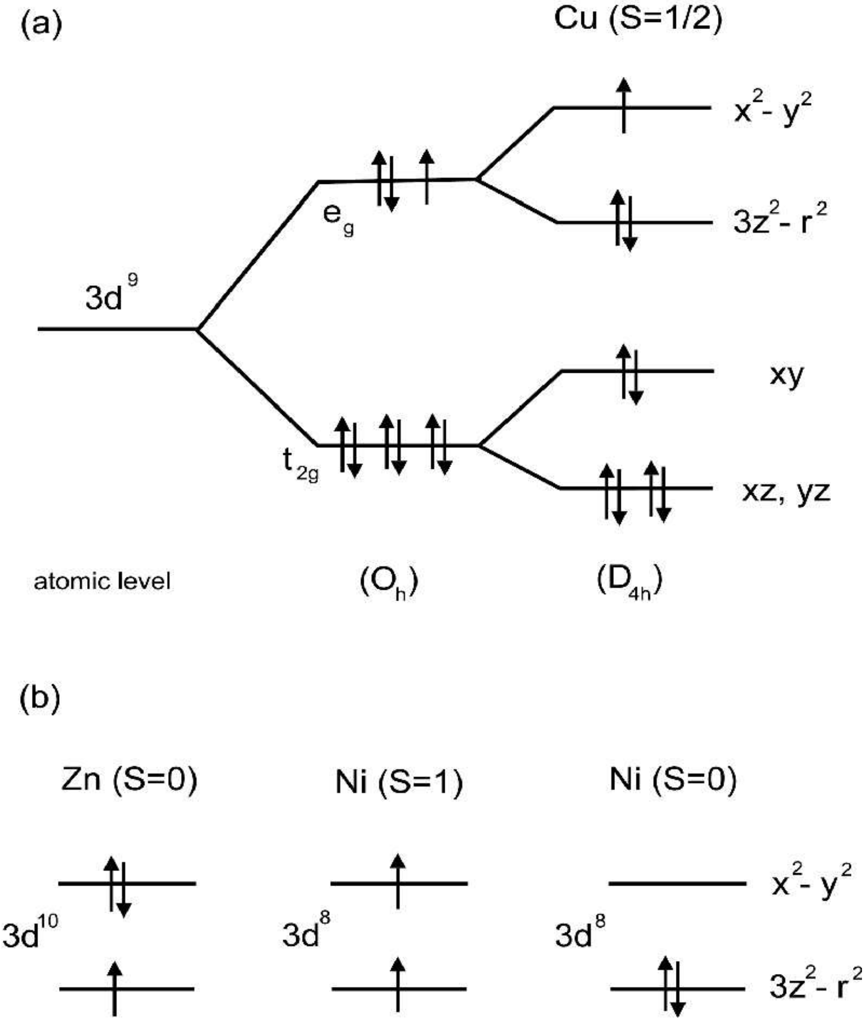

Figure 17: Schematic illustration of the splitting of the 3d energy levels for (a) Cu and (b) Zn and Ni embedded in a cuprate environment in the ideal case. For a Cu atom in spherically symmetric field, the 3d levels are degenerate in energy. In a crystal field of cubic symmetry O_h , for a proper octahedral CuO_6 the five 3d orbitals in a cubic environment are split into a triplet (t_{2g}=xy,yz, and xz) and a doublet (e_g=z^2 and x^2-y^2). They are separated by Δ the crystal field splitting (1-2 eV). Upon the decrease of symmetry to tetragonal D_{4h}, a further splitting of the 3d levels into the states b_{1g}= x^2-y^2, a_{1g}=z^2, b_{2g}=xy and e_g=yz, xz occurs. For the Zn atom has a full $3d^{10}$ shell (s=0). For Ni the high spin state (S=1) and the low spin state (S=0) are represented.

The new states $|\,\psi_n\,\rangle$ form an complete orthonormal set (they are adiabatically related to $|\,\phi_{\vec{k},s}\,\rangle$). One has

$$|\,\psi_{n,s}\,\rangle = \sum_{\vec{k}} |\,\phi_{\vec{k},s}\,\rangle\langle\,\vec{k}\,|\,n\,\rangle \quad \text{and} \quad |\,\psi_{\vec{k},s}\,\rangle = \sum_{n} |\,\psi_{n,s}\,\rangle\langle\,n\,|\,\vec{k}\,\rangle. \tag{44}$$

The degenerate partner electronic states which form the Cooper pairs are related through a time reversal operation:

$$\hat{K}|\,\phi_{\vec{k},s}\,\rangle = -i\sum_{s'}\sigma^y_{ss'}|\,\phi_{-\vec{k},s'}\,\rangle = -i\sum_{n,s'}\sigma^y_{ss'}|\,\psi_{n,s'}\,\rangle\langle\,n\,|\,\vec{k}\,\rangle^* \tag{45}$$

that is for example:

$$\hat{K}|\,\phi_{\vec{k},\uparrow}\,\rangle = |\,\phi_{-\vec{k},\downarrow}\,\rangle. \tag{46}$$

This is also true for the new states $|\,\psi_n\,\rangle$ which are still degenerate because the non-magnetic impurities do not destroy the time reversal symmetry:

$$\hat{K}|\,\psi_{n,s}\,\rangle = -i\sum_{s'}\sigma^y_{ss'}|\,\psi_{n,-s}\,\rangle = -i\sum_{\vec{k},s'}|\,\phi_{-\vec{k},s'}\,\rangle\langle\,\vec{k}\,|\,n\,\rangle^*. \tag{47}$$

The interaction part of the BCS hamiltonian with the new state then reads

$$\hat{H}_{int} = \frac{1}{2}\sum_{n,n'} U_{n,n'} c^\dagger_{n\uparrow} c^\dagger_{n\downarrow} c_{n'\downarrow} c_{n'\uparrow} \tag{48}$$

where $c_{n\uparrow}$ and $c^\dagger_{n\uparrow}$ are the creation and annihilation operators in the new states $|\,\psi_{n,s}\,\rangle$. The interaction matrix element has the following form

$$U_{n,n'} = \sum_{\vec{k},\vec{k}'} V_{\vec{k},\vec{k}'}|\langle n\,|\,\vec{k}\,\rangle|^2|\langle n'\,|\,\vec{k}'\,\rangle|^2 = \sum_{\vec{k},\vec{k}'} V_0 g^*_{\vec{k}} g_{\vec{k}'}|\langle n\,|\,\vec{k}\,\rangle|^2|\langle n'\,|\,\vec{k}'\,\rangle|^2. \tag{49}$$

Normalization requires

$$\sum_{\vec{k}} |\langle\,n\,|\,\vec{k}\,\rangle|^2 = 1 \tag{50}$$

and for an isotropic interaction potential (which leads to slowly varying coefficient $g_{\vec{k}}$)[23] the pairing interaction remains unchanged in the space of the $|\,\psi_n\,\rangle$ and the critical temperature is given by the unchanged BCS equation

---

[23] It is averaged over the entire Fermi surface

$$k_B T_C = 1.13\hbar\omega_D e^{-1/\lambda} \tag{51}$$

with $\lambda = V_0 N_0$. Then a change in T_c is only possible with a change in the density of states at the Fermi energy, N_0. Within the framework of quantum field theory one can show that the effect of non-magnetic impurity scattering can be taken as a simple renormalization of the energy scale *without any influence on thermodynamic properties.* The theorem is only an approximate statement about the thermodynamic averages of the system and is based on the conservation of the time reversal symmetry. If this symmetry is broken then the argument fails.

5.1.2 Magnetic impurities

Magnetic impurities (that is impurities that have a magnetic moment), cause the breakdown of superconductivity with very small concentration [2], because the spin of the electrons couples to the local magnetic moment of the impurity

$$H_{imp} = \sum_i \int d^3r \quad J \cdot \vec{M}_i \cdot \hat{\vec{S}}(\vec{r}) \cdot \delta(\vec{r} - \vec{R}_i) \tag{52}$$

where $\vec{M}_i$ is the magnetic moment of the impurity at the position $\vec{R}_i$ which couples with the coupling constant J to the spin density $\hat{\vec{S}}(\vec{r})$. Evidently the static moment of the impurity breaks the time reversal symmetry and the scattered states $|\phi_{-\vec{k},\downarrow}\rangle$ and $|\phi_{-\vec{k},\uparrow}\rangle$ are no longer degenerate (see for example Ref. [3]). One can show that magnetic impurities lower T_c significantly as:

$$T_c \approx T_{c0} - \frac{\pi\hbar}{4\tau_s k_B} \tag{53}$$

where T_{c0} is the critical temperature of a pure superconductor and τ_s is the mean free time relative to the spin flip associated with the magnetic impurities. The presence of magnetic impurities in a given concentration range can even produce gapless superconductivity [4, 40].

5.1.3 Unconventional superconductivity

In the case of unconventional d-wave pairing the situation is much different (see for example Ref. [113]). Non-magnetic impurities have a strong effect on superconductivity in case of an anisotropic pairing. This can be easily seen by taking a look at Eq. (49). If $g_{\vec{k}}$ is not constant anymore but rather describes anisotropic pairing (in the case of unconventional superconductivity even with $\langle g_{\vec{k}} \rangle_{\vec{k},FS} = 0$) then of course the completeness relation (50) is no longer valid. The effective interaction is lowered. As a consequence of unconventional pairing the non-magnetic impurities strongly modify the density of states[24]. Non-magnetic impurities will then modify the exponents in the power-laws describing the temperature dependence of specific heat, thermal conductivity, NMR relaxation rate and electromagnetic absorption.

Therefore the suppression of superconductivity by non-magnetic impurities is a strong hint of an unconventional pairing state. The strong suppression of the superconducting properties by a small concentration of Zn in cuprates is often claimed to be one of the first indirect proofs of the unconventional pairing state which war found in those materials. Recently with STM experiments in Zn doped BiSCO it has even been possible to see a d-wave pairing signature around the scatterer [94]. To summarize, impurity is an important tools to identify the nature of the pairing state and microscopic properties in cuprates.

5.2 Impurities in HTSC: some experimental facts

In hole doped cuprate superconductors[25], non-magnetic impurities like Zn and others are detrimental [145] and superconductivity disappears with a few percent of Zn dopants. This fact has initiated an enormous activity in experimental and theoretical investigations on the effects of impurities that substitute copper in the CuO_2 planes. In this section we would like to summarize some of the experimental results which have been obtained so far.

Of course there are many possible substitutions for the planar Cu (Fe, Co, Ni, Zn, Ga, Li, Al, Mn, Cr, Ti,...), but we will concentrate mainly on Zn and Ni. These two impurities are the most widely used experimentally to probe superconductivity[26]. We will also essentially concentrate on NMR and NQR properties because some of these properties can be related with results of our cluster calculations.

---

[24] This of course will depend on the pairing state. For example within the framework of generalized BCS theory the density of state of the polar state (with line nodes) is the most strongly modified [113] by non-magnetic impurities.

[25] In electron doped superconductors the situation is still unclear. Although the d-wave symmetry of the hole doped cuprates is generally agreed by the community, the pairing state of the electron doped cuprates is still matter of debate. There are evidence there that magnetic impurities will have a bigger effect than the non-magnetic ones [122, 62].

[26] One reason for this is that Ni and Zn are divalent impurities and are believed to go mainly the to Cu(2) site [145]

5.2.1 Magnetic and transport properties

The influence of impurity substitution on the magnetic and transport properties of cuprates has been studied very early after the discovery of HTSC. In p-type cuprates Zn is more detrimental than Ni destroying superconductivity [145, 144]. More precisely Zn^{2+} ions induce a reduction of T_c by about -12 K/% Zn. This is almost three times larger than for magnetic Ni^{2+} ions [128, 82][27]. This difference between Ni and Zn has been put forward as evidence supporting a magnetic mechanism for HTSC [88, 98]. A typical resistivity plot obtain by Tarascon *et al.* [128] for the La_2CuO_4 substance for different Zn and Ni concentrations is given in Fig. 18.
Xiao *et al.* [144] in a systematic study in impurity doped $La_{1.85}Sr_{0.15}Cu_{1-x}A_xO_4$ (A=Fe, Co, Ni, Zn, Ga, Al) showed that regardless of magnetic or nonmagnetic impurity the macroscopic susceptibility of every system exhibits Curie-Weiss behaviour, indicating the existence of a *localized moment* induced by Zn. Surprisingly, the nonmagnetic dopants that cannot carry moments by their atomic structures induce all a similar moment, i.e., 1.0-1.2 μ_B. It was also shown that Ni and Zn impurities do not appreciably change the overall carrier density [44, 77, 125, 137].

5.2.2 NMR

Nuclear magnetic resonance (NMR) and nuclear quadrupole resonance (NQR) studies were widely used to probe Zn and Ni doped p-type cuprates especially for the Cu atoms. Those have led to conflicting conclusions. The results from NMR and NQR studies have been analysed in terms of (i) a local *suppression* of the antiferromagnetic spin correlations about the Zn impurity [56, 95, 152], (ii) *no local suppression* of the antiferromagnetic spin correlations about the Zn impurity [140, 141], (iii) an enhancement of the antiferromagnetic correlations about the Zn impurity [61, 59] and (iv) a transition from magnetic to quadrupole relaxation for high Zn impurity concentrations [95]. The interpretation of the data is made more difficult by susceptibility, NMR ^{17}O, and the ^{89}Y studies [140, 77], which show that the data can also be analyzed in terms of a Zn induced local moment on the Cu sites nearest neighbor to the Zn site. The magnitude of the Zn-induced local moment, for high Zn impurity concentrations, decreases with increasing hole concentration [82]. More recent NMR experiments in Li doped YBCO by Bobroff*et al.* [30] show that Li also induces moments on the NN Cu and that their values are identical to those induced by a Zn impurity[28]. Using ^7Li NMR the authors argued that the anomalous local moment induced by Li persists below T_c in YBCO. It was also concluded by Mendels *et al.* [81]

---

[27] Some authors still do not agree with this fact for example Williams *et al.* found evidence that T_c is equally depressed by Ni and Zn.

[28] See also a discussion relative to this paper on the preprint server [126, 31].

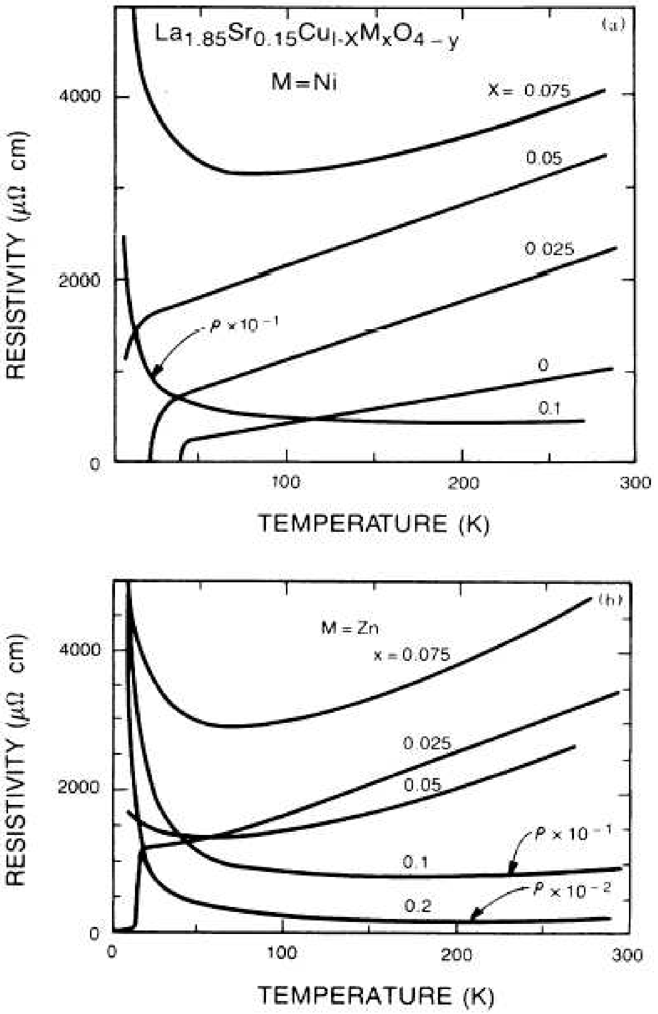

Figure 18: Typical behavior of the resistivity vs temperature for different concentrations of Zn and Ni taken from [128]. (a) Resistivity data for $La_{1.85}Sr_{0.15}Cu_{1-x}Ni_xO_4$ and (b) resistivity data for $La_{1.85}Sr_{0.15}Cu_{1-x}Zn_xO_4$ (x denotes Ni and Zn concentration, respectively).

that above T_c each Ni atom possesses a strong magnetic moment around 1.5 μ_B.
Knight shift measurements for Zn and Ni substituted $YBa_2Cu_3O_7$ have been reported by Ishida *et al.* [56]. In the Zn case, above T_c, K_{ab} is almost independent of both temperature and Zn concentration. The spin shift K_{ab}^{spin} at low temperature increases with increasing Zn content which is considered by the authors to indicate the presence of a finite density of state at the Fermi level induced by Zn. This is even observed in the superconducting state. In the Ni case, K_{ab} above T_c is temperature independent but it increases slightly with Ni doping, indicating the slight enhancement of the spin susceptibility upon Ni substitution. In contrast to the Zn case no change in the Knight shift is observed at low temperature.

5.2.3 Zn induced additional peaks in NMR and NQR

The Zn impurity has a detectable influence on the NMR and NQR properties. In particular the Zn impurity can induce additional peaks in the NMR and NQR spectra[29]. Two such additional peaks were first observed by Mahajan *et al.* [77] in the ^{89}Y NMR spectra of $YBa_2(Cu_{1-y}Zn_y)_3O_{6+x}$. Later Williams *et al.* [140] found similar additional peaks in the ^{89}Y NMR and ^{17}O spectra of $YBa_2(Cu_{0.9825}Zn_{0.0175})_4O_8$. The two additional peaks in the ^{89}Y NMR spectra which have both frequencies slightly lower than the main ^{89}Y peak, were assigned by Mahajan *et al.* and Williams *et al.* to Y sites nearest neighbour (NN) and next nearest neighbour (NNN) to the Zn impurities. The main line was interpreted to originate from all other ^{89}Y sites. The three peaks display different ^{89}Y spin-lattice relaxation times T_1 and different ^{89}Y Knight shifts. Note T_1 is observed to be shorter for the satellite peaks than for the main line ($T_{1,sat} < T_{1,main}$). Mahajan *et al.* attributed the additional peaks in the ^{89}Y NMR spectra of $YBa_2(Cu_{1-y}Zn_y)_3O_{6+x}$ to an induced local moment on the four nearest-neighbour Cu sites to the Zn impurity which influence the Y NN and NNN. This induced localized moment on the nearest neighbour sites gives a Curie-like contribution to the Knight shifts and spin susceptibility. However recent μSR measurements on $YBa_2(Cu_{1-z}Zn_z)_4O_8$ found no evidence of a local moment induced by Zn [23]. The existence of such an induced Zn moment is still a matter of debate and if it exists, its origin is not understood theoretically.
Later Williams *et al.* [139, 141] noticed a similar Zn induced additional line in the Cu NQR spectra of $YBa_2Cu_4O_8$. Actually this peak could have been guessed from earlier NQR studies by Yamagata *et al.* [56] and Ishida *et al.* [147], but the resolution of the experiment was not good enough to conclude the existence of such an additional peak. This peak was then

---

[29] In the literature the terminology for this additional peak is "satellite peak" which can lead to confusion (this can be confounded for example with the two satellite peaks of the ^{63}Cu NMR spectra (see Fig. 3)).

confirmed by Itoh *et al.* [58, 59]. As can be seen in Fig. 19 from Itoh *et al.* [59] the main ^{63}Cu line broadens when Zn is substituted and the additional peak grows with increasing Zn concentration. For each peak a spin-lattice relaxation time has been measured. Itoh *et al.* measured that T_1 of the additional Zn induced peak is shorter than that of the main signal

$$^{63}T_{1,satellite} < {}^{63}T_{1,main}. \tag{54}$$

The T_1 time of the main ^{63}Cu peak is also influenced by Zn and it has been reported that for "high Zn doping" (typically $x \gg 0.03$) ^{63}Cu $T^{Zn}_{1,main}$ is *bigger* than for [59] pure $YBa_2Cu_3O_7$ and $YBa_2Cu_4O_8$

$$^{63}T^{Zn}_{1,main} > {}^{63}T^{pure}_{1,main}. \tag{55}$$

However as pointed out by Williams *et al.* and Itoh *et al.* both the satellite and main ^{63}Cu peaks cannot be modeled by a monoexponential time decay with greater departure observed for the nearest-neighbor site. This can make the analysis of the spin-lattice relaxation time rather complicated (Itoh *et al.* make a complicated analysis with two different relaxation times and Williams *et al.* fitted the data with a modified exponential) . But the above results about T_1 are qualitatively correct.

In the case of La_2CuO_4 it is impossible to observe such a peak because of the very broad ^{63}Cu NQR spectrum. Beside this Zn seems to induce a wipeout effect[30], (a complete dissapearance of the Cu NQR signal) for Zn-substituted, Sr underdoped samples below 40K [148], interpreted by the authors as a Zn-induced charge-spin stripe formation.

In the case of Ni substitution there is no additional lower frequency ^{63}Cu peak [139]. The ^{63}Cu NQR spectra are systematically broadened with increasing Ni content. Williams *et al.* [139] interpret the absence of a peak near the Ni impurity as due to the Ni moment locally wiping out the NQR signal. There are actually two kinds of wipe out effects. The first kind of wipe out effect is happening when the spin relaxation rate of the nearest neighbors to the impurity is so dramatically enhanced that it does not show up in the NMR or NQR spectra. This possibility has to be excluded in case of Ni substitution because it has negligible effects on the $^{63}T_1$ spin-lattice relaxation rate [139]. Another wipe out of the NQR signal occurs when the impurity modifies the electric field gradients at the sites in its vicinity so strongly that it is pushed away from the window in which the spectrum is actually measured.

---

[30] The wipeout effect is a limitation of the experimental apparatus. Here the relaxation rate is so small that it is impossible to observe any signal with the precision of the experiment.

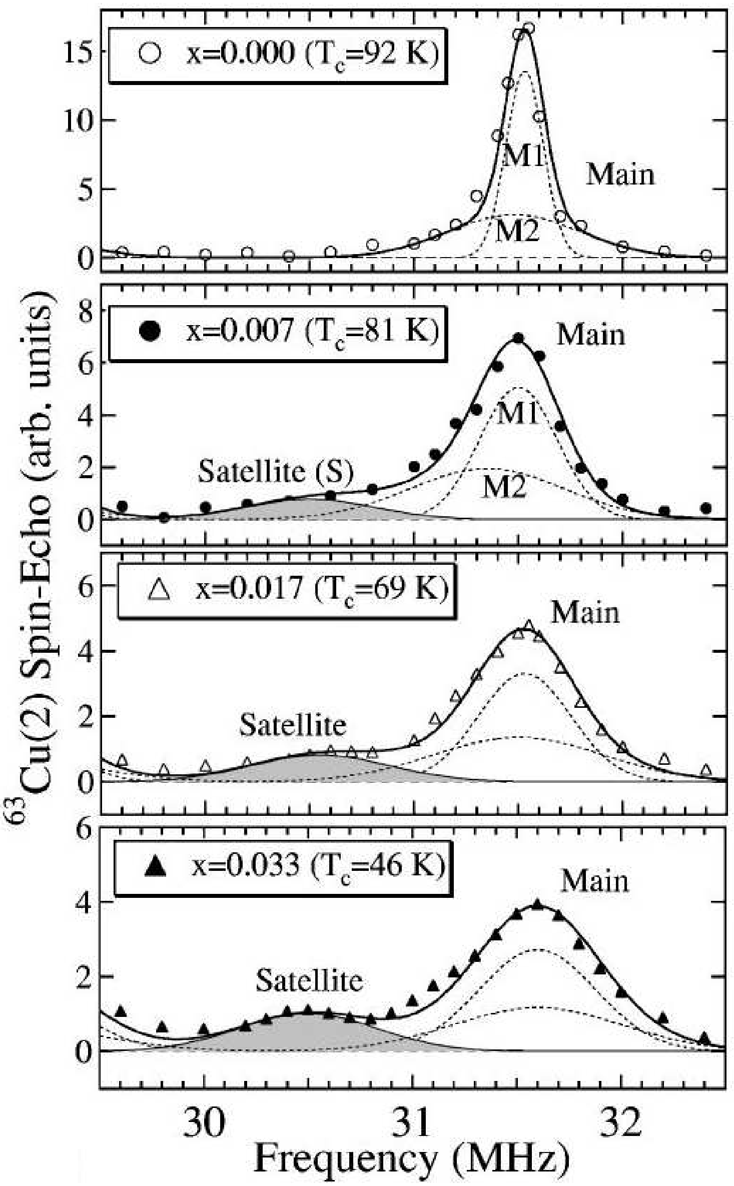

Figure 19: Plot of the normalized NQR spectra from $YBa_2(Cu_{1-x}Zn_x)_3O_{7-\delta}$ with different Zn doping from Itoh *et al.* [59]. The solid curves are multiple Gaussian fits to the data (the authors use in total three Gaussian functions: two for the main peak and one for the satellite peak). The ^{63}Cu satellite peak induced by Zn is marked in gray. The intensity of the satellite peak increase with increasing Zn doping. One also sees clearly the broadening of the main ^{63}Cu peak with increasing Zn doping and that a small shoulder towards higher frequencies is also induced by Zn doping.

5.2.4 STM results

Zn [93] and Ni [51] doped cuprates have also been recently studied with scanning tunneling microscopy (STM) by the group of Davis. These experiments can only be performed in the BSCCO family because those material are the only ones which can be cleaved easily. They can cleave at the Bi-O layer and show a very clean surface which is necessary to perform such experiments. This kind of experiment is very useful to investigate the local properties of the copper oxide planes in the cuprates. However one has to be aware that this method like the ARPES method only investigates the surface of the probes. This fact has been strongly criticized by several authors which believe that one has to "look" inside the bulk to really understand the mechanism of superconductivity. STM experiments provide a map of the differential tunneling conductance which is proportional to the local density of states (LDOS) which provides information about the quasiparticle spectra.

In the Zn doped BSCCO Pan *et al.* [93] found an intense quasiparticle scattering resonance at the Zn sites and this inside the superconducting gap (the so called Shiba states). The superconducting coherence peaks are also strongly suppressed at the Zn scattering site, and recover to their usual value over a distance of about 15 Å from it. The quasiparticle LDOS at the resonance energy does not decay monotonically with distance r from the scatterer but rather oscillates, producing local minima and maxima in the LDOS-map. The local maxima coincide with positions of only some of the atomic sites near the scattering center. The position of the four nearest-neighbor Cu atoms to the Zn have no LDOS local maxima associated with them. This is a rather unexpected phenomenon which is still not fully understood theoretically. On the other hand, the positions of the eight next nearest neighbor and third-nearest neighbor Cu atoms coincide with the local maxima in the DOS image, and appear to form a "box" around the scatterer. The intensity at the next nearest neighbor is greater than the one at the third-nearest neighbor. That is, apart from the Zn site itself, the biggest effect is seen on the NNN to Zn. It is also observed that the LDOS decays faster in the gap-node directions of a d-wave like superconducting gap which is one more evidence for the d-wave symmetry of the order parameter[31].

In the Ni doped BSCCO Hudson *et al.* [51] found a quite different behaviour. At each Ni site they observe two d-wave impurity states of apparently opposite spin polarization, whose existence indicates that Ni retains a mag-

---

[31] In the case of an ideal single potential impurity problem (see Sec.5.3.1) a virtual bound state is created at the impurity which has the form of a cross with long tails in the local density of states. The d-wave gap which is defined in *k space* can be made "visible" in the *direct space* by a non magnetic impurity. Therefore Pan *et al.* [93] speak from the gap-node direction in the direct space. Their observation that the LDOS decays faster in the gap-node directions is only a indirect evidence of a d-wave pairing.

netic moment in the superconducting state (the degeneracy of the single spin impurity state induced by potential scattering is lifted by an additional magnetic interaction between the impurity moment and the quasi-particle spin). The LDOS mapping reveals both particle-like and hole-like components of the impurity states that exist at each Ni. It shows that the impurity state consists of two spatially complementary components. It can also be shown that the superconducting gap magnitude does barely change as one approaches the impurity site. The constant gap magnitude indicates that the superconductivity is not disrupted locally by the magnetic impurity in contrast to the Zn. A detailed analysis of the data leads to the conclusion that the dominant pair-breaking effect is due to *potential scattering* which is surprising since Ni usually is regarded as a source of magnetic scattering. In conclusion STM experiments show marked differences between Ni- and Zn-substituted samples.

5.2.5 Other experiments: neutron scattering and μSR

Here we would like to mention studies made with other experimental techniques. Penetration depth measurements made by Bonn *et al.* [33] with the μSR technique in Zn and Ni doped $YBa_2Cu_3O_{7-\delta}$ reveal a different behaviour for Zn and Ni impurities. It is found that Ni impurities disturb the superconducting pairing state of $YBa_2Cu_3O_{6.95}$ much less than Zn impurities do. The neutron scattering experiments from Sidis *et al.* [112] also show a quite different behaviour between Zn and Ni impurities.

5.3 Theoretical investigations and simulation

In contrast to the large amount of experimental studies of Zn and Ni doped cuprates there has been much less theoretical proposals for the destruction of SC by these impurities. As we mentioned in the introduction there still no consensus on a general theory of HTSC and most of the theorists prefer to search for the general mechanism of HTSC before dealing with much complicated phenomena as impurity scattering without knowing the exact physics of HTSC.

5.3.1 Theoretical investigations

There are mainly three possibilities to face this problem. The first is to use generalized BCS theory assuming a d-wave symmetry for the superconducting gap, the second is to use strong correlation models (as the t-J model), and the third is to perform ab-initio computer simulations. It is not the purpose of this section to go into the details of these theoretical investigations but just to sketch their main results. For more details the reader should check a very nice review on the subject by Balatsky *et al.* [17].

One of the first theoretical studies of the impurity effect in cuprates was made by Borkowski and Hirschfeld [35]. They were the first to propose that systematic impurity doping in the Cu-O plane of the hole doped cuprate superconductors may allow one to decide between unconventional (d-wave) and anisotropic (s-wave) states as possible candidates for the order parameter in these materials. They did their investigation in the framework of generalized BCS theory.

In d-wave systems the density of states below the gap maximum is *non-zero*, and varies linearly with the energy in a impurity free system. Consequently, the overlap with the particle-hole continuum only allows the formation of *virtual bond states* with a finite lifetime inside the superconducting gap. This was first realized by Balatsky *et al.* [16][32] who studied the effect of a single potential impurity problem in a d-wave superconductor. They consider the simplest case of a single scalar impurity i.e. they study the response of the homogeneous d-wave state to a delta-function potential. They use the Yu-Shiba approach, a generalization of the Abrikosov-Gorkov formalism, which treats impurities in the unitary scattering limit and show that a single strongly scattering impurity produces a bound quasiparticle state inside the gap in a d-wave superconductor. They find two terms in the local density of states:

$$N(\mathbf{r},\omega) = N(\omega) + N_{imp}(\mathbf{r},\omega). \tag{56}$$

The first term originates from the bulk quasiparticles and is a constant in the system. The second term originates from the virtual bound state created at the impurity. N_{imp} turn out to have a form of a cross with long tails extended along the gap nodes as can be seen in green in Fig. 20. N_{imp} is of course a quantity defined in the *direct space*. At this point to avoid confusion it is important to realize that in this case we are equating real space and momentum space directions. This because the real space structure of the bound state wavefunction is tied to the crystal axes, and less evidently the Fourier transform of the order parameter is tied to the *same* axes. Therefore according to this simple impurity theory there is a coupling between the direct and the k space!

The STM results for Zn [93] however show a more complicated pattern than this simple cross-like form for the density of states, which is why various people have tried to consider many-body effects and tunneling matrix element "filter" effects [17].

The explicit form of the bound-state wave function is found to decay exponentially with angle-dependent range. The bound-state probability density decays as the inverse second power of the distance from the impurity, mostly localized along the nodes of the gap function

$$N_{imp}(\mathbf{r},\omega = 0) \propto r^{-2}, \tag{57}$$

---

[32] See also the review of Balatsky *et al.* [17] for a detailed description.

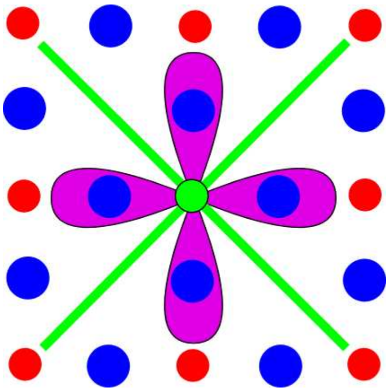

Figure 20: Effect of a single impurity atom (green) in a HTSC (d-wave symmetry) with a simple impurity scattering model. The copper atoms are in red and the oxygen atoms are in blue. The superconducting energy gap in the direct space is in violet and the predicted impurity state is a green cross.

and similarly, but with smaller amplitude, in the vicinity of the extrema of the gap function,

$$N_{imp}(\mathbf{r}, \omega = 0) \propto \frac{\delta_0^2}{E_F^2} r^{-2}, \tag{58}$$

with $\delta = \delta_0 cos 2\phi$ being the gap function of d$_{x^2-y^2}$ symmetry. For the authors the different decay behaviors of Eq. (57) and (58) provide an explanation for the different Cu NMR spin-lattice relaxation rates measured for the main and the the Zn induced satellite peak that we mentioned in Sec. 5.2.3. This satellite is believed by them to arise from the sites close to Zn impurities in the cuprates being sensitive to the higher local density of states.

Some theoretical investigations of impurity effects in cuprates have been performed with the t-J model, the standard (and also the simplest) strong-correlation model, to approach this type of materials. Poilblanc *et al.* [99] performed exact diagonalization of the t-J hamiltonian for small clusters (typically 20 sites). They attribute the large effects of Zn impurities to a disruption of local antiferromagnetic correlations by spin vacancies (this is depicted schematically in the upper panel of Fig. 21), which, depending upon the magnitude of J/t of the host, can lead to a spatially extended bound state. They treat the Zn impurity as an inert site, which eliminates the antiferromagnetic exchange couplings to its nearest neighbor Cu sites and doing so disrupts the local AF correlations. In addition they show that the neighboring copper sites may develop local moments.

In a following publication the same authors investigated the effect of magnetic Ni impurities [100]. With the same model they consider a similar

approximate characterization of the Ni impurity problem except that they allow the impurity to have a spin (which for simplicity they take to be S=1/2) and couple it to its nearest neighbors via an exchange coupling J'. They find bound states only in the case of very weak coupling (J'/J≪1). But even for a modest J'/J coupling (>0.3) no bound states are found. Within their model, they picture the Ni impurities as maintaining the local AF correlations and hence acting as much weaker scattering centers than the Zn impurities which destroy the local Cu spin correlations (this situation is depicted schematically in the lower panel of Fig.21).
Kilian *et al.* [67] treat the t-J hamiltonian in the framework of the resonating valence bond (RVB) mean-field theory. In a similar manner as Poilblanc *et al.*, they attribute the effects of Zn impurities to a disruption or resonating-valence bound (as depicted schematically in the upper panel of Fig. 21 the Cu adjacent to Zn cannot form a RVB state). In this picture the impurity induces a broadly distributed moment that resides on Cu sites in the proximity of the impurity. In this picture one can also treat the case of the S=1 Ni magnetic impurity. In this case the spin of the impurity is partially screened by moments induced on Cu sites. Effectively a local impurity spin 1/2 results. With their model they find a more delocalized behaviour for the Zn impurity. They also attempt to explain some ^{17}O NMR results obtained by the Alloul group (Bobroff *et al.* [29]), in particular the ^{17}O NMR line broadening.
Polikovnikov *et al.* [101] proposed a model with which they were able to fit the STM spectra obtain by the Davis group. With their model can explain the occurrence of a LDOS peak near the Fermi level on the Zn site and on the NNN Cu. Their model uses insights from NMR experiments which show that there is a net S=1/2 moment on the Cu ions near Zn and they introduce the induced spin degree of freedom ad-hoc in their model. That is the appearance of such a moment is not explained. Their hamiltonian is a sum of a simple BCS hamiltonian and a scattering hamiltonian:

$$H = H_{BCS} + H_{imp}. \tag{59}$$

The scattering hamiltonian is the sum of a Kondo interaction term modeling the interaction of the charge carrier spins for localized moments $\vec{S}_i$ which have been assumed to explain the NMR experiments [77] (this magnetic moment is simply added ad-hoc) and an on site potential scattering term. The Zn impurity is at r_0.

$$H_{imp} = H_{Kondo} + H_{potential} = \sum_{r \in \aleph} \vec{S} c_\alpha^+(r) \frac{\vec{\sigma}_{\alpha\beta}}{2} c_\beta(r) + U c_\alpha^+(r_0) c_\alpha(r_0) \tag{60}$$

where $c_\alpha(r)$ annihilates an electron at site r, σ are the Pauli matrices in spin space, and $\aleph$ is a set of sites in the neighborhood of r_0 where the local moments are formed (the sites NN to Zn). They argue that the Kondo spin dynamics of these moments is the origin of the low bias peak in the differential conductance, rather than a resonance in a purely potential scattering model. As pointed out by Bobroff *et al.* [30] this computation is the first realistic attempt to account for the magnetic properties detected by NMR and to give a common understanding of the local magnetism observed by NMR and LDOS observed by STM. However there is still no theoretical explanation for the origin of the Zn induced moments.

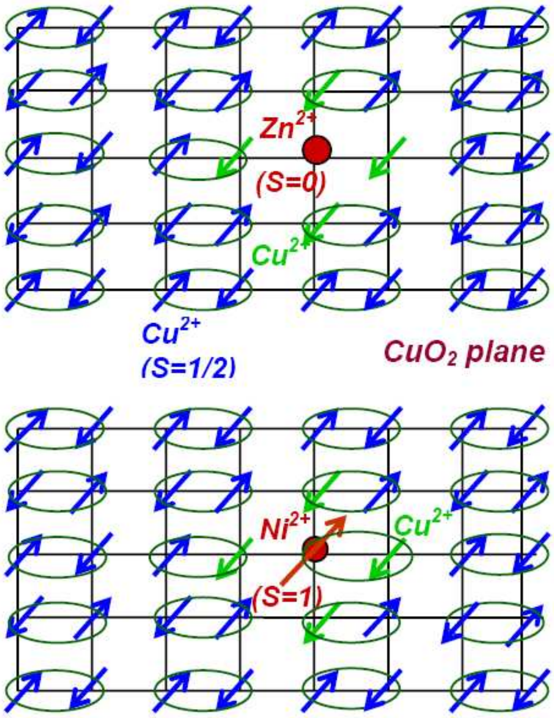

Figure 21: Schematic illustration from Ref. [149] of the effect of quantum impurities on hole doped cuprate superconductors. In the upper panel Zn behaves like a magnetic hole (a spinless site in an environment of strongly exchange-coupled spins) that strongly alters NN exchange correlations and disrupts superconductivity. In the lower panel Ni retains a magnetic moment that barely perturbs the antiferromagnetic exchange correlations that facilitate superconductivity.

Finally Abrikosov [5] with a spin density wave model (SDW) proposed to explain some recent experiments. His model establish that Zn, Ni and Li substitution restore the antiferromagnetic ordering of spins in a certain vicinity around them. He claims that this phenomenon would be difficult to explain in terms of localized magnetic moments but it could be very natural, if the antiferromagnetic order is due to a spin-density wave. The SDW can be destroyed by doping, which is described by the increase of the chemical potential. However the impurity atom tends to *repel* the carriers and it automatically reduces the chemical potential in its vicinity and this lead to the restoration of the SDW. Pictorially in the model of Abrikosov the impurity ion is surrounded by a "bubble" of antiferromagnetic phase[33]. As we will see later in this section this mechanism will be confirmed by our calculations. Abrikosov without giving an exact value argues that the radius of the bubble can be several times larger than the lattice constant.

5.3.2 Simulation

Another possibility to face the problem is to perform numerical calculations. This is the method we are choosing in this work. Few numerical simulations have been performed to investigate the impurity problem in cuprates. One reason is the difficulty encountered by using periodic boundary conditions as an impurity site in the lattice will break them. It is however still possible to perform calculations in the direct space as we will do.

This kind of calculations applied to impurities was first proposed by Gupta and Gupta which investigated Zn doped $YBa_2Cu_3O_{7-\delta}$ [46]. They performed electronic structure calculations by using the tight binding recursion method with clusters of ≈ 13000 atoms. They however only used basis functions for the valence shells (p functions at the oxygens and d at the other sites) and did not take into account the electron correlations which of course play an very important role in the cuprate materials. As pointed out by Stoll *et al.* [119] this is not sufficient to calculate physical quantities such as the electric field gradients. The authors observe the collapse of the antibonding Cu-O band (Zn has a filled 3d shell that lies much lower in energy than the 3d states of Cu). This has two major consequences. First the perturbation due to Zn is not localized to the Zn site alone but extends further. Second there is a strong perturbation of the hole carrier density in the vicinity of the Zn impurity with a significant reduction at the four CuO_2 units neighboring a Zn atom. The biggest effect is seen at the four oxygen sites neighboring Zn which have a large increase in the effective charges of about 0.2 (that is a reduction of the charge carriers). A slight increase in the effective charges at the apical oxygen sites neighboring Zn is also observed. Gupta and Gupta used the same model to investigate the effect of a Ni impurity [47] and compared them to the Zn case. They find that Ni induces a rather localized and weak perturbation compared to Zn. The authors attribute the depression of T_c as resulting from the scattering of the charge carriers with the large moment formed at the Ni site. More recently Kaplan

---

[33] It is well known that the introduction of holes in cuprates tends to destroy antiferromagnetic correlations. As we will see in Sec. 6.3 the effect of the Zn impurity is to expel the holes from its vicinity and to somehow restore an undoped region which favors AF correlations.

et al. [65] used cluster calculations at the MP3 level[34] in the $YBa_2Cu_3O_{7-\delta}$ material. They used clusters with five Cu atoms *neglecting* apex oxygens. The Madelung potentials are simulated with point charges. Note that in the work of Kaplan *et al.* [65] *no* pseudo potentials are used at the border of the cluster. As pointed out in the Sec. 6.1 this gives an abrupt jump in the potential and the potential on the electrons is too strong. Their methodology is open to criticism because in order to obtain a singlet state they make the average between the results of two calculations with two different numbers of electrons. It is found that Zn doping causes stronger and more extended changes of neighbor atom charges and of their bonding than the Ni doping. Their calculation also reveals that the antibonding state Cu(3d)-O(p) almost vanishes at the sites of impurity substitution and that the bonds Zn-O and Ni-O are more ionic than the corresponding Cu-O bond. An estimation of the changes of hole concentration caused by the impurity doping is also made and the authors conclude that all the nearest CuO_2 units around the impurity lose their holes, completely in the Zn case and partly in the Ni case. In the next section we will compare the results obtained by Gupta and Gupta and Kaplan to ours.

---

[34] Møller-Plesset perturbation theory of the third order

6 Effects of Zn and Ni impurities in cuprates studied by cluster calculation

Part of this section has been published in Ref. [25]. In contrast to the vast amount of theoretical investigations on the change in all possible *collective* phenomena that may occur upon Zn substitution, only few informations are available about the changes in the *local* electronic structure. Large supercells would have to be used in traditional band structure calculations to cope with the problems of broken lattice periodicity. Since already in the unsubstituted materials, the unit cells contain a large number of atoms, such supercell calculations are prohibitively complex.

In this section, the electronic structure around both Zn and Ni atoms substituting a Cu is studied by ab-initio cluster calculations. These methods which are not based on periodic lattice structures, are particularly suited to calculate the changes in the charge and spin density distributions that are occurring upon the replacement of a regular atom by a new species.

Here we present results obtained on large clusters comprising 5, 9, and 13 copper atoms in the CuO_2 plane. *Spin-polarized* calculations are carried out and their accuracy is tested by comparing theoretical values for electric field gradients (EFGs) with those derived from experiments [59, 141]. The use of both large clusters and spin-polarized calculations are crucial for the comparison to experiments. More attention will be given to the Zn impurity because in the case of Ni much less experimental data are available and therefore no direct comparison with experiments is possible.

In Sec. 6.1 some computational details will be shortly described. In Secs. 6.2 and 6.3 the resulting changes in the spin and charge density distribution induced by Zn are given. In addition, in Sec. 6.3 simulations of doping with charge carriers are performed and the changes in the charge distribution are compared to the changes induced by Zn and Ni substitution. These differences are then discussed in terms of a phenomenological model related to properties expected from the generic phase diagram. Sec. 6.4 is devoted to the calculation of EFGs at Cu sites near Zn impurities and their comparison to experiments.

6.1 The cluster method and computational details

Since we want to investigate the changes introduced by substituting a copper ion by a zinc ion we first examined the influence of lattice relaxation as the sizes of the two dications are known to be different. Therefore, we have optimized in the Cu_5O_{26}/Cu_8La_{34} cluster for La_2CuO_4 the positions of the four oxygens adjacent to the central copper atom. We then repeated the same optimization procedure in a cluster where we replaced the central Cu by a Zn atom. The result is a small increase of the Zn-O distance by 0.007 Å (respectively 0.004 Å for the Ni-O distance) corresponding to a tiny

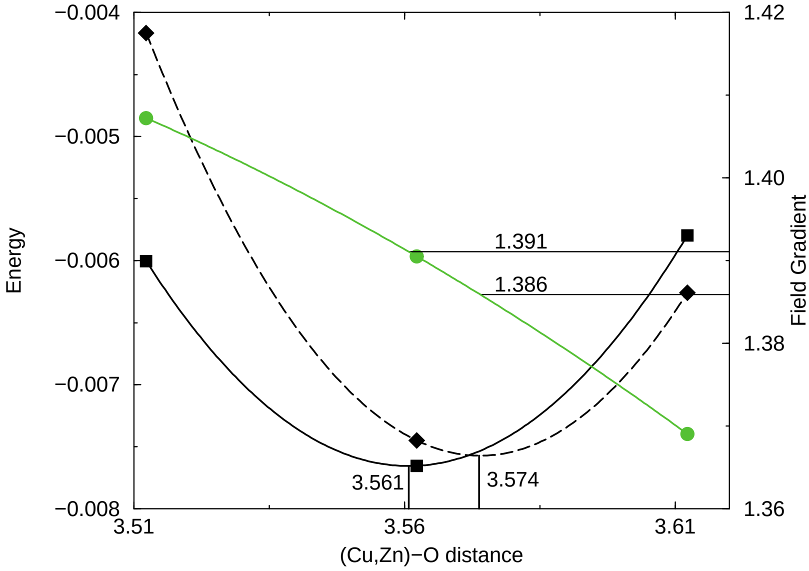

Figure 22: Total energy in hartree of the Cu_5 (black full curve) and $ZnCu_4$ (dashed black curve) clusters for several (planar) oxygen positions (the Zn is placed at the central postion in the cluster). The electric field gradient V_{zz} (in a.u.) at the Cu is also presented for the doped cluster (green full curve).

reduction of the EFG at the Cu adjacent to Zn of less than 0.5 %. This is represented in Fig. 22. We therefore neglect in the following possible lattice distortions[35].

6.2 Spin density distribution

6.2.1 Zn

We have performed extensive spin-polarized calculations using all possible spin multiplicities. The general result of these quantum chemical cluster calculations is that they well reproduce the antiferromagnetic exchange interaction J between NN copper ions with $|J|$ in the range of 160 meV.
Here we illustrate the antiferromagnetic spin arrangement with the Cu_{13}-$O_{62}/Cu_{12}La_{74}$ cluster for La_2CuO_4. With 13 copper atoms we have the possibility of choosing a spin multiplicity with an even value ranging from 2

---

[35] It is believed that Ni an Zn are non-Jahn-Teller ions. In the case of La_2CuO_4 substituted Ni a contraction of the Ni-O(2) apical distance of 0.16 Å and an elongation of Ni-O(1) planar distance of less than 0.01 Å has been measured by Haskel *et al.* [48]. We also performed the calculation with this modified crystal structure around the Ni impurity but the results do not change the overall discussion in this section. For convenience reason we will not present them.

to 14. We performed all the corresponding calculations and the state with lowest energy is obtained by choosing a spin multiplicity of $M = 6$. In Fig. 23a the spin density along the Cu-O bonds in the plane is displayed for an unsubstituted Cu_{13} cluster. In the right panel (Fig. 23b) the signs of the Mulliken spin densities at the planar Cu sites are shown which exhibit an antiferromagnetic spin arrangement, with adjacent copper sites having opposite spins[36].

Most of the spin density is provided by the singly occupied molecular orbital which is also highest in energy. It is a linear combination of $3\mathrm{d}_{x^2-y^2}$ atomic orbitals (AOs) on the coppers ($n(3\mathrm{d}_{x^2-y^2}) = 79\%$) and $2\mathrm{p}_\sigma$ AOs on the oxygens ($n(2\mathrm{p}_\sigma) = 21\%$). The square of the $3\mathrm{d}_{x^2-y^2}$ AO has maxima at distances of 0.345 Å from the nucleus but vanishes at the nucleus. In general, the spin density at a nuclear site is due to s AOs giving rise to the Fermi contact term. In particular, the spin densities at the Cu nuclei (cusps in Fig. 23a) can be correlated with the Mulliken spin densities (whose signs are given in Fig. 23b) at the same and the nearest neighbored Cu nuclei. This observation can be used to split the Fermi contact term into on-site and transferred terms as has been discussed in detail in Refs. [53, 106]. We just note here that the on-site term is negative if the Mulliken spin density at the Cu atom under consideration is positive and vice versa and that the transferred term is positive (negative) if the Mulliken spin densities at the neighboring Cu atoms is positive (negative). Near the oxygens, the spin density is provided by the $2\mathrm{p}_\sigma$ AO and the contact density is very small for antiferromagnetically arranged copper neighbors.

The substitution of Zn at the cluster center introduces an extra electron into the cluster and it is to be noted that the spin state of lowest energy is now the $M = 5$ state. The corresponding spin density along the Cu-O bonds (see Fig. 23c) shows that the antiferromagnetic arrangement virtually remains intact. As expected the Mulliken spin density on the Zn is very close to zero (Fig. 23d). Note that now the contact densities at the copper nuclei adjacent to Zn are reduced in comparison to the same sites in Fig. 23a because there are transferred hyperfine fields from three ions only instead of four. These changes in the hyperfine fields will be further discussed in Sec. 6.4.4.

6.2.2 Ni

For the Ni impurity the situation is somewhat more delicate to treat because of the different possible spin states. This makes this impurity more complicated to handle than the Zn impurity. One of the first question to address is whether the Ni^{2+} is in a high spin state (S=1) or a low spin state (S=0). In the cartoon view of Fig. 17, where the high spin state is represented in an ideal case, the upper d levels, $\mathrm{d}_{3z^2-r^2}$ and $\mathrm{d}_{x^2-y^2}$ have one electron each

---

[36] Note that the up spins are a little bit bigger than the down spins. This is due to the spin contamination of our calculation.

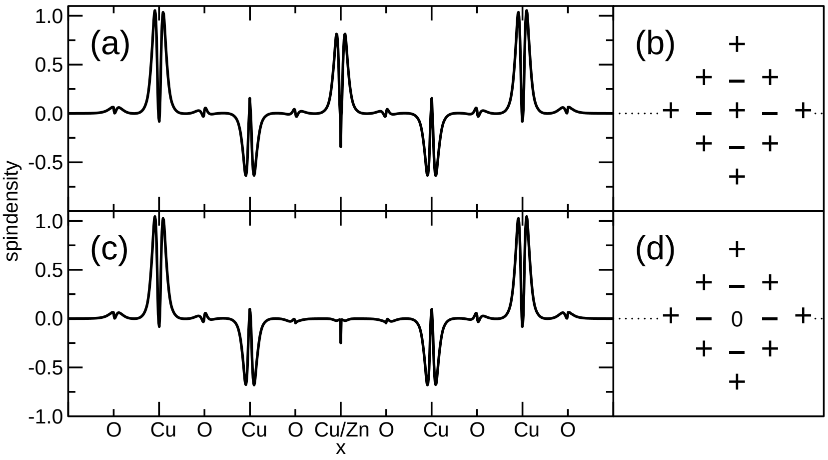

Figure 23: (a) Spin density along the 5 Cu and 6 O in the $Cu_{13}O_{62}/Cu_{12}La_{74}$ Cu cluster of spin multiplicity M=6; (b) and (d) signs of the Mulliken spin densities of the 13 copper ions; (c) spin density with Zn substitution and multiplicity M=5.

Fig. 17. The low spin state has a filled $d_{3z^2-r^2}$ level. Like in the Zn case we performed the calculations for all possible spin multiplicities and for the Cu_{13} cluster we found the calculation with the multiplicity M=7 to be the lowest in energy. These spin states are found to be independent of the cluster size. This situation is represented in Fig. 24 and one clearly sees a large spin component on the Ni site. We also note that in the calculations with all others multiplicities, Ni always carries a spin. We will discuss the spin state of Ni in more details by analysing the spin population of the different orbitals (see Sec. 6.3.5). We thus conclude that the Ni ions in a cuprate environment carry a spin. This is in accordance to experiments [48, 51]. This is of importance because in the case of Ni the antiferromagnetic arrangement is again left virtually intact and in contrast to Zn it is not disrupted at the Ni site. Ni carrying a magnetic moment barely perturbs the antiferromagnetic exchange with its neighbors. As we described in the last section this fact has been used as an explanation for the weaker disruption of superconductivity induced by Ni.

6.3 Charge density distribution

6.3.1 Zn

The cluster method enables a detailed analysis of the local charge distributions and their changes upon Zn substitution and hole doping. We first present the differences observed between the $Cu_{12}ZnO_{62}/Cu_{12}La_{74}$ and the $Cu_{13}O_{62}/Cu_{12}La_{74}$ clusters for La_2CuO_4. The most prominent modifica-

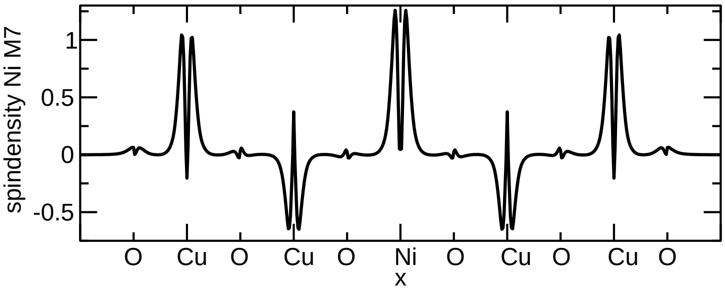

Figure 24: Spin density along the 5 Cu and 6 O in the $Cu_{12}NiO_{62}/Cu_{12}La_{66}$ cluster of spin multiplicity M=7.

tions concern the oxygen atoms adjacent to Zn. We therefore concentrate on the Mulliken charges of these oxygens and their differences in undoped and hole doped La_2CuO_4 and in optimally doped and underdoped $YBa_2Cu_3O_7$. These quantitative results are then discussed in terms of a qualitative model of extended charges. Finally we discuss the implications of our results for models which relate the suppression of T_c upon Zn substitution with enhanced antiferromagnetism around Zn substituted regions.

Let us first discuss the differences in the charge distributions at all atoms. Fig. 25 illustrates the difference in the total electron densities in the CuO_2 plane between the Zn substituted and the unsubstituted La_2CuO_4 using calculations on the corresponding Cu_{13} clusters (with the central Cu atom being substituted by Zn). The framed area insinuates the core region of the Cu_{13} cluster. The solid (black) contours are positive electron density differences, which are more prominent than the dashed (red) contours of negative electron density differences since the central Zn atom has one electron more than the Cu atom it replaces. The white space in the corners of the framed area is significant since the four coppers and 24 oxygens in this region are virtually unaffected by the zinc substitution and do not show up on the contour map ($|\Delta\rho| < 0.005$ a_B^{-3}). The difference between the center atoms can be explained as follows. As expected the $3d_{x^2-y^2}$ AO of the Zn is almost fully occupied (see Sec. 6.3.5), which shows up in the pronounced black density difference in the center of Fig. 25. The red contour lines are concentrated on $3d_{xy}$ orbitals. This is due to the fact that the $3d_{xy}$-electrons of the Zn ion are closer to the nucleus than the ones of the Cu ions since for Zn $\langle 1/r^3 \rangle = 9.39$ a_B^{-3} but $\langle 1/r^3 \rangle = 7.94$ a_B^{-3} for Cu. Therefore, the electron densities at the border of the Zn ion are smaller than at the border of the Cu ion which results in red equidensity lines.

The central zinc atom of course shows the very large positive electron density difference but some has been transferred to the adjacent oxygen atoms and also to one side of the nearest neighbor copper atoms. Thus there are significantly more electrons in the $2p_\sigma$ AO of the oxygens adjacent to Zn than in the unsubstituted case. The occupancy of the $2p_\sigma$ orbital changes from 1.67 to 1.74 and the corresponding Mulliken charges are reduced from -1.63 to -1.71. For the NN copper atoms we observe an asymmetric charge distribution. The total charge on these Cu, however, almost equals that in the unsubstituted compound. On the four coppers which are next nearest neighbors to the Zn, there are more electrons in the $3d_{x^2-y^2}$ AO compared to the bulk values. These charge differences on the NN and NNN copper atoms imply changes in the electric field gradients which will be discussed in detail in Sec. 6.4.1.

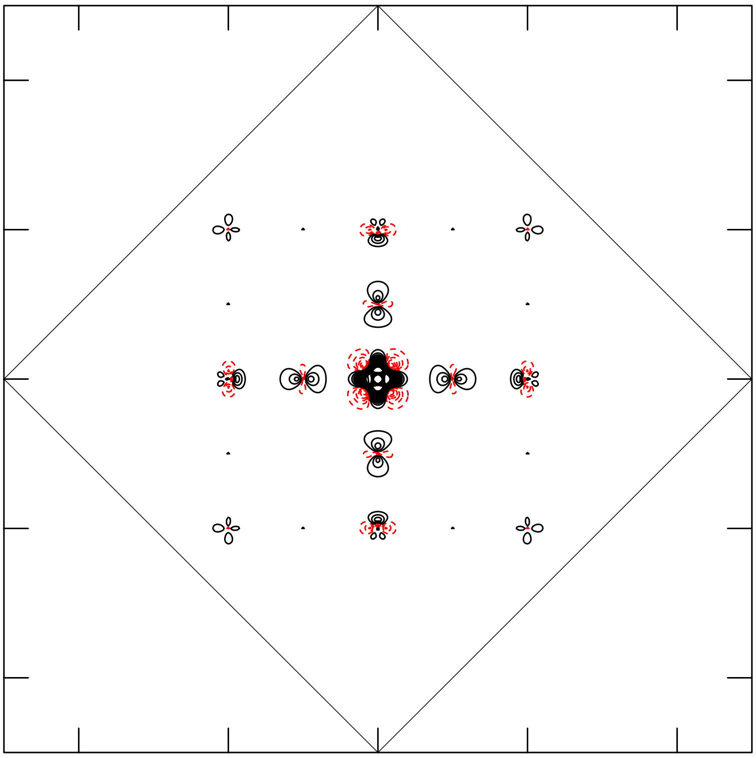

Figure 25: Electron density difference contour plots in the cuprate plane between the $Cu_{12}ZnO_{62}/Cu_{12}La_{74}$ and the $Cu_{13}O_{62}/Cu_{12}La_{74}$ clusters on a area of 5×5 lattice constants. The tick marks correspond to the planar copper position. The solid density lines (black) occur when the local electron density of the Zn substituted cluster is larger than that of the corresponding density of the unsubstituted Cu_{13} cluster. Dashed lines (red), on the other hand, denote that the local electron density is larger in the unsubstituted cluster. Two neighboring lines (solid and dashed) are separated by an electron density difference of 0.01 e/a_B^3.

It is remarkable that the effects of Zn substitution are rather local as concerns the electronic structure. This local screening, however, tells nothing about collective phenomena like scattering where it can produce a much more extended range of influence.

We have also determined the electron density differences for clusters representing the $YBa_2Cu_3O_7$ and $YBa_2Cu_4O_8$ materials. The results are very similar to those for La_2CuO_4 shown in Fig. 25 and discussed above. Furthermore, to simulate the effect of hole doping in La_2CuO_4 we have repeated all calculations for the corresponding clusters $Cu_{13}O_{62}/Cu_{12}La_{74}$ and $Cu_{12}ZnO_{62}/Cu_{12}La_{74}$ with one electron less. These simulations correspond to a hole doping of roughly 8 %. The difference in the charge density between the Zn substituted hole doped and the unsubstituted holed doped Cu_{13} clusters is presented in Fig. 26. The influence of the Zn impurity is now more extended especially for the Cu atoms (note that they are made of positive and negative contributions which cancel each other). Again the biggest change happens on the oxygens adjacent to Zn.

In the same way, the effects of underdoping $YBa_2Cu_3O_7$ were studied by repeating all calculations with one electron more. To discuss the essential changes we concentrate on the Mulliken charges of the four oxygen atoms adjacent to Zn or, in the unsubstituted compounds, Cu.

The calculated Mulliken charges of the planar oxygens in La_2CuO_4 and $YBa_2Cu_3O_7$ are -1.64 and -1.57, respectively, as illustrated by the full black bars in Fig. 27. Both these values are reduced to -1.71 and -1.64, respectively (full red bars), for oxygens adjacent to substituted Zn atoms. The simulation of hole doping in La_2CuO_4 results in a Mulliken charge of -1.61 without Zn (dashed black bars) and -1.70 (dashed red bars) on the oxygens adjacent to Zn. An analogous simulation but with electron doping was performed for $YBa_2Cu_3O_7$. If an electron is added to the $Cu_{13}O_{49}/Cu_{38}Y_{24}Ba_{24}$ cluster the Mulliken charges on the oxygens reduces slightly to -1.58 in the cluster without Zn and is virtually unaffected (-1.64) in the Zn substituted cluster.

6.3.2 Phenomenological model

These quantitative results for the *local* changes near substituted Zn and for the effects of simulating about 8 % hole doping are now put in perspective with the *extended* changes expected from the generic phase diagram. The following discussion is therefore necessarily qualitative and completely phenomenological since we do not consider band structure. It serves, however, to rationalize the main changes that are locally produced by Zn substitution.

The conventional wisdom in cuprate superconductors is that the pure parent compounds La_2CuO_4 and $YBa_2Cu_3O_6$ are insulators and that upon “hole doping” the missing electrons come from the planar oxygens. The holes thus introduced on the oxygens destroy rapidly the long range antiferromagnetic order and the materials become conducting. Although it has been pointed out elsewhere [120, 121] that this picture is too naive and may easily lead to wrong conclusions, a semiquantitative discussion on the values of the oxygen charges and their changes with hole and electron doping both in the unsubstituted and in the Zn substituted compound is instructive. We have therefore indicated in Fig. 27 a schematic separation into a metallic region (gray) and an insulating region (white) with a border line at the arbitrary chosen value of -1.62. For completeness we have also draw in Fig. 26 an electron density difference plot for the hole doped case.

This puts the Mulliken charge on the oxygen in undoped La_2CuO_4 (full black bar in Fig. 27) into the insulating region and that obtained with hole doping in the more metallic region. From simulations of underdoped $YBa_2Cu_3O_7$, however, we find a small decrease of the Mulliken charge which still is the conducting zone.

In each of the four cases considered, Zn substitution drives the Mulliken charges at the oxygens deeper into the insulating region. In particular, Zn substitution in $YBa_2Cu_3O_7$ reduces $\rho_{mull}(O)$ to a value (full red bars) which is almost equal to $\rho_{mull}(O)$ in undoped and Zn free La_2CuO_4 (full black bar). Hence, we observe that the electronic structure in the immediate vicinity of a Zn impurity in hole doped cuprates is similar to that found in the Zn free and undoped parent compounds.

This schematic description of the effect of Zn substitution and charge carrier doping can be interpreted in terms of the generic phase diagram: Zn substitution overcompensates the hole doping effects in its vicinity and thereby creates an environment where the antiferromagnetic correlations are restored. The prediction, however, whether this leads to a static or dynamic spin ordering cannot be given with our cluster method.

Several experiments in Zn substituted cuprates have also been interpreted as indications for locally enhanced antiferromagnetic correlations (see Ref. [61, 59]) induced by Zn. This has been emphasized in the work of Abrikosov [5] who considered the existence of antiferromagnetic bubbles which surround Zn, Ni, or Li impurities in the CuO_2 plane on the basis of the general theory of metal-insulator transition in layered cuprates.

6.3.3 Ni

The same analysis has been performed for the Ni impurity. The difference in the charge density distribution in the Cu(Ni) oxygen plane between the Ni substituted and the unsubstituted La_2CuO_4 Cu_{13} clusters is presented in Fig. 28. Ni is again substituted at the central position. The Ni has one electrons *less* than the Cu. The effect of the Ni is much weaker than Zn and most of the charge difference is concentrated at the central atom. The difference between the center atoms mainly comes from a different occupation of the $3d_{3z^2-r^2}$ AO (with a smaller contribution of $3d_{x^2-y^2}$ AO, see Sec. 6.3.5)

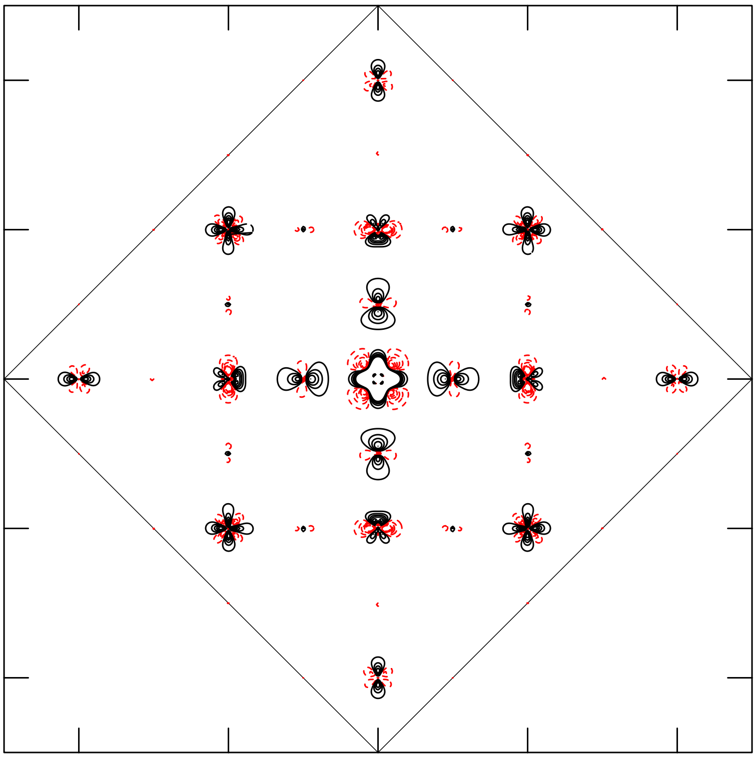

Figure 26: Electron density difference contour plots in the cuprate plane between the $Cu_{12}ZnO_{62}/Cu_{12}La_{74}$ and the $Cu_{13}O_{62}/Cu_{12}La_{74}$ clusters both doped with one hole (an electron has been removed from both clusters) i.e. the function $\rho_{with\ Zn}(r) - \rho_{pure}(r)$ is plotted. The symbols and the units are the same as in Fig. 25.

which shows up in the ring-like red density difference in the center of Fig. 28. Like in the Zn case the four black spots contour lines come from the $3d_{xy}$ orbitals. This is due to the fact that the $3d_{xy}$-electrons of the Ni ion are farther away from the nuclei than the ones of the Cu ions since for Zn $\langle 1/r^3 \rangle$ = 6.73 a_B^{-3} but $\langle 1/r^3 \rangle$ = 7.94 a_B^{-3} for Cu. Surprisingly the *negative* electron density difference is concentrated at the center (see Table (6.3.4)) and the influence of Ni is to produce small *positive* electron density difference on the O NN and the Cu NN and NNN to the Ni. The occupancy of the $2p_\sigma$ orbital for the oxygens adjacent to Ni is 1.69 which is close to the unsubstituted case.

The Mulliken charges at the oxygens adjacent to Ni are plotted in blue in Fig 27. They are respectively -1.65 and -1.59 for the undoped La_2CuO_4 and $YBa_2Cu_3O_7$. For hole (respectively electron) doped La_2CuO_4 (respectively $YBa_2Cu_3O_7$) they are -1.63 and -1.59. We can further apply our phenomenological discussion to the Ni impurity. The result is that Ni repels

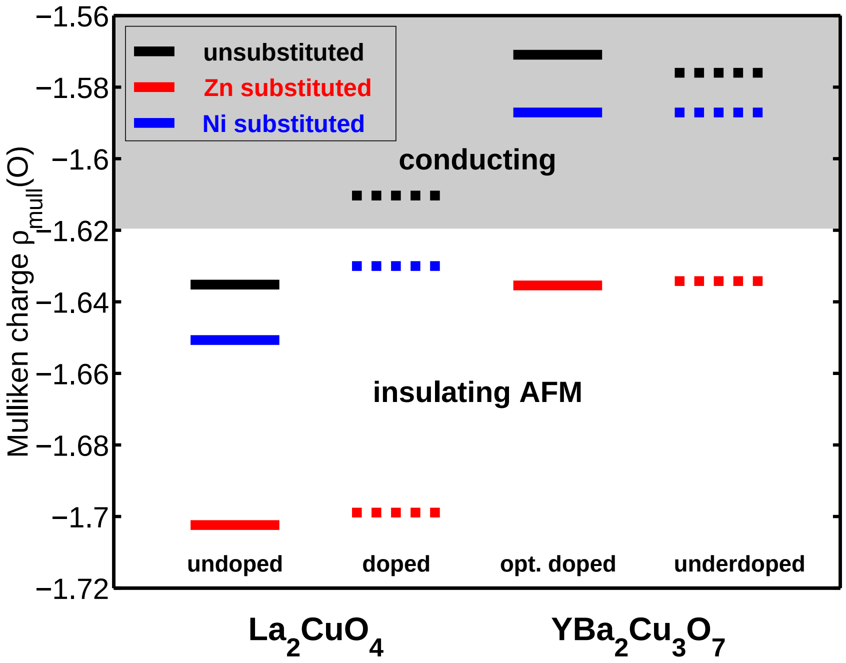

Figure 27: Schematic view of the Mulliken charge on the oxygens in the unsubstituted compounds (full black bars) and in Zn substituted compounds adjacent to a Zn atom (full red bars) or a Ni atom (full blue bars) for La_2CuO_4 and $YBa_2Cu_3O_7$. The results for clusters doped with one hole for La_2CuO_4 and one electron for $YBa_2Cu_3O_7$ are plotted with black (in unsubstituted clusters), red (in Zn substituted clusters) and blue (in Ni substituted clusters) *dashed* bars. An approximate border line at -1.62 is drawn to illustrate the separation between the insulating antiferromagnetic phase and the conducting phase.

holes from its vicinity much less than Zn does. For La_2CuO_4 for both doped and undoped cases the Ni drives the Mulliken charges at the oxygens into the insulating region but much less than Zn does. Furthermore according to our model the reduction of the Mulliken charge in $YBa_2Cu_3O_7$ is not sufficient to drive the oxygens into the insulating region and will be much less disruptive than Ni. Ni in contrast with Zn will then act more like a simple potential impurity scatterer by destroying superconductivity[37]. This explains why Ni destroys superconductivity less than Zn does with the same amount of impurities [145, 144, 127][38].

---

[37] As we pointed out in Sec. 5 STM experiments have shown that despite their magnetic moments, scattering at Ni atoms is dominated by potential interactions.

[38] Of course Zn will also be a potential scatterer

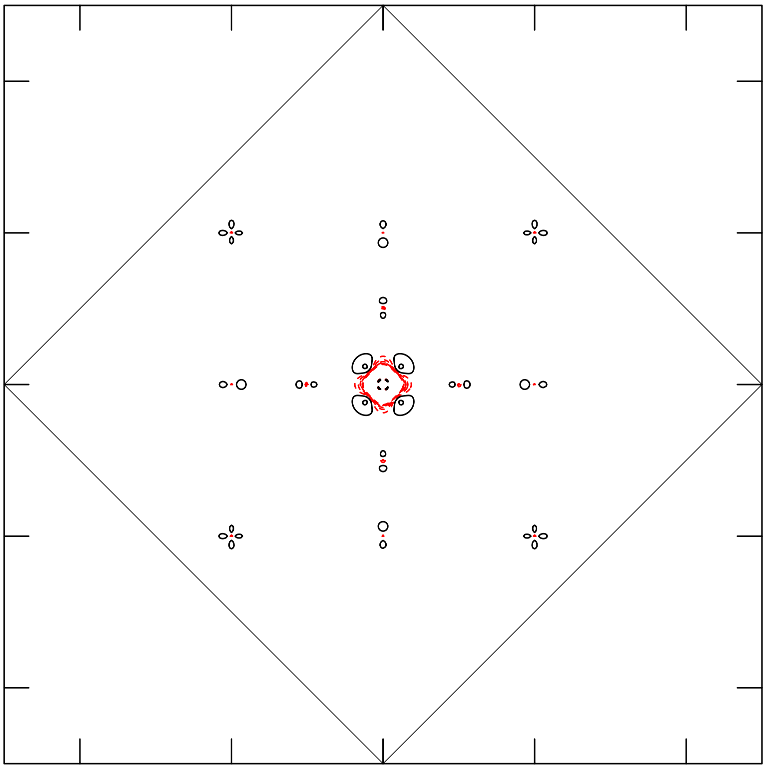

Figure 28: Electron density difference contour plots in the Cu(Ni) oxygen plane between the $Cu_{12}NiO_{62}/Cu_{12}La_{66}$ (multiplicity M=7, high spin state) and the $Cu_{13}O_{62}/Cu_{12}La_{66}$ (multiplicity M=6), i.e. the function $\rho_{with\,Ni}(r) - \rho_{pure}(r)$ is plotted. The symbols and the units are the same as in Fig. 25.

6.3.4 Detailed Mulliken charge differences: Comparison with other works

For completeness we give the detailed Mulliken charge differences for the different sites in the Cu_{13} cluster for La_2CuO_4 in Table 6.3.4 and for $YBa_2Cu_3O_7$ in Table 6.3.4. The comparison of the data of Table 6.3.4 with the calculations of Gupta and Gupta [46, 47] Kaplan *et al.* [65], show large discrepancies. Our results show a more localized behaviour. In our calculations the main changes are observed at the oxygens adjacent to Zn. The discrepancies with Gupta-Gupta are easily understandable because of the approximate nature of their method. As pointed out in Sec. 5 they only simulated the external O p and Cu d shells, and did not took into account correlation effects (the tight-binding model being based on the one-electron approximation). The differences with the calculation of Kaplan *et al.* can been explained as follow. First of all they use a different method (Møller-Plesset perturbation theory). Second they use a calculation which is spin unpolarized. They take the average between the results of two calculations which have different numbers of electrons to avoid problems with spin contamination. Third they do not use pseudopotential at the edge of the cluster (no screening region). If we discard the screening region in our calculations we observe large edge effects [104]. If one takes a look at Table 2 in [65], it can be seen that Kaplan *et al.* obtain a greater charge difference on the oxygen NNN (-0.19 in average) than the NN (-0.04) to Zn. This is certainly due to such an edge effect because the NNN are at the edge of the cluster. Fourth they only used a Cu_5 cluster without apical oxygens. Fifth Gupta-Gupta and Kaplan *et al.* did not mentioned the basis set they used for their calculations. The results of the calculations and particularly the evaluation of the Mulliken charges can depend on the choice of the basis set. To finalize this discussion it should be emphasized that both calculations from Gupta-Gupta and Kaplan have not been compared to experiments and thus remain pure speculations. This is not the case for the calculations that we performed which we will be able to compare with NQR experiments in Sec. 6.4. However the general trend of the calculations of Gupta-Gupta and Kaplan showing a stronger modification of the electronic around the Zn impurity than the Ni impurity agrees with our calculations.

Site	Ni	Zn
NN O	-0.016	-0.067
NNN O	-0.002	0.002
NNNN O	-0.001	0.004
NN Cu	-0.005	-0.001
NNN Cu	-0.002	-0.004
NNNN Cu	0	0
Central atom	1.066	-0.687
apex O (center)	0.048	0.001

Table 9: Mulliken charge differences for La_2CuO_4 at different sites in the Cu_{13} cluster ($\Delta\rho_{Mull}$=ρ(substituted cluster)-ρ(pure crystal)) induced by Zn and Ni subsitutions at central positions.

6.3.5 Partial Mulliken charge analysis

We now analyse the partial Mulliken charge and partial Mulliken spin of selected AO for Cu, Ni and Zn. The results are given in Table 6.3.5. As discussed elsewhere [53] the highest occupied molecular orbital (HOMO) in the unsubstituted La_2CuO_4 substance is a combination of the Cu $3d_{x^2-y^2}$ and the Op_σ AO. In this case the $3d_{3z^2-r^2}$ is nearly fully occupied and the $3d_{x^2-y^2}$ is more than half occupied. This picture breaks down near a Zn or

	Ni		Zn	
Site	a-axis	b-axis	a-axis	b-axis
NN O	-0.0156	-0.0168	-0.0633	-0.0657
NNN O	-0.0024	-0.0024	-0.0008	0.0008
NNNN O	0.0003	0.0009	0.0032	0.0041
NN Cu	-0.0051	-0.0054	-0.018	-0.008
NNN Cu	-0.0034	-0.0034	-0.0076	-0.0076
NNNN Cu	-0.0009	-0.0013	-0.0006	-0.0003
Central atom	1.1012		-0.7041	
apex O (center)	0.0585		0.004	

Table 10: Mulliken charge differences for $YBa_2Cu_3O_7$ at different sites in the Cu_{13}cluster ($\Delta\rho_{Mull}$=ρ(substituted cluster)-ρ(pure crystal) induced by Zn and Ni substitutions at central positions.

a Ni impurity where the combination of the Cu $3d_{x^2-y^2}$ and the Op_σ AO is lowered in energy. The Zn and the Ni are very near from the ideal picture of Fig. 17. Both $3d_{3z^2-r^2}$ and $3d_{x^2-y^2}$ are nearly fully occupied for Zn and half occupied for Ni. From this Table we can argue that the Ni is in the high spin state. There is a spin of 0.72 on the $3d_{3z^2-r^2}$ MO with an overlap on the O p_z MO which has a Mulliken spin of 0.06. As expected in the case of Zn the Mulliken spin is almost zero for $3d_{3z^2-r^2}$ and $3d_{x^2-y^2}$. The naive picture of Fig. 17 is then not such a bad representation of the calculated case.

AO	$3d_{3z^2-r^2}$		$3d_{x^2-y^2}$		4s		O p_z		Op_σ	
	p_c	p_s	p_c	p_s	p_c	p_s	p_c	p_s	p_c	p_s
Cu	1.92	-0.01	1.41	0.43	0.51	-0.03	1.95	-0.01	1.67	0.01
Ni	1.21	0.72	1.18	0.55	0.38	0.03	1.90	0.06	1.69	-0.01
Zn	1.97	-0.01	1.98	-0.01	0.56	-0.03	1.95	0.00	1.74	-0.03

Table 11: Partial Mulliken charges (p_c) and partial Mulliken spin (p_s) of selected AO for Cu (unsubstituted case), Zn and Ni in the central position of the Cu_{13}, $ZnCu_{12}$ and $NiCu_{12}$ clusters respectively. p_c and p_s of the oxygens (Op_z and Op_σ) are the ones adjacent to the central atom.

6.4 Site assignments in copper NMR and NQR spectra

As already mentioned in Sec. 5 numerous NMR and NQR experiments on Zn substituted cuprates have been reported. In the present work we refer in particular to the measurements of Itoh *et al.* [59] and Williams *et al.* [141] who presented ^{63}Cu quadrupole resonance frequencies and spin-lattice relaxation rates in unsubstituted and Zn substituted $YBa_2Cu_3O_7$ and $YBa_2Cu_4O_8$. It has been observed that the main copper line broadens and slightly shifts to higher frequencies when Zn is substituted and that a new Cu satellite resonance occurs at a somewhat lower frequency. The intensity of this satellite peak grows with increasing Zn concentration. In addition, Itoh *et al.* [59] found that the Cu spin-lattice relaxation time, $^{63}T_1$, of the satellite peak is shorter than that of the main signal. This was interpreted as resulting from locally enhanced antiferromagnetic correlations in the neighborhood of Zn based on the site assignment that the NQR satellite peak comes from Cu atoms that are nearest neighbors to a substituted Zn atom. In this chapter we propose a different site assignment. We claim that the satellite peak is due to copper atoms that are *next* nearest neighbors to a substituted Zn atom. We will provide evidence for this in Sec. 6.4.1 by a direct calculation of copper EFGs in clusters representative of unsubstituted and Zn substituted La_2CuO_4, $YBa_2Cu_3O_7$, and $YBa_2Cu_4O_8$. In Sec. 6.4.4 we will consider measurements of copper spin-lattice relaxation rates in unsubstituted and Zn substituted cuprates to give additional independent arguments that support the site assignment suggested above. For Ni substituted cuprates no additional peak in the Cu spectra was observed [139][39]. Only a large broadening of the copper line has been reported [139]. Furthermore it was shown that Ni substitution has negligible effect on the spin-lattice relaxation rate and this independent of doping [56, 139]. In this section we will concentrate on the Zn impurity because it can be precisely compared with the experiments mentioned above which is not the case for the Ni impurity.

6.4.1 Electric Field Gradients

6.4.2 Zn

The extra calculations needed to study the changes of the copper EFGs in substances doped with impurities have been performed – for efficiency reasons – in clusters comprising nine copper atoms in the plane. As already stated in Sec. 6.3 this is justified since the changes in the electronic structure upon Zn substitution occur predominantly in the immediate vicinity of the impurity (see also Fig. 25). We have evaluated the electronic structure in clusters for La_2CuO_4, $YBa_2Cu_3O_7$, and $YBa_2Cu_4O_8$ and recorded the copper EFGs at all copper sites in the cluster which slightly differ due to finite size effects. Next we repeated the above calculations for Zn substituted clusters where the copper in the middle of the cluster (site M in the inset of Fig. 29) was replaced by a zinc. The copper EFGs were again calculated at all sites and were compared to those at the same sites in the unsubstituted clusters. The relative differences between the copper EFGs in the Zn substituted and in the unsubstituted clusters are shown with thick bars in

---

[39] Note that this is not restricted to Cu NMR (see [138])

Fig. 29. The solid (dotted) thick lines refer to situations where the copper in the substituted cluster is a nearest neighbor (NN) (next nearest neighbor (NNN)) to the Zn impurity. The EFG values for the NN coppers are all found to be larger than in the unsubstituted compounds whereas those for the NNN are smaller. For consistency, we repeated the above calculations but with Zn impurities in the edge and corner position (site E and site C). We included the results of these calculations with thin bars in Fig. 29 and – as a guide to the eye – grouped the copper EFGs resulting from coppers with the same distance (NN or NNN) to the Zn impurity by gray blocks. It is to be expected that asymmetrical substitution leads to somewhat deviating values, however, the qualitative findings of the above paragraph remain unchanged. We therefore conclude that the observed satellite peak with lower

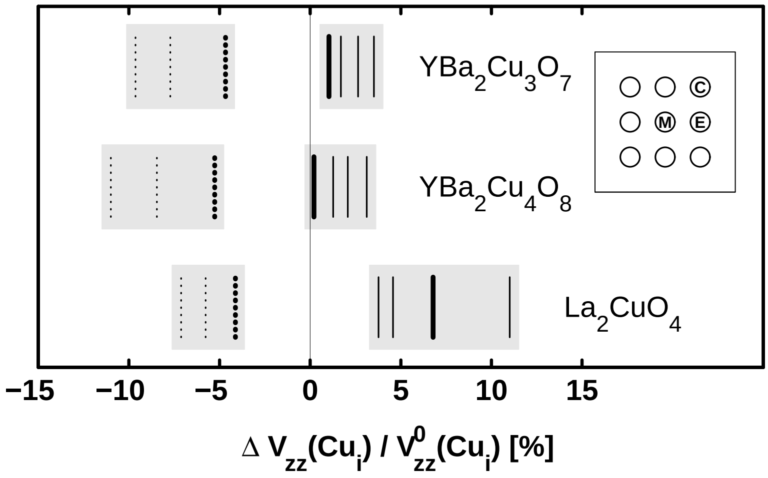

Figure 29: Relative differences between the copper EFGs in the Zn substituted and in the unsubstituted clusters with solid (dotted) lines referring to copper atoms which are NN (NNN) to the Zn impurity. In the inset: schematic representation of the Zn sites in the Cu_9 cluster with the site labelings used in the text (M: middle, E: edge, C: corner). Thick bars are for situations where the Zn is replaced at site M whereas thin bars denote results from clusters where the impurity has been inserted at sites E or C (see text).

NQR frequency originates from copper nuclei that are NNN to Zn. The NN will only broaden the main line and induce a shoulder towards higher frequency which is clearly visible in the Cu NQR spectrum [59, 141]. Note that in Refs. [59, 141] it was suggested by probabilistic arguments that the satellite peaks may originate from copper sites with one Zn NN. However, this site assignment is not unambiguous, since the probability of finding a copper coordinated with one Zn NN is the same as that of the Zn being in a NNN position to the copper, at least for low Zn concentration.

6.4.3 Ni

For completeness we also calculated the EFG at the Cu sites in the Ni doped La_2CuO_4 and $YBa_2Cu_3O_7$. If Ni is placed at the center of the Cu_9 cluster for La_2CuO_4 we obtain an increase of +0.5% for the EFG at Cu sites NN to Ni and a decrease of -3.0% for the EFG at the Cu sites NNN to Ni. For $YBa_2Cu_3O_7$ we obtain a decrease of -6.0% (-3.0%) for the EFG at Cu sites which are NN (NNN) to Ni. We therefore exclude a local wipeout effect of the NQR signal due to big differences in the EFG induced by Ni as argued by Williams *et al.*. The different EFGs at sites in the vicinity of the Ni impurity contribute to the broadening of the ^{63}Cu peak.

6.4.4 Comparison of the calculated hyperfine field with the NMR spin-lattice relaxation rate

6.4.5 Zn

In this paragraph we will give additional independent arguments that support the above conclusion about the site assignments in ^{63}Cu NQR spectra. The spin-lattice relaxation rate with the applied field along the c-axis, $^{63}T_{1c}^{-1}$, is due to fluctuations of the hyperfine fields in the perpendicular directions, i.e. in the CuO_2 plane. Adopting the notation of the Mila-Rice spin Hamiltonian [84], there is an on-site hyperfine interaction at the copper nucleus, denoted by $A_{0\perp}$, and a transferred field B. For the case of fully antiferromagnetically correlated copper spins, the rate $^{63}T_{1c}^{-1}$, is proportional to

$$^{63}T_{1c}^{-1} \propto (A_{0\perp} - 4B)^2 \tag{61}$$

since each of the four NN contributes one B (see Sec. 2.5). A Zn NN, however, will hardly transfer any spin density to the Cu (see Fig. 23) and we expect

$$^{63}T_{1c}^{-1} \propto (A_{0\perp} - 3B)^2. \tag{62}$$

Typical values [90] are $A_{0\perp} = 0.29$ μeV and $B = 0.4$ μeV, which would reduce $^{63}T_{1c}^{-1}$ by $1-(A_{0\perp}-3B)^2/(A_{0\perp}-4B)^2 = 52$ %. Note that if there were no correlations at all, this reduction would still be $1-(A_{0\perp}^2+3B^2)/(A_{0\perp}^2+4B^2) = 22$ %.

To obtain a more quantitative statement we can use the results of our cluster calculations in the $Cu_9O_{42}/Cu_{12}La_{50}$ and $Cu_8ZnO_{42}/Cu_{12}La_{50}$ clusters for the La_2CuO_4 system. The circles in Fig. 30 indicate the calculated Fermi contacts, D(Cu), in the unsubstituted Cu_9 cluster recorded at different positions in the cluster (see inset of Fig. 29) with different numbers of nearest neighbors. The slope of the fitted straight line gives the transferred contribution and the intersect the on-site contribution. The squares denote results in a Zn substituted cluster. The arrows are meant to indicate that upon losing one Cu neighbor the Fermi contact drops by about $0.6B$. Since there is some spin density on the oxygen between Zn and Cu, the change of the total transferred spin density is not from $4B$ to $3B$ but to $3.4B$ which still leads to an enormous reduction of the spin-lattice relaxation rate.

For a Cu nucleus adjacent to a Zn we therefore expect a considerably reduced spin-lattice relaxation rate. If these copper nuclei contributed to the satellite peak they would relax slower than those contributing to the main peak in contrast to the observations (see Fig. 7 in Ref. [59]). In addition the spin-lattice relaxation rate of nuclei contributing to the main peak would not change when substituting Zn atoms in the cuprate plane. However, the data in Fig. 6 of Ref. [59] show that, in fact, the relaxation of the copper nuclei in the main peak is slower in Zn substituted compounds. This behavior is expected only if, instead, the Cu atoms nearest neighbored to Zn contribute to the main peak.

We thus conclude that the satellite peak at which a larger rate is observed cannot be attributed to a Cu which is nearest neighbor to Zn thus providing an additional argument to the assignment made in Sec. 6.4.1.

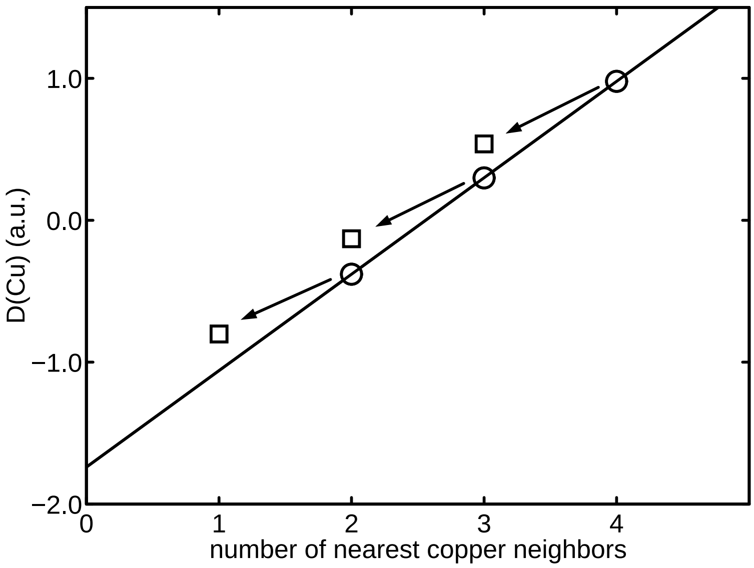

Figure 30: Contact spin density $D(\mathrm{Cu})$ in a_B^{-3} vs. the number of nearest copper neighbors. The circles result from calculations for the unsubstituted compound whereas the squares refer to Zn substituted clusters.

6.4.6 Ni

Finally in the case of Ni the calculated Fermi contact term recorded at Cu sites NN to the Ni changes less than 0.4% from the unsubstituted value. In this case we expect no significant reduction of the spin-lattice relaxation rate of that expected for the unsubstituted case. This is in agreement with experiments [56, 139].

7 Comparison of the electronic structures of La_2CuO_4, $Sr_2CuO_2Cl_2$ and $Sr_2CuO_2F_2$

This section has been published in Ref. [24]. In La_2CuO_4 the bonds to the two apical oxygens of the sixfold coordinated Cu are thought to be more ionic in character than the bonds to the planar oxygens. With the discovery [143] of superconductivity in $YBa_2Cu_3O_7$ where the planar copper is only fivefold coordinated, however, the interest in the role of the apical oxygens for the mechanism of high-temperature superconductivity was no longer in the focus of the mainstream research.

New interest in the apical anions arose when the oxyhalides $Sr_2CuO_2Cl_2$ and $Sr_2CuO_2F_2$ were investigated. The structural and magnetic properties of these compounds studied with a number of experimental techniques like x-ray scattering, neutron scattering, susceptibility, and muon spin rotation [85, 135, 74] are almost identical to the ones in La_2CuO_4 and they all have the general formula $M_2CuO_2A_2$ with metal cations M=La or Sr and apical anions A=O, Cl or F. However $Sr_2CuO_2Cl_2$ although potentially suitable of electron-type doping and superconductivity has not led to any successful superconductor, in contrast with Sr- and Ba-doped La_2CuO_4. For the $Sr_2CuO_2F_2$ superconductivity has been successfully reported [11] in $Sr_2CuO_2F_{2+\delta}$ below $\sim$ 46K. The excess fluorine is the dopant but it is controversial to which interstitial site(s) the excess fluorine should be assigned to as it is difficult using x-ray or neutron diffraction to distinguish the positions of O and F ions since they have similar scattering functions. Note that superconductivity has also been reported in Na doped $Ca_2CuO_2F_2$ with a T_c of 26 K [49] which has also the same layered perovskite body-centered-tetragonal crystal structure. In this case there is little evidence for the presence of interstitial atoms. These discoveries introduced a new class of cuprates superconductors without apical oxygen. The $Sr_2CuO_2Cl_2$ compound is often considered as a perfect S=1/2 two dimensional Heisenberg antiferromagnet, $H=J\sum S_i S_j$, where J ($\approx$ 1500 K) [129] [40]. There is also an important difference between the Cl-substituted materials and La_2CuO_4. While the latter undergoes an orthorhombic distortion, the Cl-substituted material remains tetragonal down to at least 10 K. This fact is believed to explain the different behaviour of the susceptibility near T_N for the two systems [135].

The crystal structure of $Sr_2CuO_2Cl_2$ is depicted schematically in Fig. 31 and compared with the ones of La_2CuO_4 and Nd_2CuO_4. Because of the different interplane structure of $Sr_2CuO_2Cl_2$ (the Cu-O planes are separated by puckered SrCl rocksalt layers) it has a c-axis parameter of about 20% larger than other cuprate compounds. Like Nd_2CuO_4, $Sr_2CuO_2Cl_2$ has no apex oxygen.

---

[40] The isotropic 2D Heisenberg behaviour in this compound is robust even down to $\approx$ 280K!

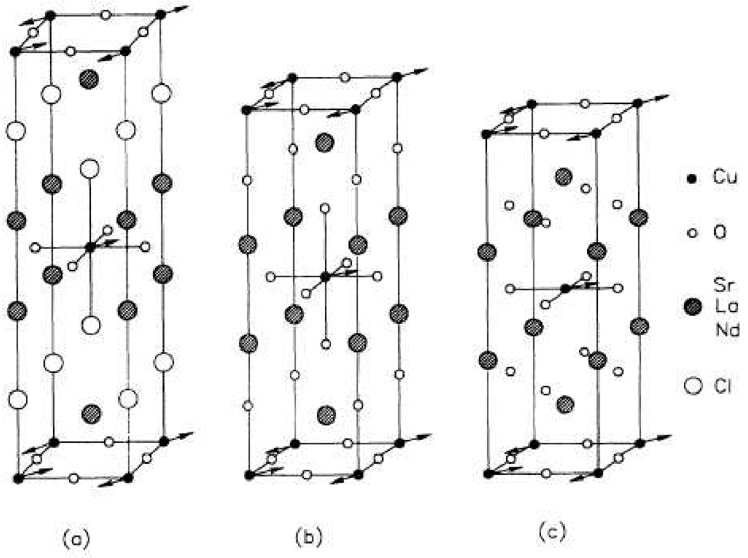

Figure 31: Schematic representation of the crystal structures of (a) $Sr_2CuO_2Cl_2$ (b) La_2CuO_4 and (c) Nd_2CuO_4. The arrows on coppers indicate the spin direction.

As pointed out by Le *et al* [74] this results in a net positive charge around the copper atoms and thus electrons may be attracted to these sites. This is this similarity between $Sr_2CuO_2Cl_2$ and Nd_2CuO_4 which has suggested that $Sr_2CuO_2Cl_2$ may be a candidate for electron doping.

The electronic structure of $Sr_2CuO_2Cl_2$, $Sr_2CuO_2F_2$ and $Ca_2CuO_2Cl_2$ was studied by Novikov *et al.* [91] with band structure calculations. They found that the band structures of these compounds are very similar and have the same features common to all HTSC, that is the electronic structure shows strong two-dimensional features including a low density of states at E_F and a simple Fermi surface of the form of a rounded square. This was confirmed by ARPES (for a detailed review on the ARPES measurement on oxyhalides see Damascelli *et al.* [39]). In their calculation the lack of the apical oxygen seems to have no effect on the states close to E_F.

What changes do occur in the local electronic structure when the apical oxygens are replaced by Cl? To answer this question we have extended our investigations of the cluster method to the oxyhalides. We will compare the local electronic structures of the three compounds La_2CuO_4, $Sr_2CuO_2Cl_2$ and $Sr_2CuO_2F_2$. Effectively we are studying the changes introduced by replacing the apical oxygen ions in La_2CuO_4 with chlorine or fluorine ions, the strontium counter ions simply maintaining the correct charge balance, in an attempt to rationalize the differences qualitatively.

7.1 Clusters and computational methods

The clusters used for this section are described in detail in Sec. 3 For the atoms of the core of the cluster the standard 6-311G basis set was employed. Again the density functional method with the local-density and generalized-gradient approximations was used.

7.2 Electric field gradients

We first note that the calculated electric field gradient at the copper nucleus in $\mathrm{Sr_2CuO_2Cl_2}$ is considerably smaller than in $\mathrm{La_2CuO_4}$ corresponding to a ^{63}Cu quadrupole frequency of about 20 MHz which is in reasonable agreement with the experiment (Thurber found 26.55 MHz [129]). The theoretical values for the copper EFG in $\mathrm{Sr_2CuO_2Cl_2}$ are clearly smaller than those in $\mathrm{La_2CuO_4}$. This finding which well reproduces the experimental trend originates from a charge redistribution from the copper $3d_{3z^2-r^2}$ to the $3d_{x^2-y^2}$ AO in the Sr compound.

7.3 Molecular orbitals

Since spin-polarized calculations have been carried out the spin-up molecular spin-polarized orbital (MSO) energies are different from the spin-down MSO energies. In Fig. 33 we have plotted the energies of the calculated MSOs which are less than seven eV below the Fermi energy. Solid bars identify the spin-up MSOs and dotted bars the spin-down MSOs. The highest occupied MSO (HOMSO) is an anti-bonding combination of basis orbitals predominantly between Cu $3d_{\mathrm{x}^2-\mathrm{y}^2}$ and the four planar O $2p_\sigma$ atomic orbitals (AO). This HOMSO is probably best interpreted as non-bonding or at most very weakly anti-bonding. This is occupied by a spin-up electron but the corresponding spin-down anti-bonding MSO (1.3 eV higher) is unoccupied and is referred to as the lowest unoccupied MSO (LUMSO). Also in Fig. 33 the composition of each MSO in terms of the more important atomic orbitals are indicated.

Just below these are MSOs which are interpreted to be the antibonding combinations of the Cu $3d_{3\mathrm{z}^2-\mathrm{r}^2}$ and apical O $2p_\mathrm{z}$ orbitals. These are followed at energies around -1.5 eV by MSOs that can be formed as anti-bonding combinations with the three other Cu 3d AOs, all thought to be effectively non-bonding. Deeper in energy, between -2.6 and -4.4 eV, are the MSOs that are composed of oxygens only without contributions from Cu. They comprise the $2p_\mathrm{z}$ AOs of the planar oxygens and the $2p_\mathrm{x}$ and $2p_\mathrm{y}$ of the apex oxygens. The MSOs at lower energies are bonding combinations between the Cu $3d$ and the O $2p$ AOs.

The $3d_{3\mathrm{z}^2-\mathrm{r}^2}$ orbital participates at slightly lower orbital energies than the $d_{x^2-y^2}$ orbital in $\mathrm{La_2CuO_4}$ as expected for the crystal field of a distorted octahedron extended along the z-axis. The corresponding $3d_{3z^2-r^2}$ orbital in the $Sr_2CuO_2Cl_2$ compound is lowered significantly in energy, even below the $3d_{xy}$, $3d_{yz}$ and $3d_{xz}$ orbital energies, which is characteristic of a square planar complex. The chlorine ions are so far removed that their influence on the crystal field is now relatively small. This may account for the observation that this crystal behaves like a 'perfect' two-dimensional antiferromagnet. This is to be contrasted with the occupied orbitals of the La compound which involve the $3d_{3\mathrm{z}^2-\mathrm{r}^2}$ orbital as well as the apical oxygen orbitals. The planar antiferromagnetic behaviour is clearly disturbed by this extra delocalization in the z-direction.

7.4 Partial charges

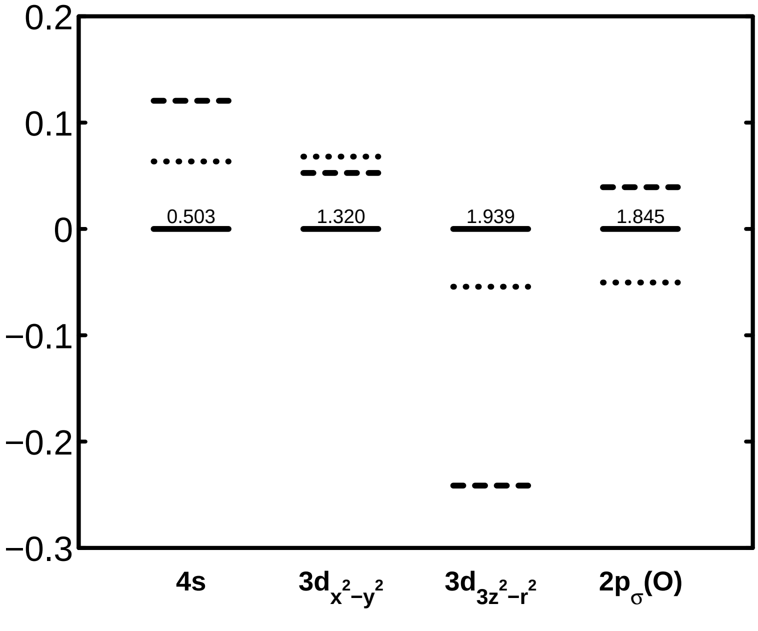

Figure 32: Changes of the partial Mulliken populations of selected atomic orbitals for La_2CuO_4 (solid), $Sr_2CuO_2Cl_2$ (dotted) and $Sr_2CuO_2F_2$ (dashed).

In Fig. 32 the partial Mulliken charges of selected AO are shown. As discussed in Sec. 4 there are about 0.5 electrons in the copper 4s AO for La_2CuO_4. This value is even higher (0.57/0.62) with Cl/F in the apical positions. Our total Mulliken charges for $Sr_2CuO_2F_2$ differ considerably from those obtained with the unrestricted Hartree-Fock (HF) method [76]. As it had already been discussed [53] for La_2CuO_4, the HF result suggests an almost purely ionic bonding with small overlap between Cu and the planar O. In contrast, the density functional method emphasizes the covalency and leads to an atomic spin density of about 0.63 on the copper ion which is at variance with the HF value [76] of 0.9.

7.5 Hyperfine coupling

	La_2CuO_4	$Sr_2CuO_2Cl_2$
a_{0iso}	-1.750	-2.153
b_{iso}	0.738	0.789
$a^{\parallel}_{0dip}$	-3.521	-3.288
$b^{\parallel}_{dip}$	0.070	0.032
$a^{\parallel}_{0so}$	2.405	2.173
$a^{\parallel}_{0tot} + 4b^{\parallel}_{tot}$	0.363	0.014

Table 12: On-site and transferred hyperfine parameters for the copper atom. These parameters are scaled with the Mulliken spin density ρ_s in the cluster with $M = 6$, which is the assumed value for the Mulliken spin density in the infinite cluster (see [53]). The total hyperfine fields are $a^{\parallel}_{0tot} = a_{0iso} + a^{\parallel}_{0dip} + a^{\parallel}_{0so}$ and $b^{\parallel}_{tot} = b_{iso} + b^{\parallel}_{dip}$.

The large cluster $Cu_5O_{16}Cl_{10}/Cu_8Sr_{34}$ which comprises five copper atoms has been calculated with spin multiplicities M = 6 and 4[41]. We then have performed the same analyses of the resulting spin densities as before [53, 106] in La_2CuO_4 and $YBa_2Cu_3O_7$. The estimated effective exchange interaction in $Sr_2CuO_2Cl_2$ is 30 % larger than in La_2CuO_4 and the hyperfine field transferred from the four nearest neighbor copper ions to the copper nucleus is 15 % larger. Table 12 collects the values for the hyperfine coupling parameters at the copper sites. Note that in $Sr_2CuO_2Cl_2$ the hyperfine fields nearly cancel.

---

[41] We did not obtain convergence for the M=2 multiplicity

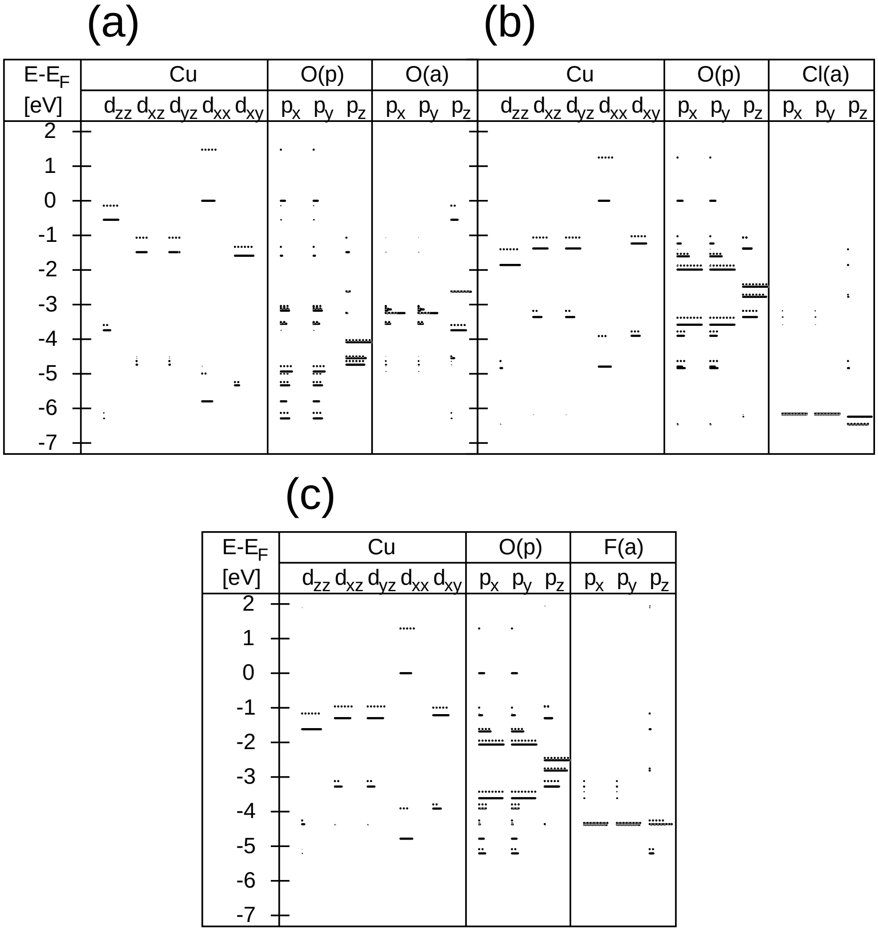

Figure 33: Energies of the highest occupied MSOs in the clusters (a) CuO_6/Cu_4La_{10}, (b) CuO_4Cl_2/Cu_4Sr_{10} and (c) CuO_4F_2/Cu_4Sr_{10} with contributions of the individual AOs. The length of the bar is proportional to the square of the expansion coefficient of the MSO into the corresponding AOs. Spin-up (spin-down) orbitals are denoted by solid (dotted) bars.

8 Summary and conclusions

In this work the electronic and magnetic properties of several high temperature superconducting cuprates have been investigated in the framework of spin polarized density functional theory using a cluster model. As a significant improvement of our previous work [53, 106] we were able to include up to 13 planar copper atoms together with the surrounding planar and apical oxygen atoms in our clusters. Electric field gradients, and magnetic hyperfine constants at copper sites have been calculated and compared to experimental results.

In the first part of this work the electronic and magnetic properties in the CuO_2 planes of the electron doped cuprates Nd_2CuO_4 were carefully examined and compared to the ones of the hole doped cuprate La_2CuO_4 already obtained by Stoll *et al.* [120]. In particular the electric field gradients at the planar copper sites were determined and compared with the corresponding experimentally measured NQR frequencies. We obtained a very good agreement with experiments. By simulating doping and using a Mulliken population analysis we showed that the simple ionic model widely used by the HTSC community is far from being realistic. In the simplistic ionic model the holes introduced in the planes by doping La_2CuO_4 enter exclusively in the planar oxygen p_σ AO. In the same model the electrons introduced by doping Nd_2CuO_4 enter exclusively in the planar copper $3d_{x^2-y^2}$ AO. The behavior of the population of the AOs with this simple ionic model is depicted in Fig. 34. Note that the copper 4s orbital, which is assumed to be empty, and the copper $3d_{3z^2-r^2}$ as well as the apical oxygen $2p_z$ orbitals, which are assumed to be fully occupied, are not represented. Our calculations show a rather different population of the AOs and a different behavior under doping than the ionic model. This is shown in Fig. 35 which summarizes the essential features of Fig. 11 which have been extensively discussed in Sec. 4. First of all there is a mismatch in the populations of Nd_2CuO_4 and La_2CuO_4 at zero doping due to the rather different crystal structure between the two materials (absence of apical oxygens in Nd_2CuO_4). The significant jump in the $3d_{3z^2-r^2}$ in the occupancy of the orbital between La_2CuO_4 and Nd_2CuO_4 is the origin of the difference in the nuclear quadrupole frequency between the undoped parent compounds Nd_2CuO_4 (ν_Q = 14 MHz) and La_2CuO_4 (ν_Q = 33 MHz). Furthermore there is a significant population of the 4s orbital in both Nd_2CuO_4 (about 0.65 electrons) and La_2CuO_4(about 0.5 electrons) in the undoped parent compounds. For La_2CuO_4 doping not only depopulates the oxygen $2p_\sigma$ orbital but also affects other orbitals. For the Nd_2CuO_4 compound, as can be seen in Fig. 35 doping mainly affects the $3d_{3z^2-r^2}$ (green), $3d_{x^2-y^2}$ (magenta), and the 4s (black) orbitals. As the 4s orbital does not contribute to the EFG, the strong sensitivity of the nuclear quadrupole frequency under doping observed experimentally ($\nu_Q \leq 2$ MHz for 15% doping) can be explained mainly by a change of the population of *both* the $3d_{3z^2-r^2}$ and $3d_{x^2-y^2}$ orbitals. These arguments should be taken into account by models attempting to explain electron doped cuprates.

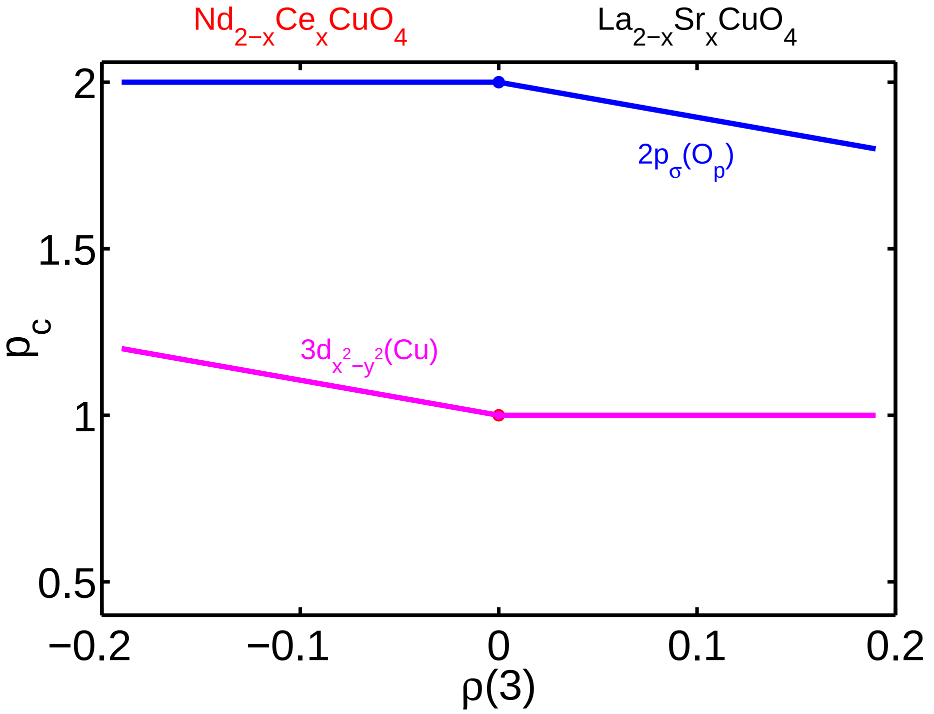

Figure 34: Partial Mulliken populations of the atomic orbitals versus doping level $\rho(3)$ for $La_{2-x}Sr_xCuO_4$ and $Nd_{2-x}Ce_xCuO_4$ in the ionic model. In this simple model the doped holes provoke a depopulation of the planar oxygen $2p_\sigma$ AO (blue). The doped electrons lead to a increase of the population of the Cu $3d_{x^2-y^2}$ AO (magenta).

The objective of the second part of this work was a first-principles investigation of the effect on the local electronic structure of Zn and Ni impurities that substitute Cu atoms in the CuO_2 plane of the cuprates. This was performed in the framework of the cluster model with clusters representative of La_2CuO_4, $YBa_2Cu_3O_7$, and $YBa_2Cu_4O_8$ and the respective Zn and Ni substituted compounds.

For the unsubstituted compounds the antiferromagnetic spin arrangement with the Mulliken spin densities of neighboring copper atoms having opposite sign could be well reproduced. Calculations in clusters where a Cu was replaced by a Zn atom revealed almost no spin density at the Zn site whereas the antiferromagnetic spin alignment around the impurity was left virtually intact. The calculations with Ni substituted clusters reveal clearly that Ni carries a spin and that the spin state of Ni is near the ideal S=1 high spin state.

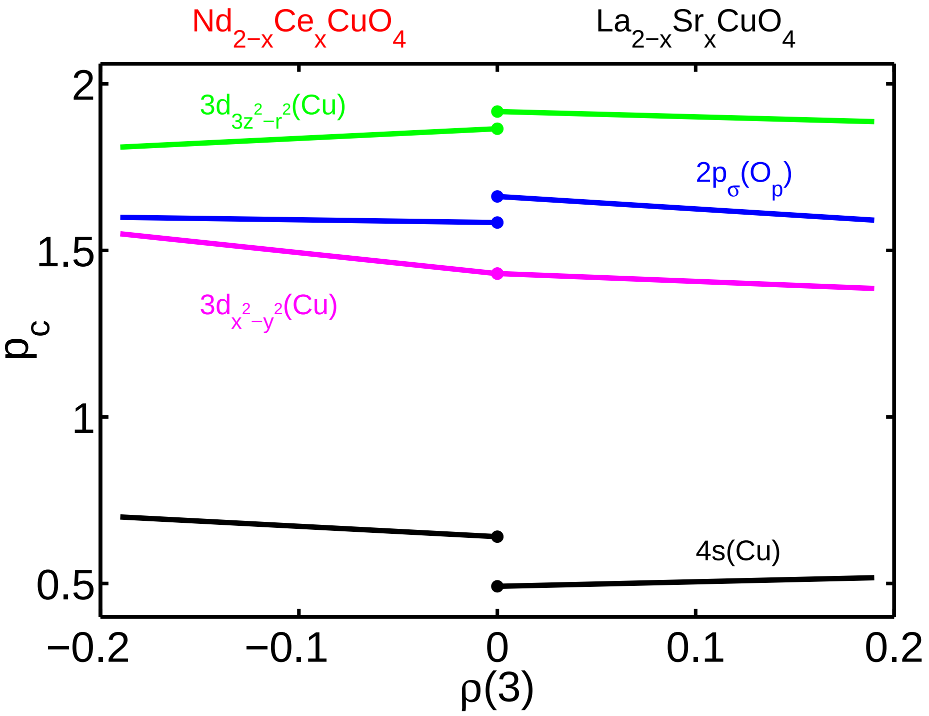

Figure 35: Partial Mulliken populations of the atomic orbitals versus doping level $\rho(3)$ for $La_{2-x}Sr_xCuO_4$ and $Nd_{2-x}Ce_xCuO_4$, as calculated by the cluster method which represents a more realistic picture than the ionic model. The following orbitals are represented: $3d_{3z^2-r^2}$ (green), 4s (black), $3d_{x^2-y^2}$ (magenta) and the planar oxygen $2p_\sigma$ (blue). The $2p_z$ orbital of the apical oxygen is not represented for simplicity. By doping with electrons there is mainly a change in the population of the $3d_{3z^2-r^2}$ and the $3d_{x^2-y^2}$ AOs.

Using the same clusters, we observed in general that the changes in the charge distribution upon Zn and Ni substitution remain rather local and do not extend to more than the next nearest copper atoms. In particular the Mulliken charge at the oxygens adjacent to the Zn impurity was significantly reduced to more negative values compared to the Zn-free case. For La_2CuO_4 the values of the Mulliken charge differences at different sites in the Cu_{13} cluster are given in Table 8.

For comparison, we simulated a hole doping of about 8 % in unsubstituted La_2CuO_4 by removing one electron from the Cu_{13} cluster and observed that in general impurity substitution seems to compensate the effects of hole doping on the charge distribution. We interpreted this as evidence for enhanced antiferromagnetic correlations around Zn impurities. In the case of Ni we observed a similar decrease at the oxygens adjacent to the Ni impurity. This effect was however much less pronounced than in the Zn case. This

Site	Ni	Zn
NN O	-0.016	-0.067
NNN O	-0.002	0.002
NNNN O	-0.001	0.004
NN Cu	-0.005	-0.001
NNN Cu	-0.002	-0.004
NNNN Cu	0	0
Central atom	1.066	-0.687
apex O (center)	0.048	0.001

Table 13: Mulliken charge differences for La_2CuO_4 at different sites in the Cu_{13} cluster ($\Delta\rho_{Mull}$=ρ(substituted cluster)-ρ(pure crystal)) induced by Zn and Ni substitutions at central positions.

result provides one argument why Zn is more effective than Ni in destroying superconductivity.

Furthermore, we also calculated electric field gradients at Cu sites in unsubstituted and Zn substituted clusters. We found that the EFGs at the Cu sites that are nearest neighbors to a Zn impurity are slightly larger than in the unsubstituted compounds, whereas those at sites NNN to Zn are about 5 % smaller. We therefore proposed a new site assignment for Cu NQR spectra in Zn substituted compounds: the satellite peak at lower frequencies originates from NNN Cu to Zn whereas the NN Cu induce a shoulder in the main peak towards higher frequencies. We also observed a significant reduction of the transferred hyperfine field on a Cu NN to Zn. The site assignment based on the calculated EFG values is corroborated by arguments concerning the different spin-lattice relaxation rates of nuclei in the main and the satellite peak. We obtained a similar modification of the EFGs at the Cu site NN and NNN to Ni, but in contrast to Zn we found no reduction of the transferred hyperfine field for a copper site NN to Ni, in accordance with experiments.

Finally we We finally conclude a rather different behaviour of Zn and Ni impurities which could explain the stronger effect of the Zn impurity compared to Ni impurity in destroying superconductivity.

In order to precisely identify the role of the apical anions on the electronic structure we investigated in the third part of this work the electronic structure of La_2CuO_4, $Sr_2CuO_2Cl_2$, and $Sr_2CuO_2F_2$ which have O, Cl, and F atoms respectively at the apical position. Cluster calculations show that the highest occupied molecular orbital in all three compounds is formed by the Cu $3d_{x^2-y^2}$ and the planar O $2p_\sigma$ AO's and exhibits a similar degree of covalency. The out-of-plane orbitals, however, are quite different with the $3d_{3z^2-r^2}$ AO lowered significantly in energy for Cl and F at the apical positions. It is difficult at present to ascertain whether the energy of the Cu 3d$_{3z^2-r^2}$ is sensitive to the effects of local dopant. The sensitivity of the energy of this orbital to the environment is however established and is the only obvious difference in the electronic structure between these compounds. The bond between the copper and the apical ligands are clearly much more ionic for both fluorine and chlorine than oxygen, in line with expectation. Finally we have noticed that the 4s populations vary significantly among the three compositions.

References

[1] M. Abe, K. Kumagai, S. Awaji, and T. Fujita, Physica C, **160**, 8 (1989).

[2] A. A. Abrikosov, and L. P. Gorkov, 1960, Zh. Eksp. Teor. Fiz. **39**, 1781, [Sov. Phys. JETP 12, 1243 (1961)].

[3] A. A. Abrikosov, L. P. Gorkov, I. E. Dzyakishinsky, “Methods of quantum field theory in statistical physics”, Prentice-Hall (1963).

[4] A. A. Abrikosov, “Fundamental of the theory of metals”, North-Holland (1999).

[5] A. A. Abrikosov, Physica C **397**, 77 (2003).

[6] L. Alff, A. Beck, R. Gross, A. Marx, S. Kleefisch, Th. Bauch, H. Sato, M. Naito, and G. Koren, Phys. Rev. B. **58**, 11197 (1998).

[7] L. Alff, S. Meyer, S. Kleefisch, U. Schoop, A. Marx, H. Sato, M. Naito, and R. Gross, Phys. Rev. Lett., **83**, 2644 (1999).

[8] J. F. Annett, “Superconductivity, superfluids, and condensates”, Oxford (2004).

[9] L. Alff, Y. Krockenberger, B. Welter, M. Schoecke, R. Gross, D. Manske, and M. Naito, nature **422**, 698 (2003).

[10] I. J. Aitchison, I. J. Aitchison, A. J. Hey, “Gauge theories in particle physics”, Institue of Physics publishing (1989).

[11] M. Al-Mamouri, P. P. Edwards, C, Greaves, and M. Slaski, Nature **369**, 382 (1994).

[12] P. W. Anderson, J. Phys. Chem. Solids **11**, 26 (1959).

[13] P. W. Anderson, science **235**, 1196 (1987).

[14] “The theory of superconductivity in high-T$_c$ cuprates”, P. W. Anderson, Princeton University Press (1997).

[15] N. P. Armitage, D. H. Lu, D. L. Feng, C. Kim, A. Damascelli, K. M. Shen, F. Ronning, and Z.-X. Shen, Y. Onose, Y. Taguchi, and Y. Tokura Phys. Rev. Lett. 86, 1126 (2001).

[16] A. V. Balatsky, M. I. Salkola, and A. Rosengren, Phys. Rev. B **51**, 15547 (1995).

[17] A. V. Balatsky, cond-mat/0411318 submitted to Rev. Mod. Phys.

[18] H. Balci, V. N. Smolyaninova, P. Fournier, A. Biswas, and R. L. Greene, Phys. Rev. B **66**, 174510 (2002).

[19] J. Bardeen, L. N. Cooper, and J. R. Schrieffer, Phys. Rev. **108**, 1175 (1957).

[20] A. D. Becke, Phys. Rev. A **38**, 3098 (1988).

[21] A. D. Becke, J. Chem. Phys. **88**, 2547 (1988).

[22] J. G. Bednorz and K. A. Müller, Z. Phys. **64**, 189 (1986).

[23] C. Bernhard, Ch. Niedermayer, T. Blasius, G. V. M. Williams, R. De Renzi, C. Bucci, and J. L. Tallon, Phys. Rev. B 58, 8937 (1998).

[24] C. Bersier, E. P. Stoll, P. F. Meier and T. A. Claxton, J. Supercond. Inc. Nov. Magn. **15**, 399 (2004).

[25] C. Bersier, S. Renold, E. P. Stoll, and P. F. Meier, Phys. Rev. B **72**, 224514 (2005).

[26] C. Bersier, S Renold, E. P .Stoll and P. F. Meier, J. Phys.: Condens. Matter **18**, 7481 (2006).

[27] C. Berthier, M.-H. Julien, M. Horvatić, and Y. Berthier, J. Phys. I France **6**, 2205 (1996).

[28] G. Blumberg, A. Koitzsch, A. Gozar, B. S. Dennis, C. A. Kendziora, P. Fournier, and R. L. Greene, Phys. Rev. Lett. **88**, 107002 (2002).

[29] J. Bobroff, H. Alloul, Y. Yoshinari, P. Mendels, A. Keren, N. Blanchard, G. Collin, and J. F. Marucco, Phys. Rev. Lett. **79**, 2117 (1997).

[30] J. Bobroff, W. A. MacFarlane, H. Alloul, P. Mendels, N. Blanchard, G. Collin, and J.-F. Marucco, Phys. Rev. Lett. **83**, 4381 (1999)

[31] J. Bobroff *et al.* Cond-Mat/0008396.

[32] J. Bobroff, H. Alloul, W. A. MacFarlane, P. Mendels, N. Blanchard, G. Collin, and J.-F. Marucco, Phys. Rev. Lett. **86**, 4116 (2001).

[33] D. A. Bonn, S. Kamal, K. Zhang, R. Liang, D. J. Baar, E. Klein, and W. N. Hardy, Phys. Rev. B, **50**, 4051 (1994).

[34] P. Bordet, C. Chaillout, J. J. Capponi, J. Chenavas, and M. Marezio, Nature **327**, 687 (1987).

[35] L. S. Borkowski and P. J. Hirschfeld, Phys. Rev. B **49**, 15404 (1994).

[36] D. Brinkmann and M. Mali, in *NMR Basic Principles and Progress*, Vol. 31 (Springer, Heidelberg, 1994), p. 171.

[37] C.-T. Chen, P. Seneor, N.-C. Yeh, R. P. Vasquez, L. D. Bell, C. U. Jung, J. Y. Kim, M.-S. Park, H.-J. Kim, and S.-I. Lee, Phys. Rev. Lett. **88**, 227002 (2002).

[38] L. N. Cooper, Phys. Rev. **104**, 1189 (1956).

[39] A. Damascelli, Z. Hussain, and Z.-X. Shen, Rev. Mod. Phys. **75**, 473 (2003).

[40] P. G. de Gennes, *Superconductivity of Metals and Alloys* (Addison-Wesley, New York, 1996).

[41] R. M. Dreizler, and E. K. U. Gross, *Density Functional Theory* (Springer, Berlin, 1990).

[42] P. Fischer, J. Karpinski, E. Kaldis, E. Jilek, and S. Rusiecki, Solid State Commun. **69**, 531-533 (1989).

[43] M. J. Frisch, *et al.*, Gaussian 03, Revision C.02, Frisch, Gaussian, Inc., Wallingford CT, 2004.

[44] D. Goldschmidt, Y. Direktovitch, A. Knizhnik, and Y. Eckstein, Phys. Rev. B, **54**, 13 348 (1996).

[45] R. Gupta and M. Gupta, Solid State Comm., **67**, 129 (1988).

[46] R. Gupta and M. Gupta, Physica C **305**, 179 (1998).

[47] R. Gupta and M. Gupta, Phys. Rev. B **59** 3381 (1999).

[48] D. Haskel, E. A. Stern, F. Dogan, and A. Moodenbaugh, J. Synchrotron Rad., **8**, 186 (2001). D. Haskel, E. A. Stern, V. Polinger, and F. Dogan, Phys. Rev. B, **64**, 104510 (2001).

[49] Z. Hiriri, N. Kobayashi and M. Takano, Nature 371, 139 (1994).

[50] P. Hohenberg and W. Kohn, Phys. Rev. **136**, B864 (1964).

[51] E. W. Hudson, K. M. Lang, V. Madhavan, S. H. Pan, H. Eisaki, S. Uschida, and J. C. Davis, nature, **411**, 420 (2001).

[52] P. Hüsser, "Calculation of the Electronic Structure of La_2CuO_4", thesis, Zürich 1999.

[53] P. Hüsser, H. U. Suter, E. P. Stoll, and P. F. Meier, Phys. Rev. B **61**, 1567 (2000).

[54] T. Imai, C. P. Slichter, K. Yoshimura, and K. Kosuge, Phys. Rev. Lett. **70**, 1002 (1993).

[55] T. Imai, C. P. Slichter, J. L. Cobb, and J. T. Markert, J. Phys. Chem. Solids **56**, 1921 (1995).

[56] K. Ishida, Y. Kitaoka, N. O. Gata, T. Kamino, K. Asayama, J. R. Cooper, and N. Athanassopoulou, J. Phys. Soc. Jpn. **62**, 2803 (1993).

[57] K. Ishida, T. Tanaka, H. Yamanaka, T. Mito, Y. Tokunaga, K. Yoshida, K. Yamazoe, S. Oshugi, and Y. Kitaoka, Physica C **282-287**, 1367 (1997).

[58] Y. Itoh, T. Machi, N. Watanabe, S. Adachi, and N. Koshizuka J. Phys. Soc. Jpn. **70**, 1881 (2001).

[59] Y. Itoh, T. Machi, C. Kasai, S. Adachi, N. Watanabe, N. Koshizuka, and M. Murakami, Phys. Rev. B **67**, 064516 (2003).

[60] J. D. Jackson, *Klassische Elektrodynamik* (de Gruyter, Berlin, 1982).

[61] M.-H. Julien, T. Fehér, M. Horvatić, C. Berthier, O. N. Bakharev, P. Ségransan, G. Collin, and J.-F. Marucco, Phys. Rev. Lett. **84**, 3422 (2000).

[62] C. U. Jung, J. Y. Kim, Min-Seok Park, Mun-Seog Kim, Heon-Jung Kim, S. Y. Lee, and Sung-Ik Lee, Phys. Rev. B **65** 172501 (2002).

[63] S. Kambe, H. Yasuoka, H. Takagi, S.-I. Uschida, and Y. Tokura, J. Phys. Soc. Jpn. **60**, 400 (1991).

[64] I. G. Kaplan, J. Soullard, J. Hernández-Cobos, and R. Pandey, J. Phys.: Condens. Matter **11**, 1049 (1999).

[65] I. G. Kaplan, J. Soullard, and J. Hernández-Cobos, Phys. Rev. B **65**, 214509 (2002).

[66] S. Kashiwaya, T. Ito, K. Oka, S. Ueno, H. Takashima, M. Koyanagi, Y. Tanaka, and K. Kajimura, Phys. Rev. B **57**, 8680 (1998).

[67] R. Kilian, S. Krivenko, G. Khaliullin, and P. Fulde, Phys. Rev. B, **50**, 13020 (1994).

[68] M.-S. Kim, J. A. Skinta, T. R. Lemberger, A. Tsukada and M. Naito, Phys. Rev. Lett., **91**, 087001 (2003).

[69] “A chemist’s guide to density functional theory”, W. Koch, M. C. Holthausen, Wiley (2001).

[70] W. Kohn and L. J. Sham, Phys. Rev. **140**, A1133 (1965).

[71] J. D. Kokales, P. Fournier, L. V. Mercaldo, V. V. Talanov, R. L. Greene, and S. M. Anlage , Phys. Rev. Lett. **85**, 3696 (2000).

[72] K. Kumagai, M. Abe, S. Awaji, and T. Fujita, Physica C, **162**, 181 (1989).

[73] K. Kumagai, M. Abe, S. Tanaka and T. Kishino, Physica C, **185**, 1073 (1991).

[74] L. P. Le, G. M. Luke, B. J. Sernlieb, Y. J. Uemura, J. H. Brewer, T. M. Riseman, D. C. Johnston, and L. L. Miller, Phys. Rev. B **42**, 2182 (1990).

[75] C. Lee, W. Yang, and R. G. Parr, Phys. Rev. B **37**, 785 (1988).

[76] W. C. Mackrodt, H. J. Gotsis and N. I. Allan, Ber. Bunsenges. Phys. Chem. **101**, 1242 (1997).

[77] A.V. Mahajan, H. Alloul, G. Collin, and J.F. Marucco Phys. Rev. Lett. **72**, 3100 (1994).

[78] S. Massida, N. Hamada, J. Yu, and A. J. Freeman, Physica C **157**, 571 (1989).

[79] "The cold wars: a history of superconductivity", J. Matricon and G. Waysand, Rutgers University Press (2003).

[80] Matthias B. T., Wood E. A., Corenzwitt E. and Bala V. B., J. Phys. Chem. Solids, **1**, 188 (1956).

[81] P. Mendels, H. Alloul, G. Collin, N. Blanchard, J. F. Marucco, J. Bobroff, Physica C 235-240, 1595 (1994).

[82] P. Mendels, J. Bobroff, G. Collin, H. Alloul, M. Gabay, J. F. Marucco, N. Blanchard, and B. Grenier, Europhys. Lett. 46, 678 (1999).

[83] K. Mikhalev, S. Verkhovskii, A. Gerashenko, A. Mirmelstein, V. Bobrovskii, K. Kumagai, Y. Furukawa, T. D'yachkova, and Yu. Zainulin Phys. Rev. B **69**, 132415 (2004).

[84] F. Mila and T. M. Rice, Physica C **157**, 561 (1989).

[85] L. L. Miller, X. L. Wang, S. X. Wang, C. Stassis, D. C. Johnston, J. Faber, Jr., and C. K. Loong, Phys. Rev. B **41**, 1921 (1990).

[86] A. J. Millis, H. Monien, and D. Pines, Phys. Rev. B **42**, 167 (1990).

[87] H. Monien, D. Pines, and C. P. Slichter, Phys. Rev. B **41**, 11120 (1990).

[88] P. Monthoux and D. Pines, Phys. Rev. B **49**, 4261-4278 (1994).

[89] R. S. Mulliken, J. Chem. Phys. **23**, 1833 (1955).

[90] V. A. Nandor, J. A. Martindale, R. W. Groves, O. M. Vyaselev, C. H. Pennington, L. Hults, and J. L. Smith, Phys. Rev. B **60**, 6907 (1999).

[91] D. L. Novikov, A. J. Freeman, and J. D. Jorgensen, Phys. Rev. B **51**, 6675 (1995).

[92] H. K. Onnes, Leiden Comm. 120b, 122b, 124c (1911).

[93] S. H. Pan, E. W. Hudson, K. M. Lang, H. Eisaki, S. Uschida, and J. C. Davis, nature, **403**, 746 (2000).

[94] S. H. Pan, E. W. Hudson, K. M. Lang, H. Eisaki, S. Uchida, and J. C. Davis, Nature, **403**, 746 (2003).

[95] K. Park, B. J. Mean, K. H. Lee, G. S. Go, S.W. Seo, K. S. Han, M. Lee, H. S. Lee, H. B. Kim, and W. C. Lee, Phys. Rev. B 59, 11 217 (1999).

[96] C. H. Pennington, D. J. Durand, C. P. Slichter, J. P. Rice, E. D. Bukowski, and D. M. Ginsberg, Phys. Rev. B **39**, 2902 (1989).

[97] W. E. Pickett, Rev. Mod. Phys. **61**, 433 (1989).

[98] D. Pines, Understanding high temperature superconductors: progress and prospects. Physica C 282-287, 273-278 (1997).

[99] D. Poilblanc, D. J. Scalapino and W. Hanke, Phys. Rev. Lett., **72**, 884 (1994).

[100] D. Poilblanc, D.J. Scalapino, and W. Hanke, Phys. Rev. B, **50**, 13020 (1994).

[101] A. Polkovnikov, S. Sachdev, and M. Vojta, Phys. Rev. Lett.,**86**, 296 (2001).

[102] *Copper Oxide Superconductors*, Ch. Poole, T. Datta, and H. A. Farach (Wiley-Interscience, New York, 1988).

[103] R. Prozorov, R. W. Giannetta, P. Fournier, and R. L. Greene Phys. Rev. Lett. **85**, 3700 (2000).

[104] S. Renold, private communication.

[105] P. G. Radaelli, D. G. Hinks, A. W. Mitchell, B. A. Hunter, J. L. Wagner, B. Dabrowski, K. G. Vandervoort, H. K. Viswanathan, and J. D. Jorgenson, Phys. Rev. B **49**, 4163 (1994).

[106] S. Renold, S. Pliberšek, E. P. Stoll, T. A. Claxton, and P. F. Meier, Eur. Phys. J. B **23**, 3 (2001).

[107] S. Renold, T. Heine, J. Weber, and P. F. Meier, Phys. Rev. B **67**, 024501 (2003).

[108] "First principles studies of local electronic structure and magnetic properties in cuprates" S. Renold, PhD thesis (2004).

[109] S. Renold, C. Bersier, P. F. Meier, in preparation.

[110] T. Sato, T. Kamiyama, T. Takahashi, K. Kurahashi, and K. Yamada, Science **291**, 1517 (2001).

[111] A. Shengelaya, private communication.

[112] Y. Sidis, P. Bourges, B. Hennion, L. P. Regnault, R. Villeneuve, G. Collin, and J. F. Marucco, Phys. Rev. B, **53**, 6811 (1996).

[113] M. Sigrist and K. Ueda, Rev. Mod. Phys. **63**, 239 (1991).

[114] "Lectures on unconventional superconductivity" M. Sigrist ETHZ (2004)

[115] J. A. Skinta, T. R. Lemberger, T. Greibe and M. Naito, Phys. Rev. Lett., **88**, 207003 (2002).

[116] C. P. Slichter, in *Strongly Correlated Electronic Materials, A Los Alamos Symposium*, edited by K. S. Bedell, *et al.* (Addison-Wesley, New York, 1994), p. 427.

[117] M. G. Smith, A. Manthiram, J. Zhou, J. B. Goodennouhg, and J. T. Markert, nature **351**, 549 (1991).

[118] R. M. Sternheimer, Z. Naturforsch. **41a** 35.

[119] E. P. Stoll, P. F. Meier, and T. A. Claxton, Phys. Rev. B **65**, 064532 (2002).

[120] E. P. Stoll, P. F. Meier, and T. A. Claxton, Int. J. of Mod. Phys. B, **17**, 3329 (2003).

[121] E. P. Stoll, P. F. Meier, and T.A. Claxton, J. Phys.: Condens. Matter, **15**, 7881 (2003).

[122] J. Sugiyama, S. Tokuono, S.-I. Koriyama, H. Yamauchi, S. Tanaka, Phys. Rev. B **43**, 10489 (1991).

[123] H. U. Suter, E. P. Stoll, P. Hüsser, S. Schafroth, and P. F. Meier, Physica C **282-287**, 1639 (1997).

[124] A. Szabo and N. S. Ostlund, *Modern Quantum Chemistry* (McGraw-Hill, New York, 1982).

[125] J. L. Tallon, J. R. Cooper, P. S. de Silva, G. V. M. Williams, and J. W. Loram, Phys. Rev. Lett., **75**, 4114 (1995).

[126] J. L. Tallon *et al.* Cond-Mat/0008295.

[127] J. M. Tarascon, L. H. Greene, P. Barboux, W. R. McKinnon, G. W. Hull, T. P. Orlando, K. A. Delin, S. Foner and E. J. McNiff, Phys. Rev. B **36**, 8393 (1987).

[128] J. M. Tarascon, P. Barboux, P. F. Miceli, L. H. Greene, G. W. Hull, M. Eibschutz, and S. A. Sunshine, Phys. Rev. B 37, 7458 (1988).

[129] K. R. Thurber, A. W. Hunt, T. Imai, F. C. Chou, and Y. S. Lee, Phys. Rev. Lett. **79**, 171 (1997) and K. R. Thurber, Ph.D. Thesis, MIT (1999).

[130] Y. Tokura, H. Takagi, and S. Uchida, nature **337**, 345 (1989).

[131] C. C. Tsuei and J. R. Kirtley Phys. Rev. Lett. **85**, 182 (2000).

[132] A. Tsukada, Y. Krockenberger, M. Noda, H. Yamamoto, D. Manske, L. Alff, and M. Naito, Solid State Comm. **133**, 427 (2005).

[133] A. C. Uldry, P. F. Meier, submitted, cond-mat/0502075.

[134] T. Uzumaki, N. Kamehara, and K. Niwa, Jpn. J. Appl. Phys. **30**, L981 (1991).

[135] D. Vaknin, S. K. Sinha, C. Stassis, L. L. Miller, and D. C. Johnston, Phys. Rev. B41, 1926 (1990).

[136] S. Verkhovskii, K. Mikhalev, A. Gerashenko, Y. Piskunov, V. Kazantsev, V. Bobrovskii, E. Mitberg, A. Podlesnyak and A. Mirmelstein J. of Superconductivity: Incorp. Novel Magnetism **16**, 543-554 (2003).

[137] G. V. M. Williams, J. L. Tallon, and R. Meinhold, Phys. Rev. B, **51**, 16 503 (1995).

[138] G. V. M. Williams, J. Tallon, R. Dupree, and R. Michalak, Phys. Rev. B **54**, 9532 (1996).

[139] G. V. M. Williams, R. Dupree, and J. L. Tallon, Phys. Rev. B **60**, 1360 (1999) .

[140] G. V. M. Williams, J. L. Tallon, and R. Dupree, Phys. Rev. B 61, 4319 (2000).

[141] G. V. M. Williams and S. Krämer, Phys. Rev. B **64**, 104506 (2001);

[142] G. V. M. Williams, R. Dupree, A. Howes, S. Krämer, H. J. Trodahl, C. U. Jung, M.-S. Park, and S.-I. Lee, Phys. Rev. B **65**, 224520 (2002).

[143] M. K. Wu, J. R. Ashburn, C. J. Torng, P. H. Hor, R. L. Meng, L. Gao, Z. J. Huang, Y. Q. Wang, and C. W. Chu, Phys. Rev. Lett. **58**, 908 (1987).

[144] G. Xiao, F. H. Streitz, A. Gavrin, Y. W. Du, and C. L. Chien, Phys. Rev. B **35**, 8782 (1990).

[145] G. Xiao, M. Z. Cieplak, J. Q. Xiao, and C. L. Chien, Phys. Rev. B **42**, 8752 (1990).

[146] J. S. Xue, J. E. Greedan, and M. Maric, J. Solid State Chem. **102**, 501 (1993).

[147] H. Yamagata, K. Inada, and M. Matsumura, Physica C, **185-189**, 1101 (1991).

[148] H. Yamagata, H. Miyamoto, K. Nakamura, M. Matsumura, and Y. Itoh, J. Phys. Soc. Jpn. **72**, 1768 (2003).

[149] N. C. Yeh, cond-mat/0210656.

[150] Y. Yoshinari, H. Yasuoka, T. Shimizu, H. Takagi, Y. Tokura and S.-I. Uchida, J. Phys. Soc. Jpn. **59**, 1910 (1989).

[151] G.-q. Zheng, Y. Kitaoka, Y. Oda, and K. Asayama, J. Phys. Soc. Jpn. **58**, 36 (1990).

[152] G.-q. Zheng, T. Odaguchi, T. Mito, Y. Kitaoka, K. Asayama, and Y. Kodama, J. Phys. Soc. Jpn. **62**, 2591 (1993).

[153] G.-q. Zheng, Y. Kitaoka, K. Ishida, and K. Asayama, J. Phys. Soc. Jpn. **64**, 2524 (1995).

[154] G.-q. Zheng, T. Sato, Y. Kitaoka, M. Fujita, and K. Yamada, Phys. Rev. Lett., **90**, 197005 (2003).

[155] G.-q. Zheng, P. L. Kuhns, A. P. Reyes, B. Liang, and C. T. Lin, Phys. Rev. Lett. **94**, 047006 (2005).

Acknowledgments

First I would like to thank my mother. She always gave me all the support that I needed to go were I wanted to go. She also suffered from my love for physics. This dissertation is dedicated to her.
I want to express my gratitude to several people, who gave me great support during my doctoral studies.

Daniel Wyler For giving the opportunity of making my PhD thesis with Prof. P. F. Meier and his constant support. Thank you for everything Daniel!

Samuel Renold Almost everything I know about Gaussian 03 and cluster calculations I own him. He also explained me a lot of concepts about superconductivity. I admire his methodology, his rigor and his patience. This thesis wouldn't have been possible without him. He is a very good friend.

Erich Stoll For his constant help and support first of all for the conferences and the publications. For me he is a sort of Yoda master of theoretical solid state physics.

Peter F. Meier For giving me the opportunity of making my phd in his group and for his constant support. His assistance in the preparation of talks and his reading of my work were of great help.

T. A. Claxton For many useful discussions, his patience explaining me the secrets of quantum "che-mystery" and his help.

My girlfriend Sarah For her constant support, especially during the writing phase of my PhD and her help for the Bibliography.

Roman Zwicky For very interesting discussions in particular on the quantum field theoretical approach to condensed matter physics.

Pascal Hoehn For very interesting discussions on philosophy and science. We had long hours together trying to find a philosophical approach for superconductivity.

Finally I would like to thank M. Sigrist, T. M. Rice, H. Keller, K. A. Müller, A. Shengelaya, M. Mali, S. Roos, T. Schneider, T. Mayer, H. R. Ott, I. Kaplan, T. Giamarchi, P. Hirschfeld, J. Mannhart for giving me some of their precious time to answer my questions.

Curriculum vitae

Personalien:

Name: Bersier
Vorname: Christophe
Geboren am: 22. März 1974 in Lausanne VD
Heimatort: Cugy FR

Bildungsgang:

1985-1990: Collège de l'Elysée
1990-1993: Gymnase du Bugnon, Matura Typus C
1993-1996: Eidgenössische Technische Hochschule Lausanne
1996-1999: Eidgenössische Technische Hochschule Zürich, Diplomfach: Theoretische Physik.
Diplom beim Prof. Dr. D. Wyler.
"Calculation of long distance effects in $B^- \to \rho^- + \gamma$ and $B^+ \to D_s^{*+} + \gamma$"
1999-2001: Assistent am Institut für Feldtheorie an der ETHZ.
2001-2005: Doktorand an der Universität Zürich.

Dissertation:

Titel der Dissertation: First-Principles Calculations of the Local Electronic Stucture in Undoped and Doped Cuprates.
Ausgeführt unter der Leitung von: Prof. Dr. P. F. Meier
Antragstellendes Fakultätsmitglied: Prof. Dr. D. Wyler

Dozentenverzeichnis:

K. Hepp
T.M. Rice
N. Straumann
F. Pauss
D. Wyler
C. Mudry
Z. Kunzt
G.M. Graf
P.F. Meier
H. Wachter
P. De Forcrand
F. Bufler
G. Blatter
M. Sigrist
H. R. Ott
T. Hurt
H. Denner
J. Bilgram